

Study on Electrochemical Preparation of Oxide  
Semiconductor Films

(酸化物半導体膜の電気化学形成に関する研究)

January, 2017

Doctor of Engineering

Kentaro Nishiyama

西山 健太郎

Toyohashi University of Technology



Date of Submission:

平成 29 年 1 月 12 日

Department 機械工学専攻	Student ID Number 学籍番号	第 103242 号	Supervisors 指導教員	伊崎 昌伸 横山 誠二
Applicant's name 氏名	西山 健太朗			

**Abstract****論文内容の要旨 (博士)**

Title of Thesis 博士学位論文名	Study on Electrochemical Preparation of Oxide Semiconductor Films (酸化物半導体膜の電気化学形成に関する研究)
----------------------------	---

(Approx. 800 words)

(要旨 1,200 字程度)

Metal oxide films have been utilized in electronics and chemical industries due to their electrical, optical, piezoelectrical, and magnetic characteristics. The oxides have been also used as host materials for transparent conductive layers, electronic parts such as thin film transistors and capacitors and photocatalysts. Especially, oxide semiconductor layers with wide bandgap energy over 2 eV have attracted increasing attention as materials to open new door for ultraviolet light-emitting diode (LED), spintronics, and multi ferroic materials with controlled physical characteristics.

Oxide semiconductor films have been prepared using gas-phase deposition processes and solution chemical processes. Gas-phase deposition processes have several advantages like the ability to control thickness and form high purity semiconductors, with disadvantages of expensive apparatus, the need of facility for gasses and high vacuum, resulting in large amount of energy consumption and CO<sub>2</sub> emission. Solution chemical processes have several advantages over the gas-phase deposition processes in the equipment, facilities, and fabrication costs, and electrochemical processes have been employed to prepare precursors of Cu(In,Ga)Se<sub>2</sub> (CIGS) and Cu<sub>2</sub>ZnSnS<sub>4</sub> (CZTS) compounds for photovoltaic applications on the industry scale.

The wide bandgap oxide semiconductor films were applied to optical devices, and it is well known that their compositions, structures and chemical states influence their optical properties. However, electrochemical preparation for oxide semiconductor films applied to optical devices has some problems. It is well known that mixing other materials to an oxide semiconductor changes its optical properties and electrical properties, but almost no example of a mixed-oxide film is reported. Moreover, valence values of metal elements in oxide were uncontrollable because of the existence of mixed valence elements and impurities, and this led to the uncontrollability of optical properties and electrical properties of oxide semiconductor. These problems can be solved by designing the processes with thermodynamic calculation. In this thesis, I show resolving these problems using electrochemical deposition of oxide films

based on thermodynamic calculation with some examples, and I demonstrate a novel device fabricated by electrochemical deposition overcoming weaknesses of existing device, in order to show the possibility for industrial applications.

First, Zn-Ce-O films, mixed oxide films, were prepared on an electrodeposited Ag layer in an aqueous solution containing a zinc nitrate hydrate and cerium nitrate hydrate based on thermodynamic calculation. Theory of deposition for mixed-oxide films was discussed from a critical pH perspective relative to ion species and oxides. The concentrations of metal ions in the Zn-Ce-O films were depending on ions concentration of Zn and Ce in the solution. The Ce content in the films changed from 0 to 43 mol% depending on the Ce concentration in solutions. Zn-Ce-O films were identified as a wurtzite ZnO containing Ce (Ce:ZnO) at 5 mol% Ce and mixtures of Ce:ZnO and CeO<sub>2</sub> containing Zn(Zn:CeO<sub>2</sub>) at 20-43 mol% Ce. The bandgap energies of Zn-Ce-O films have changed from 3.4 eV to 2.9 eV depending on the Ce content.

Secondly, I demonstrated deposition of tungsten oxide hydrate films of WO<sub>3</sub>·H<sub>2</sub>O and WO<sub>3</sub>·(H<sub>2</sub>O)<sub>0.33</sub> with a controlled valence value of the metal element in the oxides using electrochemical deposition based on thermodynamic calculation. The valence state of obtained tungsten oxide hydrate films was only +6, and this film was proved to have high chemical uniformity. Tungsten oxide hydrate films of WO<sub>3</sub>·H<sub>2</sub>O and WO<sub>3</sub>·(H<sub>2</sub>O)<sub>0.33</sub> were prepared on conductive glass substrates by anodic deposition in aqueous solutions containing 0.01–0.5 mol/L WO<sub>4</sub><sup>2-</sup>. The large square-shaped WO<sub>3</sub>·H<sub>2</sub>O obtained in the 0.01–0.09 mol/L WO<sub>4</sub><sup>2-</sup> solutions possessed a bandgap energy of approximately 2.5 eV, and granular-WO<sub>3</sub>·(H<sub>2</sub>O)<sub>0.33</sub> films obtained in the 0.05–0.5 mol/L WO<sub>4</sub><sup>2-</sup> solutions showed 3.3 eV in bandgap energy.

Thirdly, on the basis of thermodynamic calculations, I tried to form SnO<sub>2</sub> films having uniformity in valence. Sn(O,OH), mixture of SnO<sub>2</sub> and Sn(OH)<sub>4</sub>, having unified valence of +4 was prepared by electrodeposition designed using thermodynamic calculations. Obtained Sn(O,OH) completely covered the substrates, and had smooth surfaces and structures with tetragonal fine crystals.

Finally, I fabricated the WO<sub>3</sub>·(H<sub>2</sub>O)<sub>0.33</sub>/Sn(O,OH) bilayer structure for all-solid-state electrochromic device by anodic electrodeposition on the FTO substrate. The WO<sub>3</sub>·(H<sub>2</sub>O)<sub>0.33</sub>/Sn(O,OH) bilayer device showed electrochromism; this was an evident demonstration of a novel and low-costly all-solid-state electrochromic device.

I resolved the problems of existing electrodeposition for wide band gap oxide semiconductor by electrochemical deposition based on thermodynamic calculation. The results demonstrated here will strongly contribute to the improvement of the deposition process of oxide semiconductors and their devices.

# CONTENTS

## CHAPTER 1: Introduction

1.1 Introduction to oxide semiconductor films and preparation	1
1.2 Design of electrochemical deposition process and potential-pH diagram	4
1.3 Outline of this study	10

## REFERENCE

## **Chapter 2: Electrochemical deposition of Zn-Ce-O films with controlled bandgap energy**

### 2.1 Introduction

2.1.1 Electrochemical deposition using reduction reaction of nitrate 18

2.1.2 Materials and objective of this study 19

### 2.2 Experimental

2.2.1 Thermodynamic calculation of electrochemical deposition for Zn-Ce-O films 20

2.2.2 Experimental procedure 29

2.2.3 Characterization of Zn-Ce-O films 30

### 2.3 Results and discussion

2.3.1 Composition of Zn-Ce-O films 31

2.3.2 Structural characterization of Zn-Ce-O films 33

2.3.3 Optical property of Zn-Ce-O films 42

2.4 Conclusions 45

## REFERENCE

## **Chapter 3: Electrochemical deposition of tungsten oxide hydrate films with controlled bandgap energy**

3.1 Introduction	
3.1.1 Materials and issues of existing electrochemical depositions	50
3.1.2 Anodic electrochemical deposition using oxygen-evolution reaction	52
3.1.3 Objective of this study	52
3.3 Experimental	
3.2.1 Theory of electrochemical deposition for tungsten oxide hydrates films	53
3.2.2 Experimental procedure for electrochemical deposition of tungsten oxide hydrates films	60
3.2.3 Characterization of tungsten oxide hydrates films	61
3.3 Results and Discussion	
3.3.1 Composition and structure of tungsten oxide hydrates films	62
3.3.2 Optical properties of $\text{WO}_3 \cdot \text{H}_2\text{O}$ and $\text{WO}_3 \cdot (\text{H}_2\text{O})_{0.33}$ films	73
3.3.3 Photoelectrochemical properties of $\text{WO}_3 \cdot \text{H}_2\text{O}$ and $\text{WO}_3 \cdot (\text{H}_2\text{O})_{0.33}$ films	75
3.4 Conclusions	79
REFERENCE	

## Chapter 4: Electrochemical deposition of tin oxide hydrate film

### 4.1 Introduction

4.1.1 Materials and issues of existing electrochemical depositions for SnO<sub>2</sub> 85

4.1.2 Anodic electrochemical deposition using oxidization reaction of dissolved ions 86

4.1.3 Objective of this study 87

### 4.2 Experimental

4.2.1 Theory of electrochemical deposition for tin oxide hydrate compounds 87

4.2.2 Experimental procedure for electrochemical deposition of tin oxide hydrate compounds 89

4.2.3 Characterization of tin oxide hydrate compounds 90

### 4.3 Result and discussion

4.3.1 Composition of tin oxide hydrate compounds 91

4.3.2 Structural characterization of tin oxide hydrate compounds 96

4.4 Conclusions 99

## REFERENCE

**Chapter 5: Solid State tungsten oxide hydrate/tin oxide hydrate electrochromic device prepared by electrochemical depositions**

5.1 Introduction	
5.1.1 Subjective this Chapter	103
5.1.2 Electrochromic device	104
5.2 Experimental	
5.2.1 Fabrication of a FTO/ $\text{WO}_3(\text{H}_2\text{O})_{0.33}/\text{Sn}(\text{O},\text{OH})$ bilayer structure	105
5.2.2 Observations of a FTO/ $\text{WO}_3(\text{H}_2\text{O})_{0.33}/\text{Sn}(\text{O},\text{OH})$ bilayer structure	106
5.3 Results and discussion	
5.3.1 Characterizations of a FTO/ $\text{WO}_3(\text{H}_2\text{O})_{0.33}/\text{Sn}(\text{O},\text{OH})$ bilayer structure	106
5.3.2 Coloration reaction of a FTO/ $\text{WO}_3(\text{H}_2\text{O})_{0.33}/\text{Sn}(\text{O},\text{OH})$ bilayer structure	109
5.4 Conclusions	112

## **Chapter 6: Summary and future direction**

6.1 Research summary	115
6.2 Acknowledgement	119
6.3 Research achievements	
6.3.1 List of publications	121
6.3.2 List of conferences	112
6.3.3 Awards received	122

# **CHAPTER 1**

## **Introduction**

### **1.1 Introduction to oxide semiconductor films and preparation**

Metal oxide films have been utilized in electric, and chemical industries due to the electrical, optical, piezoelectrical, magnetic, and chemical characteristics. The oxides of ZnO, In<sub>2</sub>O<sub>3</sub> and SnO<sub>2</sub> have been used as the host material for transparent conductive layers because of the high optical transparency and ease to control the conductivity[1-3]. SiO<sub>2</sub>, Al<sub>2</sub>O<sub>3</sub>, and MgO have been used as electronic components such as thin film transistor and capacitor due to the high resistivity[4,5]. The ZnO, TiO<sub>2</sub>, WO<sub>3</sub>, and

CeO<sub>2</sub> have been used as photocatalyst due to the wide bandgap energy[6-9]. Especially, oxide semiconductor films with the wide bandgap energy over 2 eV have attracted increasing attention as the material to open new door for ultraviolet light-emitting diode (LED), spintronics, and multi ferroic material with controlled physical characteristics.

Oxide semiconductor films have been prepared using several techniques such as gas-phase deposition processes and solution chemical processes. Gas-phase deposition processes such as a sputtering, evaporation, molecular beam epitaxy, laser abrasion, and chemical vapor deposition have been used for the preparation in the electric and electronic industries. These processes have several advantages of the ability to control the thickness and form high purity semiconductors with disadvantages of expensive apparatus, the need of the facility for gasses and high vacuum, resulting in large amount of energy consumption and CO<sub>2</sub> emission. Solution chemical process such as electrochemical and chemical processes, hydrothermal process, and sol-gel process, has several advantage over the gas-phase deposition process in the equipment and facility, fabrication cost, and the electrochemical process has been employed to prepare precursors of Cu(In,Ga)Se<sub>2</sub> (CIGS) and Cu<sub>2</sub>ZnSnS<sub>4</sub> (CZTS) compounds for photovoltaic applications on the industry scale[10,11]. The preparation of oxide semiconductor films by electrochemical reactions have been tried, but the films were identified as the metal oxide hydrate or metal hydrate till 1996. The preparation of ZnO semiconductor films were reported from two research groups, and then the oxide semiconductor and ferromagnetic films have been prepared by electrochemical depositions. The elements prepared as oxide were summarized on the periodic table shown in Figure 1.1[12-26].

	1																	18	
1	H	2												13	14	15	16	17	He
2	Li	Be												B	C	N	O	F	Ne
3	Na	Mg	3	4	5	6	7	8	9	10	11	12	Al	Si	P	S	Cl	Ar	
4	K	Ca	Sc	Ti	V	Cr	Mn	Fe	Co	Ni	Cu	Zn	Ga	Ge	As	Se	Br	Kr	
5	Rb	Sr	Y	Zr	Nb	Mo	Tc	Ru	Rh	Pd	Ag	Cd	In	Sn	Sb	Te	I	Xe	
6	Cs	Ba	La	Hf	Ta	W	Re	Os	Ir	Pt	Au	Hg	Tl	Pb	Bi	Po	At	Rn	
7	Fr	Ra	Ac																
				Ce	Pr	Nd	Pm	Sm	Eu	Gd	Tb	Dy	Ho	Er	Tm	Yb	Lu		
				Th	Pa	U	Np	Pu	Am	Cm	Bk	Cf	Es	Fm	Md	No			

 oxides prepared by electrochemical deposition  
 oxides prepared by electrochemical deposition in our laboratory

Figure 1.1 Oxides could be prepared by electrochemical deposition on periodic table.

Izaki group developed two ways to prepare directly semiconductor and ferromagnetic oxide films by electrochemical depositions. One is the cathodic deposition which was driven by using the reduction reaction of nitrate ion containing in the solution, and the ability was approved by the direct formation of ZnO, In<sub>2</sub>O<sub>3</sub>, CeO<sub>2</sub>, Fe<sub>3</sub>O<sub>4</sub>[12-15]. Another one is the anodic deposition using an O<sub>2</sub> evolution reaction, and Ag<sub>2</sub>O and CuO were directly prepared by the anodic deposition[16,17]. Almost all the oxide film prepared by electrochemical deposition was identified as single metal oxide such as ZnO, and CeO<sub>2</sub>. The CeO<sub>2</sub> possessed two states of Ce, Ce<sup>3+</sup> and Ce<sup>4+</sup>, but the Ce<sup>3+</sup> state strongly affected the semiconductor characteristic of CeO<sub>2</sub>[14].

## 1.2 Design of electrochemical deposition process and potential-pH diagram

The wide bandgap oxide semiconductor films have been applied to optical devices, and the composition, structure, and chemical state influence the optical property. Electrochemical deposition process for preparing oxide semiconductor films appropriate to optical devices has several problems of the incorporation of impurity oxide phase with harmful effects on optical and electrical properties of the oxide semiconductor, and difficulty to control the valence state of oxide semiconductor with mixed valence states. It is expected to propose the way by thermodynamic design and calculation. The electrochemical deposition for oxide semiconductors was composed of acid-base and reduction-oxidation reactions in aqueous solutions. The thermodynamic calculations on the acid-base and reduction-oxidation reactions are described as follows.

Acid-base reaction:



$$\Delta_r G^0 = (\Delta_f G_{M(OH)_n}^0) - ((\Delta_f G_{M^{n+}}^0) + n(\Delta_f G_{H_2O}^0)) \quad (1.2)$$

$$\Delta_r G^0 = -RT \ln K \quad (1.3)$$

$$\ln K \approx 2.303 \log K \quad (1.4)$$

$$K = \frac{a_{M(OH)_n} a_{H^+}^n}{a_{M^{n+}} a_{H_2O}^n} = \frac{[M(OH)_n][H^+]^n}{[M^{n+}][H_2O]^n} \quad (1.5)$$

$$\log[H^+] = -\text{pH} \quad (1.6)$$

, where  $\Delta_r G^0$ ,  $\Delta_f G_{M(OH)_n}^0$ ,  $\Delta_f G_{M^{n+}}^0$ ,  $\Delta_f G_{H_2O}^0$ ,  $R$ ,  $T$  and  $K$  are Gibbs free energy change per mole for the reaction (1.2), standard Gibbs free energy of the formation of  $M(OH)_n$ ,  $M^{n+}$ , and  $H_2O$ , gas constant, thermodynamic temperature, and equilibrium constant,

respectively. And,  $a_{M(OH)_n}$ ,  $a_{M^{n+}}$ ,  $a_{H_2O}$  and  $a_{H^+}$  are activity of  $M(OH)_n$ ,  $M^{n+}$ ,  $H_2O$ , and  $H^+$ , respectively. Activities are nearly equal to ion concentrations in diluted solutions, and ion concentration of  $[M(OH)_n]$ ,  $[M^{n+}]$ ,  $[H_2O]$  and  $[H^+]$  are used alternative to the activity in the study. Thermodynamic calculation of the acid-base reaction for electrochemical deposition of oxide semiconductor is reflected to the critical pH value and solubility curve. The solubility curve shows the maximum concentration of the dissolved species at the pH value. In the solubility curve, the logarithmic concentration of dissolved species is represented by vertical axis, and pH value is represented by horizontal axis. Solubility curves were made from the thermodynamic calculation about possible combination of solid phase species and all dissolved species in aqueous solution using standard Gibbs free energy of formation and solubility product.

Reduction-oxidation reaction:



$$\Delta_r G^0 = (\Delta_f G_{M^0}^0) - (\Delta_f G_{M^{n+}}^0) \quad (1.8)$$

$$E = E^0 + \frac{RT}{zF} \ln \frac{[M^{n+}]}{[M^0]} \quad (1.9)$$

$$E^0 = \frac{-\Delta_r G^0}{zF} \quad (1.10)$$

, where  $\Delta_f G_{M^0}^0$ ,  $E$ ,  $E^0$ ,  $z$ , and  $F$  are standard free energy of formation of  $M^0$ , cell potential, standard electrode potential, number of moles of electrons, and Faraday constant (= 96485 C/mol), respectively.

The reaction composed of both acid-base reaction and reduction-oxidation reactions is described as follows.



$$\Delta_r G^0 = y(\Delta_f G_Y^0) - x(\Delta_f G_X^0) \quad (1.12)$$

$$\Delta_r G = \Delta_r G^0 + RT \ln Q + zFE \quad (1.13)$$

, where  $\Delta_f G_X^0$ ,  $\Delta_f G_Y^0$  and  $Q$  are the standard free energy of formation of X, Y and reaction quotient, respectively. In equilibrium state,  $\Delta_r G = 0$ ,  $Q = K$ , the equation (1.13) change into equation (1.14);

$$0 = \Delta_r G^0 + RT \ln K + zFE \quad (1.14)$$

$$K = \frac{a_Y^y}{a_X^x a_{H^+}^h} = \frac{[Y]^y}{[X]^x [H^+]^h} \quad (1.15)$$

$$\ln K = 2.303 \left( \log \frac{[Y]^y}{[X]^x} + h(\text{pH}) \right) \quad (1.16)$$

$$0 = \Delta_r G^0 + 2.303RT \left( \log \frac{[Y]^y}{[X]^x} + h(\text{pH}) \right) + zFE \quad (1.17)$$

Here,  $a_X$ ,  $a_Y$ ,  $[X]$  and  $[Y]$  are activity of X, Y, ion concentration of X, and Y, respectively. As shown in the equation (1.17), the Gibbs free energy,  $\Delta_r G^0$  is functions of the ion concentration, the pH value, and the cell potential at equilibrium state. Thermodynamic calculations of the acid-base reaction and the oxidation-reduction reaction for the electrochemical deposition of oxide semiconductors are reflected to the potential-pH diagram. In the potential-pH diagram, the potential is represented by vertical axis, and pH value is represented by horizontal axis.

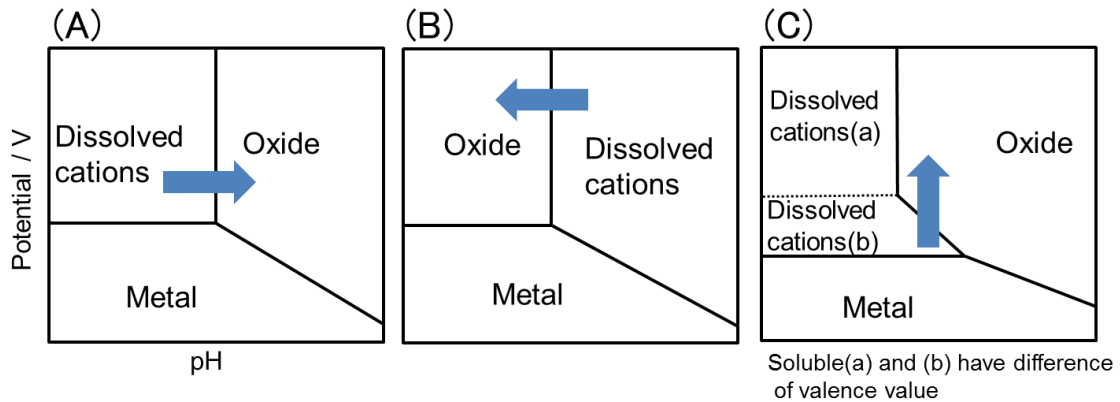


Figure 1.2 Schematic of three type potential-pH diagram.

The potential-pH diagram shows the stable region of substances in the metal-water system and is specified to three types in the oxide formation. The oxide region is located at high pH side of the dissolved cation region, and the oxide can be obtained by raising pH value from the cation region to oxide region as shown in Fig.1.2(A), which is specified as A-type. The oxide region is located at low pH side of the dissolved cation region, and the oxide can be obtained by decreasing pH value from the cation region to the oxide region as shown in Fig.1.2(B), which is specified as B-type. There is no change in the valence state of the metallic element through the reaction in A-type and B-type preparations, and solubility curves are very important, because the acid-base reaction directly relates to the formation of oxides. The valence state of the metallic element is kept at the constant value through the reaction. There is two or more valence state for the dissolved cation, and the oxide region is located at high pH side of both the cation region in Fig. 1.2 (C). The oxide can be obtained by changing the potential to the positive side from the cation region (b) with the change in the valence state of the metallic element as represented by arrow, which is specified as C-type. In

the “A-type” potential-pH diagram, oxides are obtained by electrochemical deposition using the raise in the pH value induced by the reduction reaction of nitrate ions and molecular oxygen. The electrochemical deposition of ZnO using the reduction-reaction of nitrate ions was demonstrated by Izaki et al.[12] in 1996, and CeO<sub>2</sub>[14], MgO[18], Y<sub>2</sub>O<sub>3</sub>[19] and In<sub>2</sub>O<sub>3</sub>[27] were obtained by the reduction reaction of nitrate ions. ZrO<sub>2</sub> and Y<sub>2</sub>O<sub>3</sub> were prepared by electrochemical deposition by using the reduction reaction of H<sub>2</sub>O[17]. The “B-type” potential-pH diagram is appropriate to prepare oxides by decreasing the pH value originated from the oxidization reaction of H<sub>2</sub>O, and the reaction was generated by the anodic electrochemical deposition. CuO and Ag<sub>2</sub>O have been prepared by the anodic electrochemical deposition using the oxidization reaction of H<sub>2</sub>O[16,17]. In the case of “C-type” potential-pH diagram, the oxide can be prepared by the oxidation-reduction reaction between dissolved cations and oxides region. Metal cation dissolved in the solution is oxidized by anodic polarization, and the oxide or hydrate can be obtained by reacting O<sub>2</sub> originated from H<sub>2</sub>O. AgO was prepared by the anodic electrochemical deposition in this reaction[20]. In “A-type,” and “B-type” potential-pH diagrams, oxides were prepared by acid-base reaction, and the “C type” potential-pH diagram provides the preparation of oxides by the oxidization-reduction reaction. Solar cells[29], passivation film of LED reflector[30], and gas sensor[31] have been fabricated by using these electrochemical reactions.

This study deals with the two obstacles laid in the preparation of oxide semiconductors by electrochemical depositions in aqueous solutions, difficulty of the preparation of complex oxides containing two or more metallic elements and the preparation of single valence state oxide in the oxide system with several valence states.

ZnO-CeO<sub>2</sub> system was selected to propose the preparation process of the complex oxide, Zn-Ce-O, due to the importance in the optical application and electrochemical reason. Simple oxides of ZnO and CeO<sub>2</sub> can be obtained by reducing the nitrate ion containing in aqueous solutions, resulting in the raise in the pH value in the vicinity of the substrate surface, which is specified as A-type already mentioned. The critical pH value is important in the preparation of the ZnO-CeO<sub>2</sub> complex oxide in simple aqueous solution, and the preparation is realized by adjusting the solution formulation based on the thermodynamic calculation specified as A-type.

Tungsten oxide was selected to propose the preparation process of the WO<sub>3</sub> with only W<sup>6+</sup> state due to the optical property and existence of several state tungsten oxide such as WO<sub>2</sub>, W<sub>2</sub>O<sub>5</sub>, and WO<sub>3</sub> in the oxide system. The tungsten oxide has been prepared by electrochemical deposition specified in A-type, but the deposited tungsten oxide film contained some oxides with different valence state. This study proposed the way to overcome this obstacle by applying electrochemical reaction specified as B-type.

Tin oxide was selected to propose the preparation process of the SnO<sub>2</sub> with Sn<sup>4+</sup> state due to the optical property and solution chemical reason. Several research works to prepare the SnO<sub>2</sub> film have been carried out by using the electrochemical deposition specified as A-type, but the Sn<sup>0</sup> impurity state was incorporated into the tin oxide film, due to the difficulty in controlling the deposition condition. Since SnO<sub>2</sub> region is located at positive potential side of the Sn<sup>2+</sup> state in the potential-pH diagram, the preparation of the SnO<sub>2</sub> not containing Sn<sup>0</sup> impurity state can be realized by anodic polarization specified as C-type.

### 1.3 Outline of this study

This study aims to indicate the importance of designing electrochemical deposition reaction based on thermodynamics and the calculation using potential-pH diagrams of “A, B and C-type,” and to approve the ability for preparing oxide semiconductors by controlling the deposition process. The way for designing electrochemical deposition reactions for oxide semiconductor preparations based on the thermodynamics and potential-pH diagram has been proposed by demonstrating preparation of complicated oxide, ZnO-CeO<sub>2</sub> and single valence state oxide, WO<sub>3</sub>, and SnO<sub>2</sub>. Furthermore, we demonstrated the fabrication of novel solid-state device using new electrochemical deposition process for constructing oxide components prepared in this study to show the possibility for exploring to industrial use.

In **Chapter 2**, Zn-Ce-O films were prepared on an electrodeposited Ag layer in an aqueous solution containing a zinc nitrate hydrate and cerium nitrate hydrate. The solution formulation was designed by the critical pH value calculated with the thermodynamic calculation for ZnO/Zn<sup>2+</sup> and CeO<sub>2</sub>/Ce<sup>3+</sup> systems. The metal element content in the Zn-Ce-O films depended on the ion concentration of Zn and Ce cations in the solution. The structural and optical characteristics were investigated using a X-ray diffraction analysis, scanning electron microscopy, and reflectance spectra measurement. The Ce content in the films changed from 0 to 43 mol% depending on the Ce concentration in solutions. Zn-Ce-O films were identified as a wurtzite Ce:ZnO for 5% Ce, a mixture of Ce:ZnO and Zn:CeO<sub>2</sub> 20-43% Ce. Zn-Ce-O films showed the bandgap energy change from 3.4 eV to 2.9 eV depending on the Ce content.

In **Chapter 3**, the preparation of tungsten oxide hydrate films of  $\text{WO}_3 \cdot \text{H}_2\text{O}$  and  $\text{WO}_3 \cdot (\text{H}_2\text{O})_{0.33}$  was demonstrated by using electrochemical deposition designed based on thermodynamic calculation. The valence state of tungsten oxide hydrate films were in only +6 state, and the film showed the homogeneity in chemical composition over entirely the films. Tungsten oxide hydrate films of  $\text{WO}_3 \cdot \text{H}_2\text{O}$  and  $\text{WO}_3 \cdot (\text{H}_2\text{O})_{0.33}$  were prepared on conductive glass substrate by the anodic deposition in aqueous solutions 0.01–0.5 mol/L  $\text{WO}_4^{2-}$ . Structural and optical characterizations were carried out by X-ray photoelectron spectroscopy, X-ray diffraction, SEM observation, optical absorption measurements, and photoelectrochemical measurements. The large square-shaped  $\text{WO}_3 \cdot \text{H}_2\text{O}$  obtained in the 0.01–0.09 mol/L  $\text{WO}_4^{2-}$  solutions possessed a bandgap energy of approximately 2.5 eV, and granular- $\text{WO}_3 \cdot (\text{H}_2\text{O})_{0.33}$  films obtained in the 0.05–0.5 mol/L  $\text{WO}_4^{2-}$  solutions showed 3.3 eV in bandgap energy. The  $\text{WO}_3 \cdot \text{H}_2\text{O}$ - $\text{WO}_3 \cdot (\text{H}_2\text{O})_{0.33}$  mixed films prepared in the 0.01–0.09 mol/L  $\text{WO}_4^{2-}$  solutions showed a photoresponse for visible light at 380–600 nm, due to the existence of 2.5 eV-bandgap- $\text{WO}_3 \cdot \text{H}_2\text{O}$ . The  $\text{WO}_3 \cdot \text{H}_2\text{O}$  film is a realistic candidate as a photomaterial such as photocatalyst operative in visible light.

In **Chapter 4**,  $\text{SnO}_2$  with only  $\text{Sn}^{4+}$  state was prepared by electrochemical deposition designed based on thermodynamic calculation. The  $\text{Sn}(\text{O},\text{OH})$  was a mixture of  $\text{SnO}_2$  and  $\text{Sn}(\text{OH})_4$  with only  $\text{Sn}^{4+}$  state, and the smooth film with tetragonal fine grains deposited over entirely the substrate surface.

In **Chapter 5**, the fabrication of  $\text{WO}_3 \cdot (\text{H}_2\text{O})_{0.33}/\text{Sn}(\text{O},\text{OH})$  bilayer structure for all-solid-state electrochromic device was constructed by anodic electrochemical deposition of  $\text{WO}_3 \cdot (\text{H}_2\text{O})_{0.33}$  followed by electrochemical deposition of  $\text{Sn}(\text{O},\text{OH})$  films

on the transparent conductive glass substrate. The  $\text{WO}_3 \cdot (\text{H}_2\text{O})_{0.33} / \text{Sn}(\text{O}, \text{OH})$  bilayer structure was analyzed for chemical states, structure, and coloration character by XPS measurement, FE-SEM observation, and UV-vis spectroscopy measurement. Electrochromic behavior of the  $\text{WO}_3 \cdot (\text{H}_2\text{O})_{0.33} / \text{Sn}(\text{O}, \text{OH})$  bilayer structure was observed by changing the appearance from clear transparency to blue color, and the  $\text{WO}_3 \cdot (\text{H}_2\text{O})_{0.33} / \text{Sn}(\text{O}, \text{OH})$  bilayer structure is a realistic candidate low-cost and solid-state electrochromic device.

In **Chapter 6**, the summary of all results obtained was made.

## REFERENCES

- [1] J. Rousset, E. Saucedo, D. Lincot, Extrinsic Doping of Electrodeposited Zinc Oxide Films by Chlorine for Transparent Conductive Oxide Applications, *Chem. Mater.*, **21**, 534 (2009).
- [2] M.J. Alam, D.C. Cameron, Optical and electrical properties of transparent conductive ITO thin films deposited by sol-gel process, *Thin Solid Films*, **377**, 455 (2000).
- [3] B. Thangaraju, Structural and electrical studies on highly conducting spray deposited fluorine and antimony doped SnO<sub>2</sub> thin films from SnCl<sub>2</sub> precursor, *Thin Solid Films*, **402**, 71 (2002).
- [4] S. Kim, J. Nah, I. Jo, D. Shahrjerdi, L. Colombo, Z. Yao, E. Tutuc, S.K. Banerjee, Realization of a high mobility dual-gated graphene field-effect transistor with Al<sub>2</sub>O<sub>3</sub> dielectric, *Appl. Phys. Lett.*, **94**, 062107 (2009).
- [5] B. Luo, J.W. Johnson, J. Kim, R.M. Mehandru, F. Ren, B.P. Gila, A.H. Onstine, C.R. Abernathy, S.J. Pearton, A.G. Baca, R.D. Briggs, R.J. Shul, C. Monier, J. Han, Influence of MgO and Sc<sub>2</sub>O<sub>3</sub> passivation on AlGaIn/GaN high-electron-mobility transistors, *Appl. Phys. Lett.*, **80**, 1661 (2002).
- [6] H.F. Lin, S.C. Liao, S.W. Hung, The dc thermal plasma synthesis of ZnO nanoparticles for visible-light photocatalyst, *J. Photochem. Photobiol. A Chem.*, **174**, 82 (2005).
- [7] A. Fujishima, K. Honda, Electrochemical Photolysis of Water at a Semiconductor Electrode, *Nature*, **238**, 37 (1972).

- [8] D.W. Hwang, J. Kim, T.J. Park, J.S. Lee, Mg-doped  $\text{WO}_3$  as a novel photocatalyst for visible light-induced water splitting, *Catal. Lett.*, **80**, 53 (2002).
- [9] P. Ji, J. Zhang, F. Chen, M. Anpo, Study of adsorption and degradation of acid orange 7 on the surface of  $\text{CeO}_2$  under visible light irradiation, *Appl. Catal. B*, **85**, 148 (2009).
- [10] A.M. Fernández, R.N. Bhattacharya, Electrodeposition of  $\text{CuIn}_{1-x}\text{Ga}_x\text{Se}_2$  precursor films: optimization of film composition and morphology, *Thin Solid Films*, **474**, 10 (2005).
- [11] J.J. Scragg, P.J. Dale, L.M. Peter, Towards sustainable materials for solar energy conversion: Preparation and photoelectrochemical characterization of  $\text{Cu}_2\text{ZnSnS}_4$ , *Electrochem. Commun.*, **10**, 639 (2008).
- [12] M. Izaki, T. Omi, Transparent zinc oxide films prepared by electrochemical reaction, *Appl. Phys. Lett.*, **68**, 2439 (1996).
- [13] M. Izaki, Preparation of Transparent Indium Oxide Film from a Chemically Deposited Precursor, *Electrochem. Solid State Lett.*, **1**, 215(1998).
- [14] M. Izaki, M. Ishikawa, M. Inoue, Preparation of Rare-Earth Metal Oxide Films through Electrochemical Reaction, *Proc. Electrochem. Soc.*, **2000**, 1 (2000).
- [15] T. Shinagawa, M. Izaki, H. Inui, K. Murase, Y. Awakura, Microstructures and MR effects of transparent ferromagnetic chemically prepared Fe–Zn–O films, *Physica Status Solidi A*, **203**, 2760(2006).

- [16] M. Izaki, M. Nagai, K. Maeda, F.B. Mohamad, K. Motomura, J. Sasano, T. Shinagawa, S. Watase, Electrodeposition of 1.4-eV-Bandgap p-Copper (II) Oxide Film With Excellent Photoactivity, *J. Electrochem. Soc.*, **158**, D578 (2011).
- [17] Y. Ida, S. Watase, T. Sinagawa, M. Watanabe, M. Chigane, M. Inaba, A. Tasaka, M. Izaki, Direct Electrodeposition of 1.46 eV Bandgap Silver(I) Oxide Semiconductor Films by Electrogenerated Acid, *Chem. Mater.*, **20**, 1254 (2008).
- [18] G. Zou, R. Liu, W. Chem, Highly textural lamellar mesostructured magnesium hydroxide via a cathodic electrodeposition process, *Mater. Lett.*, **61**, 1990 (2007).
- [19] A.A.M. Barmi, M. Aghazadeh, H.M. Shiri, F. Ghorab, Cathodic electrodeposition and characterization of nanostructured  $Y_2O_3$  from nitrate solution. Part I: Effect of current density, *Rus. J. Electrochemi.*, **49**, 583 (2013).
- [20] B.E. Breyfogle, C.J. Hung, M.G. Shumsky, J.A. Switzer, Electrodeposition of Silver(II) Oxide Films, *J. Electrochem. Soc.*, **143**, 2741 (1996).
- [21] M. Chigane, T. Shinagawa, Titanium dioxide thin films prepared by electrolysis from aqueous solution of titanium-lactic acid complex for dye-sensitized solar cells, *Thin Solid Films*, **520**, 3510 (2012).
- [22] S. Chou, F. Cheng, J. Chen, Electrodeposition synthesis and electrochemical properties of nanostructured  $\gamma$ - $MnO_2$  films, *J. Power Sources*, **162**, 727 (2006).
- [23] I.G. Casella, M.R. Guascito, Anodic electrodeposition of conducting cobalt oxyhydroxide films on a gold surface. XPS study and electrochemical behaviour in neutral and alkaline solution, *J. Electroanal. Chem. Interfacial Electrochem.*, **476**, 54 (1999).

- [24] M.S. Wu, Y.A. Huang, C.H. Yang, J.J. Jow, Electrodeposition of nanoporous nickel oxide film for electrochemical capacitors, *Int. J. Hydrogen Energy*, **32**, 4153(2007).
- [25] R.S. Patil, M.D. Uplane, P.S. Patil, Structural and optical properties of electrodeposited molybdenum oxide thin films, *Appl. Surf. Sci.*, **252**, 8050 (2006).
- [26] J.K. Lee, G.P. Kim, I.K. Song, S.H. Baeck, Electrodeposition of mesoporous  $V_2O_5$  with enhanced lithium-ion intercalation property, *Electrochem. Commun.*, **11**, 1571 (2009).
- [27] R. Henriquez, E. Munoz, E.A. Dalchiele, R.E. Marotti, F. Martin, D. Leinen, J.R. Ramos-Barrado, H. Gomez, Electrodeposition of  $In_2O_3$  thin films from a dimethylsulfoxide based electrolytic solution, *Physica Status Solidi A Appl. Res.*, **210**, 297 (2013).
- [28] M. Aghazadeha, A.A.M. Barmi, H. M. Shiri, S. Sedaghat, Cathodic electrodeposition of  $Y(OH)_3$  and  $Y_2O_3$  nanostructures from chloride bath. Part II: Effect of the bath temperature on the crystal structure, composition and morphology, *Ceram. Int.*, **39**, 1045 (2013).
- [29] M. Izaki, T. Shinagawa, K. Mizuno, Y. Ida, M. Inaba, A. Tasaka, Electrochemically constructed p- $Cu_2O$ /n- $ZnO$  heterojunction diode for photovoltaic device, *J. Phys. D Appl. Phys.*, **40**, 3326 (2007).
- [30] H. Nawafune, Trend Remarks and Required Strategy on Plating Technologies, *J. Surf. Finish. Soc. Jpn.*, **66**, 403 (2015).

[31] O. Lupan, L. Chow, Th. Pauporté, L.K. Ono, B.R. Cuenya, G. Chai, Highly sensitive and selective hydrogen single-nanowire nanosensor, *Sens. Actuators B Chem.*, **173**, 772 (2012).

## **CHAPTER 2**

### **Electrochemical deposition of Zn-Ce-O films with controlled bandgap energy**

#### **2.1 Introduction**

##### **2.1.1 Electrochemical deposition using reduction reaction of nitrate**

Electrochemical deposition of crystalline ZnO thin films from aqueous solutions have been reported by Izaki et al.[1] in 1996, and are promoted by OH<sup>-</sup> generation originated from electrochemical reduction of the nitrate ion. In addition, CeO<sub>2</sub>[2],

MgO[3], Y<sub>2</sub>O<sub>3</sub>[4] and In<sub>2</sub>O<sub>3</sub>[5] were prepared by the electrochemical deposition process using the reduction reaction of nitrate ion. The oxide semiconductor films have been applied to important optical devices such as a light emitting diode, photosensors, and solar cells[6], and electrochemical deposition using the reduction reaction of the nitrate is an important method for optical and electric industries. Although a large amount of reports about electrochemical deposition using the reduction reaction of the nitrate ion were published, the electrochemical co-deposition of two or more oxide films was rarely reported. In this chapter, ZnO and CeO<sub>2</sub> were selected to propose the electrochemical co-deposition process for fabricating Zn-Ce-O films using the reduction-reaction of the nitrate ions.

### **2.1.2 Materials and objective of this study**

The electrochemical reaction for ZnO and CeO<sub>2</sub> preparations were specified as “A-type” potential-pH diagram explained in **Chapter 1**. In this chapter, I demonstrated that electrochemical deposition of ZnO-CeO<sub>2</sub> complex oxide (Zn-Ce-O) films based on the thermodynamic calculations for the critical pH value.

ZnO is an n-type semiconductor with 3.3 eV in bandgap energy[7] and are employed for industry, such as a passivation film of the reflector for LEDs[8], a transparent conductive film of touch panels and solar cells[9], and a scintillator to convert high-energy radiations to visible light[10]. The ZnO film has been prepared several techniques such as an RF magnetron sputtering, laser ablation, molecular beam epitaxy, sol-gel method, spray pyrolysis, and electrochemical deposition[1,11-15]. ZnO is an very important host material available to optical, electrical, and chemical applications,

and the characteristics are adjusted by introducing impurities and preparing ZnO-based complex oxide. Electrochemical deposition has several advantages over the gas-phase deposition process due to the ease in controlling impurity by solution formulation.

CeO<sub>2</sub> is an n-type semiconductor with 3.0-3.3 eV in bandgap energy[16]. The electrochemical deposition of CeO<sub>2</sub> was reported[2] by using the nitrate reduction reaction based on the critical pH value for acid-base reaction of Ce<sup>3+</sup>/Ce(OH)<sub>3</sub>. The Zn-Ce-O film has attracted increasing attention as the photocatalyst for cosmetic and self-cleaning applications. Both of ZnO and CeO<sub>2</sub> were deposited by increase in the pH value originated from the nitrate reduction reaction, and we perform the deposition of the Zn-Ce-O complex oxide by considering the solution formulation for Zn<sup>2+</sup>/ZnO and Ce<sup>3+</sup>/Ce(OH)<sub>3</sub> systems. The effect of the mixture is investigated by the structural and optical characterizations to approve the applicability to the optical application.

## **2.2 Experimental**

### **2.2.1 Thermodynamic calculation of electrochemical deposition for Zn-Ce-O films**

Figure 2.1 shows the potential-pH diagram of Zn-H<sub>2</sub>O and Ce-H<sub>2</sub>O systems cited from the reference[17]. ZnO and CeO<sub>2</sub> deposited by increasing the pH value in the vicinity of the substrate surface originated from the reduction reaction of the nitrate ion, and the critical pH of the acid-base reaction is very important in the deposition. In the solution containing Zn(NO<sub>3</sub>)<sub>2</sub>·6H<sub>2</sub>O and Ce(NO<sub>3</sub>)<sub>3</sub>·6H<sub>2</sub>O, Zn and Ce elements are dissolved as Zn<sup>2+</sup> and Ce<sup>3+</sup> cation, and the solutions showed an acidity depending on the activity.

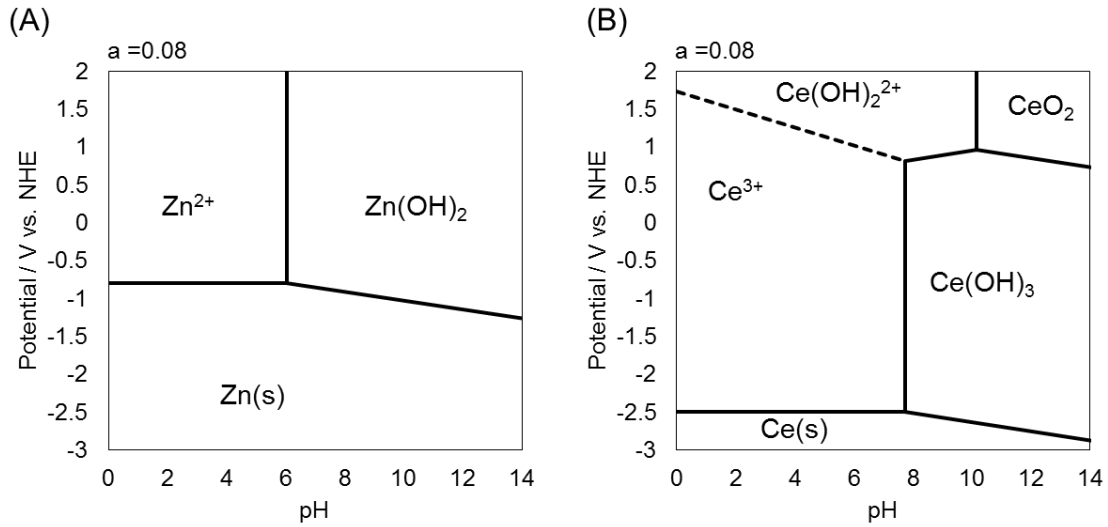


**Figure 2.1** Potential-pH diagram of Zn-H<sub>2</sub>O (A) and Ce-H<sub>2</sub>O (B) system at standard state drawn at 0.08 in activity.

The hydroxide ion, OH<sup>-</sup> are generated by the reduction-reaction of the nitrate ions in the solution, and the reaction is induced by applying a negative potential. The oxidization-reduction reaction of NO<sub>3</sub><sup>-</sup>/NO<sub>2</sub><sup>-</sup> is described as follows:[18]



The pH value before the polarization locates near the critical pH line inside the Zn<sup>2+</sup> region, and the condition on the substrate shifted from the Zn<sup>2+</sup> region to Zn(OH)<sub>2</sub> region by the pH raise induced by the reduction reaction of the nitrate ion. The critical value was calculated to be 6.0 for ZnO/Zn<sup>2+</sup> and 7.7 for Ce(OH)<sub>3</sub>/Ce<sup>3+</sup>, according to the formation reaction as follows:[18,19]





Figure 2.2 shows solubility curves of  $\text{Zn}(\text{OH})_2$  and  $\text{Ce}(\text{OH})_3$ . The horizontal axis represented the pH value of solutions, and vertical axis represented concentrations of  $\text{Zn}^{2+}$  and  $\text{Ce}^{3+}$  ions in solutions. The solid lines represented showed boundaries between metallic ions and the hydrate and hydroxides. The thermodynamic calculation was carried out using following equations.

$$0 = \Delta_r G^0 + 2.303RT \left( \log \frac{a_Y^y}{a_X^x} + h(\text{pH}) \right) + zFE \quad (1.8)$$

Since electrons were not needed for the acid-base reaction in the reaction,  $z = 0$ , equation (1.8) was specified to equation (1.8)';

$$0 = \Delta_r G^0 + 2.303RT \left( \log \frac{a_Y^y}{a_X^x} + h(\text{pH}) \right) \quad (1.8)'$$

As shown in equation (1.8), the standard Gibbs free energy at the equilibrium state is a function of the ion concentration and pH value. The relationship between the pH value and the concentrations of dissolved species at equilibrium state is called as solubility curves. A solubility curves were drawn by calculation about on solid phase species and all ionic species in the aqueous solution using the standard Gibbs free energy for the formation shown in Table 2.1. The solubility curve shows the maximum concentration of the dissolved species at the pH and the system of the chemical equilibrium (2.5), which is transformed from equation (1.3), is used for drawing solubility curves.

$$K = \exp \left( -\frac{\Delta_r G^0}{RT} \right) \quad (2.5)$$

Table 2.1 Standard Gibbs free energies of formation at 298.15 K used for drawing of the solubility curve of Zn(OH)<sub>2</sub> and Ce(OH)<sub>3</sub>[20,21].

Chemical species	$\Delta_f G^0$ [kJ/mol]
Zn <sup>2+</sup> (aq)	-147.06
Zn(OH) <sup>+</sup> (aq)	-330.1
Zn(OH) <sub>2</sub> <sup>0</sup> (aq)	-522.73
Zn(OH) <sub>3</sub> <sup>-</sup> (aq)	-694.22
Zn(OH) <sub>4</sub> <sup>2-</sup> (aq)	-858.52
Zn(OH) <sub>2</sub> (s)	-555.07
Ce <sup>3+</sup> (aq)	-717.915
Ce(OH) <sup>2+</sup> (aq)	-864.424
Ce(OH) <sub>2</sub> <sup>+</sup> (aq)	-1055.991
Ce(OH) <sub>4</sub> <sup>-</sup> (aq)	-1402.636
Ce(OH) <sub>3</sub> (s)	-1302.86
H <sub>2</sub> O(l)	-237.1

The solubility equilibrium between Zn(OH)<sub>2</sub> and Zn<sup>2+</sup>, Zn(OH)<sup>+</sup>, Zn(OH)<sub>2</sub><sup>0</sup>, Zn(OH)<sub>3</sub><sup>-</sup>, and Zn(OH)<sub>4</sub><sup>2-</sup> can be described by using the following reaction schemes.



The change in standard Gibbs free energy ( $\Delta_r G^0$ ) and equilibrium constant ( $K$ ) can be calculated using the chemical potentials of substances according to the reaction schemes.

The equation (2.2) is revised as equation (2.11):



$$\begin{aligned} \Delta_r G^0 &= \Delta_f G^0_{[\text{Zn}^{2+}]} + 2\Delta_f G^0_{[\text{OH}^-]} - (\Delta_f G^0_{[\text{Zn(OH)}_2]}) \\ &= -147.06 + 2(-157.24) - (-555.07) \\ &= 93.35 \text{ kJmol}^{-1} \end{aligned} \quad (2.12)$$

$$\log K = -\frac{\Delta_r G^0}{2.303RT} = -\frac{93.53 \times 1000}{2.303 \times 8.314 \times 298.15} = -16.38 \quad (2.13)$$

, when  $K$  in the equation (2.8) means  $K_{\text{sp}}$  of  $\text{Zn(OH)}_2$ ,  $K_{\text{sp(Zn(OH)}_2)}$ , and it is shown as follows:

$$K_{\text{sp(Zn(OH)}_2)} = 10^{-16.38} = 4 \cdot 10^{-17} \quad (2.14)$$

The calculated  $K_{\text{sp(Zn(OH)}_2)}$  value was almost agreed with the standard value,  $3 \cdot 10^{-17}$  [22], and solubility curves of  $\text{Zn(OH)}_2$  is determined by thermodynamic calculation originated from equation (2.6)-(2.10) in this study.

The standard Gibbs free energy for reaction scheme (2.6) was expressed as follows:

$$\begin{aligned} \Delta_r G^0 &= \Delta_f G^0_{[\text{Zn}^{2+}]} + 2\Delta_f G^0_{[\text{H}_2\text{O}]} - (\Delta_f G^0_{[\text{Zn(OH)}_2]} + 2\Delta_f G^0_{[\text{H}^+]}) \\ \Delta_r G^0 &= -147.06 + 2(-237.129) - (-555.07 + 2(0)) \\ \Delta_r G^0 &= -66.248 \text{ kJmol}^{-1} \end{aligned} \quad (2.15)$$

Since,  $\Delta_r G^0 = -RT \ln K = -2.303RT \log K$ ,

$$\log K = -\frac{\Delta_r G^0}{2.303RT} = -\frac{-66.248 \times 1000}{2.303 \times 8.314 \times 298.15} = 11.604 \quad (2.16)$$

when,  $K$  is equilibrium constant of equation (2.6). The activity is approximated to ion concentrations for all substances,  $a_{\text{Zn}^{2+}} \approx [\text{Zn}^{2+}]$  and  $a_{\text{H}^+} \approx [\text{H}^+]$ .  $[\text{Zn}^{2+}]$  and  $[\text{H}^+]$  represented the concentration of  $\text{Zn}^{2+}$  and  $\text{H}^+$ , and there is relation of  $\log[\text{H}^+] = \text{pH}$ .

$$\log K = \log \frac{[\text{Zn}^{2+}]}{[\text{H}^+]^2} = \log[\text{Zn}^{2+}] - 2\log[\text{H}^+] = \log[\text{Zn}^{2+}] + 2\text{pH} \quad (2.17)$$

$$11.604 = \log[\text{Zn}^{2+}] + 2\text{pH} \quad (2.18)$$

The pH dependences for the dissolved species,  $(\text{Zn}(\text{OH})^+)$ ,  $\text{Zn}(\text{OH})_2^0$ ,  $\text{Zn}(\text{OH})_3^-$ ,  $\text{Zn}(\text{OH})_4^{2-}$ , can be calculated in same manner, and results are summarized in table 2.2.

The solubility equilibrium between  $\text{Ce}^{3+}$ ,  $\text{Ce}(\text{OH})^{2+}$ ,  $\text{Ce}(\text{OH})_2^+$ ,  $\text{Ce}(\text{OH})_3^0$ , and  $\text{Ce}(\text{OH})_4^-$  can be described as the following reaction schemes:



The equation (2.19) is revised as equation (2.24):



$$\begin{aligned} \Delta_r G^0 &= \Delta_f G^0_{[\text{Ce}^{3+}]} + 3\Delta_f G^0_{[\text{OH}^-]} - (\Delta_f G^0_{[\text{Ce}(\text{OH})_3]}) \\ &= -717.915 + 3(-157.24) - (-1302.86) \end{aligned}$$

$$= 113.225 \text{ kJmol}^{-1} \quad (2.25)$$

$$\log K = -\frac{\Delta_r G^0}{2.303RT} = -\frac{93.53 \times 1000}{2.303 \times 8.314 \times 298.15} = -19.83 \quad (2.26)$$

, when  $K$  in the equation (2.26) means  $K_{sp}$  of  $\text{Ce(OH)}_3$ ,  $K_{sp(\text{Ce(OH)}_3)}$ , and it is shown as follows:

$$K_{sp(\text{Ce(OH)}_3)} = 10^{-19.83} = 1.5 \cdot 10^{-20} \quad (2.27)$$

Calculated  $K_{sp(\text{Ce(OH)}_3)}$  value is almost agreed with the standard value,  $1.6 \cdot 10^{-20}$  [22], and in this study, solubility curves of  $\text{Ce(OH)}_3$  is determined by thermodynamic calculation originated from equation (2.19)-(2.23).

The standard Gibbs energy of reaction for equation (2.19) was described as follows:

$$\begin{aligned} \Delta_r G^0 &= \Delta_f G^0_{[\text{Ce}^{3+}]} + 3\Delta_f G^0_{[\text{H}_2\text{O}]} - (\Delta_f G^0_{[\text{Ce(OH)}_3]} + 3\Delta_f G^0_{[\text{H}^+]}) \\ \Delta_r G^0 &= -717.915 + 3(-237.129) - (-1302.86 + 3(0)) \\ \Delta_r G^0 &= -126.44 \text{ kJmol}^{-1} \end{aligned} \quad (2.28)$$

Since,  $\Delta_r G^0 = -RT \ln K = -2.303RT \log K$ ,

$$\log K = -\frac{\Delta_r G^0}{2.303RT} = -\frac{-126.44 \times 1000}{2.303 \times 8.314 \times 298.15} = 22.08 \quad (2.29)$$

Here,  $K$  is equilibrium constant of equation (2.19). Activities are approximated to ion concentrations in dilute solutions,  $a_{\text{Ce}^{3+}} \approx [\text{Ce}^{3+}]$ .  $[\text{Ce}^{3+}]$  is  $\text{Ce}^{3+}$  concentration in solutions.

$$\log K = \log \frac{[\text{Ce}^{3+}]}{[\text{H}^+]^3} = \log[\text{Ce}^{3+}] - 3\log[\text{H}^+] = \log[\text{Ce}^{3+}] + 3\text{pH} \quad (2.30)$$

$$22.08 = \log[\text{Ce}^{3+}] + 3\text{pH} \quad (2.31)$$

The pH dependences of the dissolved species ( $\text{Ce}^{3+}$ ,  $\text{Ce}(\text{OH})^{2+}$ ,  $\text{Ce}(\text{OH})_2^+$ ,  $\text{Ce}(\text{OH})_3^0$ , and  $\text{Ce}(\text{OH})_4^-$ ), can be calculated in same manner, and are summarized in table 2.3.

The total concentrations of Zn and Ce dissolved species in solution are described as  $[\text{Zn}_{\text{total}}]$  and  $[\text{Ce}_{\text{total}}]$ :

$$[\text{Zn}_{\text{total}}] = [\text{Zn}^{2+}] + [\text{ZnOH}^+] + [\text{Zn}(\text{OH})_2^0] + [\text{Zn}(\text{OH})_3^-] + [\text{Zn}(\text{OH})_4^{2-}] \quad (2.32)$$

$$[\text{Ce}_{\text{total}}] = [\text{Ce}^{3+}] + [\text{Ce}(\text{OH})^{2+}] + [\text{Ce}(\text{OH})_2^+] + [\text{Ce}(\text{OH})_3^0] + [\text{Ce}(\text{OH})_4^-] \quad (2.33)$$

The solubility curves of  $\text{Zn}(\text{OH})_2$  and  $\text{Ce}(\text{OH})_3$  were expressed by using logarithmic value of  $[\text{Zn}_{\text{total}}]$  and  $[\text{Ce}_{\text{total}}]$  for vertical axis, and pH value for horizontal axis in Figure 2.2.

Table 2.2 Reaction formula and pH dependence of equilibrium concentration for dissolved Zn species

Reaction formula	$\Delta_r G^0$ (kJmol <sup>-1</sup> )	pH dependence of equilibrium concentration for dissolved species
$\text{Zn(OH)}_2 + 2\text{H}^+ = \text{Zn}^{2+} + 2\text{H}_2\text{O}$	-66.248	$\log[\text{Zn}^{2+}] = 11.604 - 2\text{pH}$
$\text{Zn(OH)}_2 + \text{H}^+ = \text{ZnOH}^+ + \text{H}_2\text{O}$	-21.759	$\log[\text{Zn(OH)}^+] = 3.8113 - \text{pH}$
$\text{Zn(OH)}_2 = \text{Zn(OH)}_2^0$	35.841	$\log[\text{Zn(OH)}_2^0] = -6.2773$
$\text{Zn(OH)}_2 + \text{H}_2\text{O} = \text{Zn(OH)}_3^- + \text{H}^+$	91.87	$\log[\text{Zn(OH)}_3^-] = -16.092 + \text{pH}$
$\text{Zn(OH)}_2 + 2\text{H}_2\text{O} = \text{Zn(OH)}_4^{2-} + 2\text{H}^+$	164.77	$\log[\text{Zn(OH)}_4^{2-}] = -28.861 + 2\text{pH}$

Table 2.3 Reaction formula and pH dependence of equilibrium concentration for dissolved Ce species

Reaction formula	$\Delta_r G^0$ (kJmol <sup>-1</sup> )	pH dependence of equilibrium concentration for dissolved species
$\text{Ce(OH)}_3 + 3\text{H}^+ = \text{Ce}^{3+} + 3\text{H}_2\text{O}$	-126.44	$\log[\text{Ce}^{3+}] = 22.149 - 3\text{pH}$
$\text{Ce(OH)}_3 + 2\text{H}^+ = \text{Ce(OH)}_2^+ + 2\text{H}_2\text{O}$	-35.822	$\log[\text{Ce(OH)}_2^+] = 6.275 - 2\text{pH}$
$\text{Ce(OH)}_3 + \text{H}^+ = \text{Ce(OH)}_2^0 + \text{H}_2\text{O}$	9.74	$\log[\text{Ce(OH)}_2^0] = -1.706 - 2\text{pH}$
$\text{Ce(OH)}_3 = \text{Ce(OH)}_3^0$	65.45	$\log[\text{Ce(OH)}_3^0] = -11.466$
$\text{Ce(OH)}_3 + \text{H}_2\text{O} = \text{Ce(OH)}_4^- + \text{H}^+$	137.353	$\log[\text{Ce(OH)}_4^-] = -24.06 + \text{pH}$

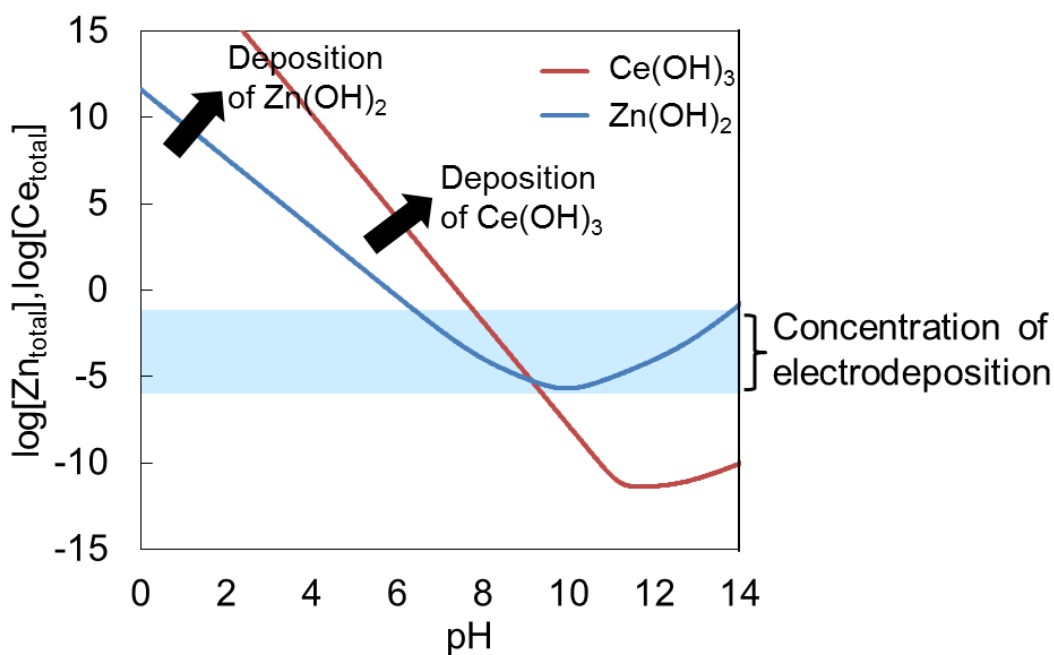


Figure 2.2 Relationship between solubilities of  $\text{Zn(OH)}_2$  and  $\text{Ce(OH)}_3$  and pH.

Light blue area represented in the Figure 2.2 region, gave the condition to prepare Zn-Ce-O film due to the close solubilities of  $\text{Zn(OH)}_2$  and  $\text{Ce(OH)}_3$ . The critical pH values of the acid-base reaction for  $\text{Zn}^{2+}/\text{ZnO}$  system was 6.51 at 0.04 mol/L, and the critical pH values of the acid-base reaction for  $\text{Ce}^{3+}/\text{Ce(OH)}_3$  system was 7.85 at 0.04 mol/L concentration.

### 2.2.2 Experimental procedure

The substrate was a Cu plate ( $2 \times 2 \text{ cm}^2$ ) coated Ag by electrochemical deposition. The Cu plate was degreased at a current density of  $-10 \text{ mA/cm}^2$  in an electrolyte containing 60 g/L KOH and 30 g/L  $\text{K}_4\text{P}_2\text{O}_7$  for 1 minute and was washed with distilled water (15  $\text{M}\Omega\text{cm}$  with Milli-pore), prior to electrochemical deposition. Then, activation of Cu

substrate was carried out by the immersion in 10% H<sub>2</sub>SO<sub>4</sub> solution for 30 seconds. Electrolysis for the Ag electrochemical deposition was performed SILVREX 50 (EEJA) containing AgNO<sub>3</sub>. Pt foil was used as the counter electrode, and the electrochemical deposition was carried out at 80 mA/cm<sup>2</sup> in current density for 5 min.

The solution for electrochemical deposition of Zn-Ce-O films was prepared by dissolving Zn(NO<sub>3</sub>)<sub>2</sub>·6H<sub>2</sub>O and Ce(NO<sub>3</sub>)<sub>3</sub>·6H<sub>2</sub>O into a deionized water. Total ion concentration was set at a constant value of 0.08 mol/L, and Ce(NO<sub>3</sub>)<sub>3</sub>·6H<sub>2</sub>O concentration in the solution were set at 0, 0.027, 0.040, 0.053 and 0.08 mol/L in order to change the Ce molar ratio (Ce/(Zn+Ce)) to 0, 33, 50, 67, and 100%, respectively. Deionized water (15 MΩcm with Milli-pore) was used as a media, and the pH value of solutions ranged from 4.0 to 5.4. The electrochemical deposition of Zn-Ce-O films were carried out using conventional three electrode cell with Ag/Cu substrate, Pt foil, and Ag/AgCl electrode (+0.199 V vs. NHE) as working, counter, and reference electrodes. Temperature was set at 63°C, and the potential was set at -1.1 and -0.9 V. The electric charge was set at 0.5 C/cm<sup>2</sup>. Electrochemical deposition were performed at -1.1 V for Zn(NO<sub>3</sub>)<sub>2</sub>·6H<sub>2</sub>O solution, and -0.9 V for Ce(NO<sub>3</sub>)<sub>3</sub>·6H<sub>2</sub>O solution, respectively.

### **2.2.3 Characterization of Zn-Ce-O films**

Surface observations were carried out with a field emission scanning electron microscope (FE-SEM). Accelerating voltage and emission current were taken as 3.0 kV and 10 mA, respectively. In addition, elemental analysis was carried out using an energy dispersive X-ray spectroscopy (EDX, EMAX ENARGY: EX-250; X-Max80,

HORIBA) attached to the FE-SEM. In the EDX analysis, the accelerating voltage and emission current were set at 7.0 kV and 10 mA, respectively. The structures of the deposited films were identified by an X-ray diffraction (XRD: RINT2500, Rigaku) technique with a monochromatized Cu K $\alpha$  radiation at 40 kV and 200 mA. Optical reflectance spectra was recorded by a spectrophotometer (UV-Vis-NIR: U4100, HITACHI Hightech) with the reference of Al<sub>2</sub>O<sub>3</sub>.

## **2.3 Results and discussion**

### **2.3.1 Composition of Zn-Ce-O films**

Table 2.1 shows molar content of Ce, Zn, and O and Ce molar ratio of Ce to metal (Ce/(Zn+Ce)) of Zn-Ce-O films. The film prepared in the Zn(NO<sub>3</sub>)<sub>2</sub>·6H<sub>2</sub>O solution contained only Zn and O elements, and the ratio for Zn:O is approximately 50:50 in agreement with the stoichiometry. The film prepared in Ce(NO<sub>3</sub>)<sub>3</sub>·6H<sub>2</sub>O solution contained only Ce and O elements, and the ratio for Ce:O is approximately 40:60. The oxygen deficiency against the stoichiometric value was attributed to contain the Ce<sup>3+</sup> state in the films, as already reported in CeO<sub>2</sub> films prepared by nitrate reduction[2]. The film prepared by the Ce 33, 50 and 67% solutions contained Zn, Ce, and O elements indicating the formation of Zn-Ce-O films. In all Zn-Ce-O films, the Zn molar content is higher than the Ce molar content. The Ce content in the films changed from 0 to 43 mol% depending on the Ce concentration in solutions, and the Ce concentration in solutions showed a great influence for the Ce molar content in the films. The Ce molar content in the Zn-Ce-O films prepared at -0.9 V slightly higher than these at -1.1 V, as shown in table 2.1.

Table 2.1 Atoms molar concentration and Ce atom molar concentration by total metal atoms in the films (Ce/(Zn+Ce)) of deposits prepared by each conditions from EDX analysis.

Ce/(Zn+Ce) in the solution(%)	Potential of deposition (V vs. Ag/AgCl)	Molar content(mol%)			Ce/(Zn + Ce) in the deposits(mol%)
		Zn	Ce	O	
0	- 1.1	49.89	0.00	50.11	0
	- 0.9	48.79	2.81	48.40	
33	- 1.1	45.21	2.80	51.99	6
	- 0.9	33.41	8.07	58.51	
50	- 1.1	33.60	8.46	57.94	20
	- 0.9	21.27	10.16	68.56	
67	- 1.1	22.44	13.51	64.05	38
	- 0.9	0.00	39.61	60.39	
100					100

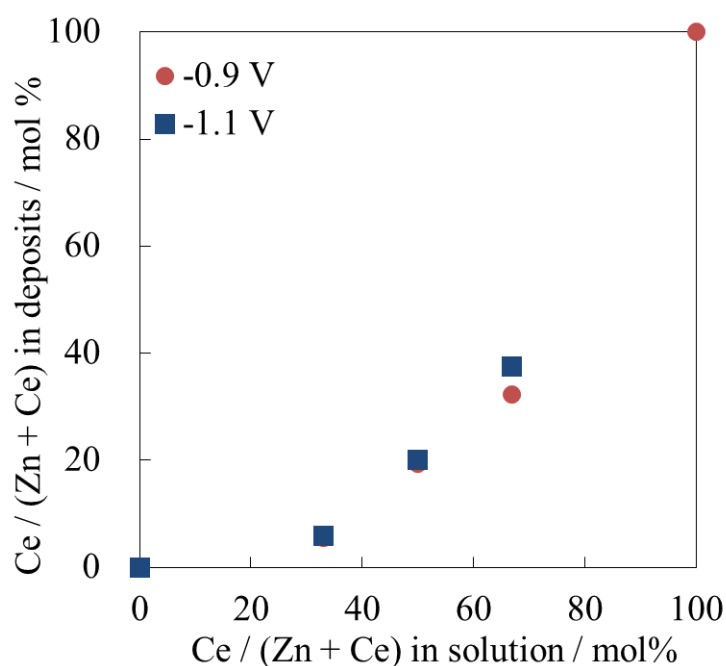


Figure 2.3 Correlation between Ce ions molar concentration by total metal ions in the solution ( $Ce/(Zn+Ce)$ ) and Ce ions molar concentration by total metal ions in the deposits ( $Ce/(Zn+Ce)$ ) from EDX analysis.

In electrochemical deposition using the reduction reaction of nitrate ion, the deposition potential strongly affected the pH value in the vicinity of the substrate, and it was reported that the pH value in the vicinity of the substrate increased to 10.5 and 11.5 at  $-0.9$  and  $-1.1$  V for the electrode potential at  $-0.9$  and  $-1.1$  V, respectively[23]. The Zn-Ce-O film prepared at  $-1.1$  V showed higher Ce content compared with that at  $-0.9$  V, because of the change between the critical pH value for  $Zn^{2+}/ZnO$  and  $Ce^{3+}/Ce(OH)_3$  system and the pH value in the vicinity of substrate. The Ce content in Zn-Ce-O films depended on the Ce concentration in solutions and pH value in the vicinity of the substrate. Figure 2.3 shows correlation between the Ce molar ratio ( $Ce/(Zn+Ce)$ ) in the solution and Ce molar content ratio ( $Ce/(Zn+Ce)$ ) in the Zn-Ce-O films.

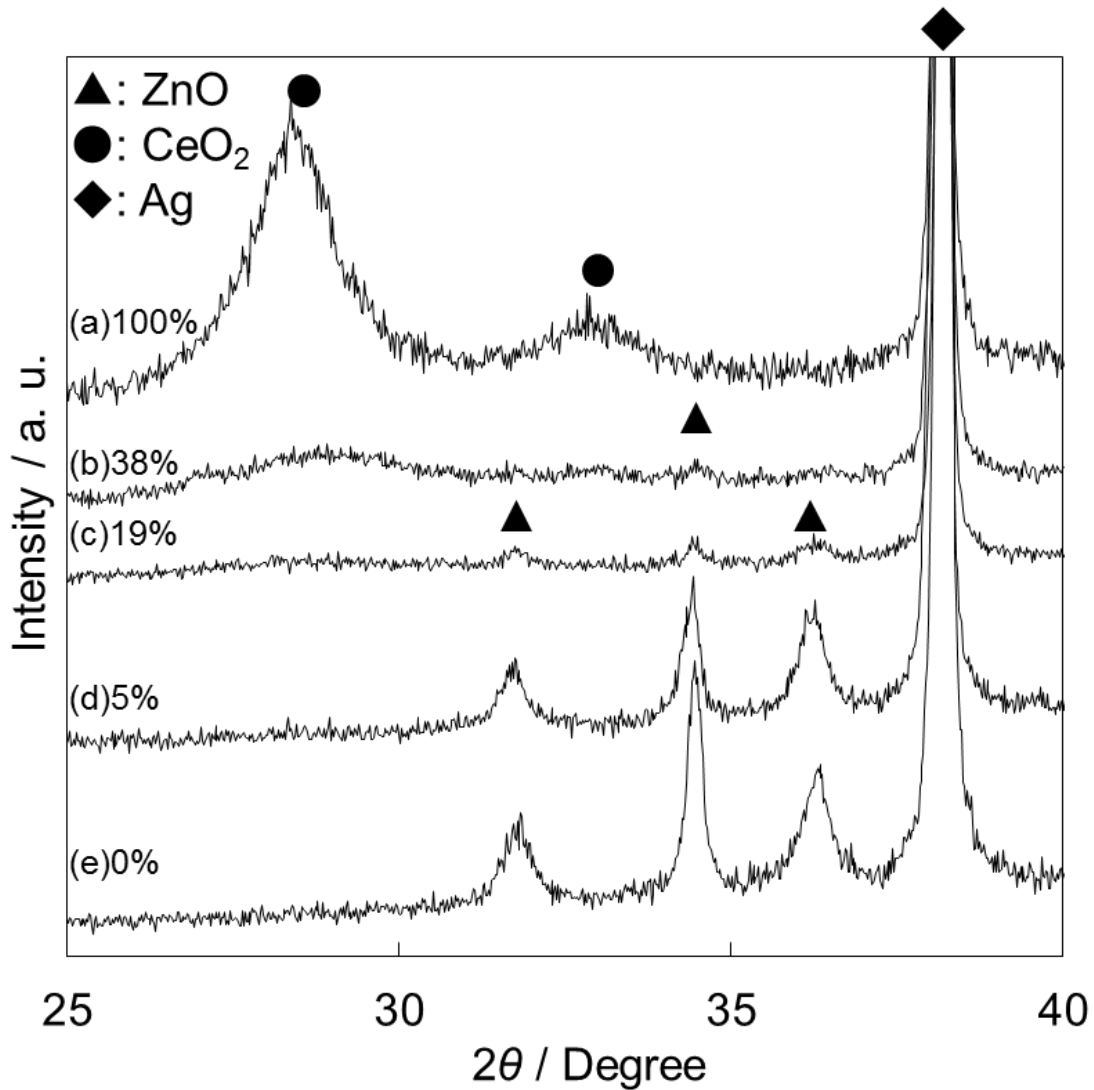


Figure 2.4 X-ray diffraction patterns Zn-Ce-O films with Ce content of 100(a), 38(b), 19(c), 5(d), and 0 mol%(e).

### 2.3.2 Structural characterization of Zn-Ce-O films

Figure 2.4 shows the X-ray diffraction patterns for Zn-0~100% Ce-O films. The three peaks at 31.84, 34.46 and 36.34° in the Ce-free ZnO film were assigned as (100), (002) and (101) planes of wurtzite structure ZnO, respectively, and the peak at 38.18°

was assigned as the Ag(111) plane. Broadened peaks at 28 and 33° observed in the Zn-free CeO<sub>2</sub> film were assigned as (111) and (200) planes of a cubic CeO<sub>2</sub>, respectively. Full width at half maximum (FWHM) of X-ray diffraction peaks relates to the grain size and inhomogenous strain[24], and broadened CeO<sub>2</sub> peaks indicated the small grain size and presence of inhomogenous strain. The inhomogenous strain was originated from the incorporate of the Ce<sup>3+</sup> ion in addition to Ce<sup>4+</sup> ion and the difference in ionic radius. The intensity and diffraction angle of XRD peaks changed depending on the Ce content for Zn-5~38% Ce-O film. XRD peaks assigned as ZnO were observed clearly on XRD patterns for Zn-5~20% Ce-O films. Intensity of XRD peaks of ZnO decreased with increase in Ce content, and very weak ZnO (002) peak was observed in the Zn-38% Ce-O film. Since, the ZnO (002) peak was stronger than other ZnO peaks in the Ce-free ZnO film, the ZnO film showed a (0002) preferred orientation, due to the lowest surface energy of (0002) plane in wurtzite ZnO[25]. In Zn-5~38% Ce-O films, the intensity of the ZnO (002) peak decreased compared with (100) and (101) planes, suggesting the changing preferred orientation. The decrease in the grain size and increase in inhomogenous strain were generated with increase in the Ce content from the increase in the FWHM value of ZnO peaks. A slight shift of ZnO peaks to lower angle side occurred by containing the Ce element, indicating the change in the lattice constant. Broadened CeO<sub>2</sub> (111) peak was observed around 28° in Zn-19-38%Ce-O film in addition to ZnO peaks, and the intensity increased with increase in the Ce content. The CeO<sub>2</sub> (111) peak shifted to higher angle side by 0.3-0.7° compared with that for the Zn-free CeO<sub>2</sub> film.

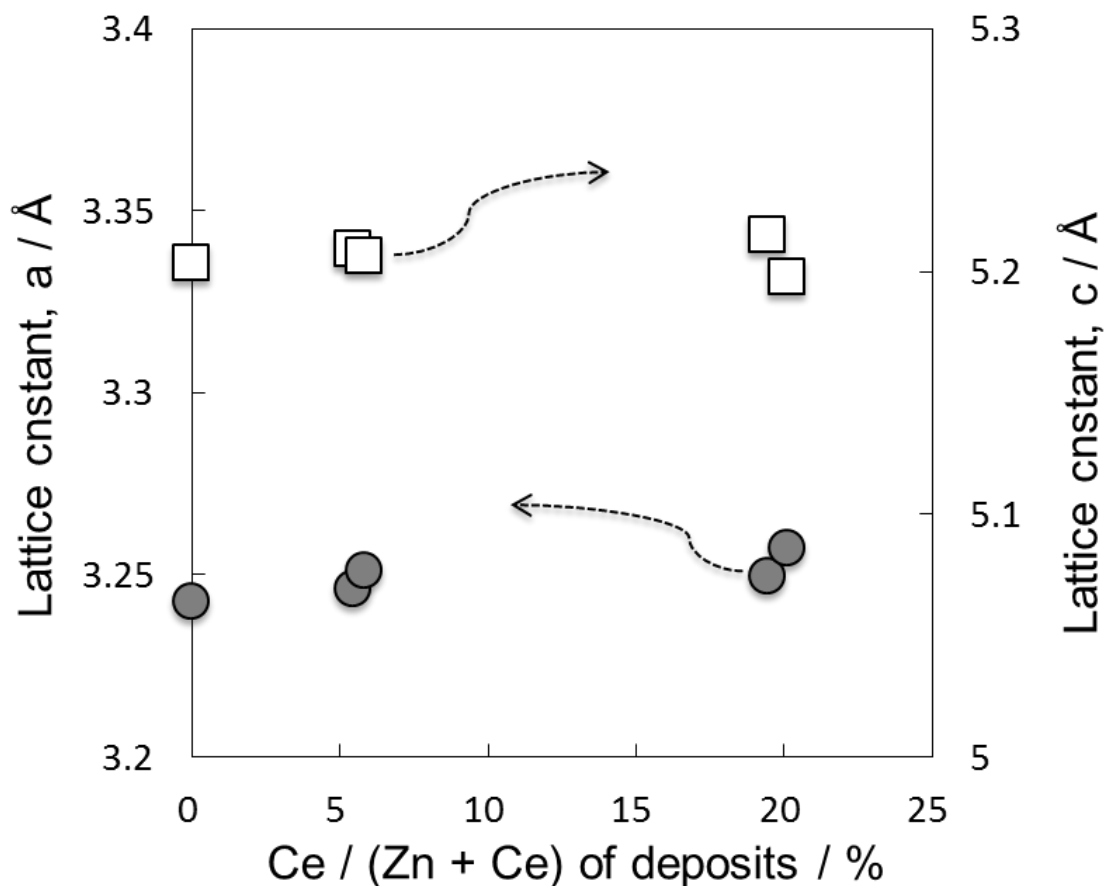


Figure 2.5 Effects of the Ce content on lattice constant a and c of ZnO films in ZnO and Zn-Ce-O films.

As mentioned above, Zn-0~6% Ce-O films were identified as single ZnO phase, and Zn-19~43% Ce-O films were identified as a mixture of ZnO and CeO<sub>2</sub>.

Correlation between the Ce content and lattice constants of ZnO phase in Zn-Ce-O films was shown in Figure 2.5. Lattice constants a and c of Ce-free ZnO film were calculated to be  $a = 3.243 \text{ \AA}$ ,  $c = 5.203 \text{ \AA}$  and almost agreed to  $a = 3.2496 \text{ \AA}$ ,  $c = 5.2065 \text{ \AA}$  for standard values. The lattice constant c of ZnO phase showed almost constant

value irrespective of Ce content in Zn-Ce-O films, but the lattice constant  $a$  of ZnO phase increased with increase in the Ce content in Zn-Ce-O films, and the cell volume increased. The increase in the cell volume indicated that the  $Zn^{2+}$  site in ZnO was substituted by  $Ce^{3+}$  and  $Ce^{4+}$ , due to the ionic radius of 0.60 Å for  $Zn^{2+}$  ion in ZnO, of 1.01 Å for  $Ce^{3+}$  ion and of 0.87 Å for  $Ce^{4+}$  ion. The change in the lattice constant  $a$  and cell volume indicated the formation of ZnO solid solution by substituting the  $Zn^{2+}$  to Ce ions, and the formation reflected the increase in the FWHM and change in the preferred orientation.

Figure 2.6 shows the correlation between the Ce content and lattice constant of  $CeO_2$  in Zn-Ce-O films and  $CeO_2$ . Lattice constant of Zn-free  $CeO_2$  was calculated to be 5.43 Å, which almost agreed with the standard value. Lattice constant of Zn-32-38% Ce films showed a value around 5.35 Å and decreased to 5.31 Å for Zn-20% Ce film. The decrease in the lattice constant with the Ce content indicated the formation of  $CeO_2$  solid solution by substituting Ce to Zn ion.

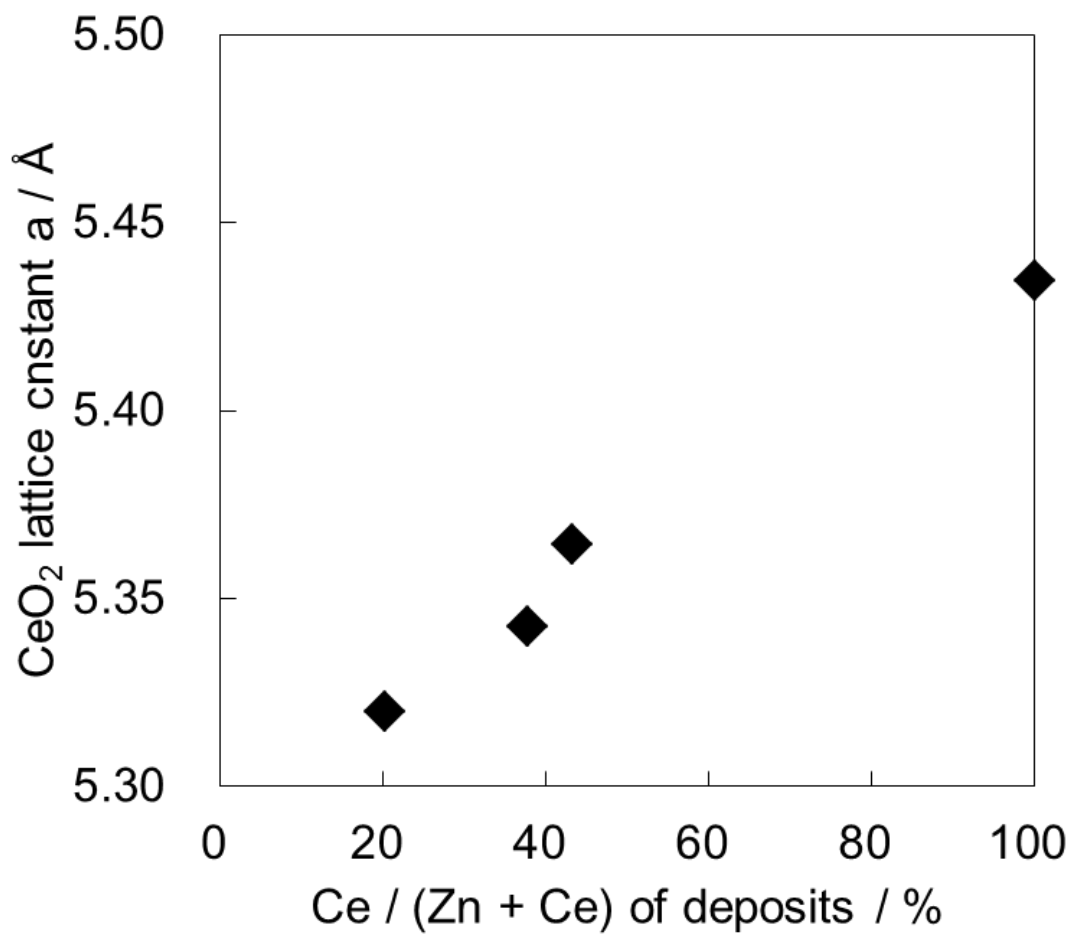


Figure 2.6 Effect of the Ce content on the lattice constant of CeO<sub>2</sub> in Zn-Ce-O films.

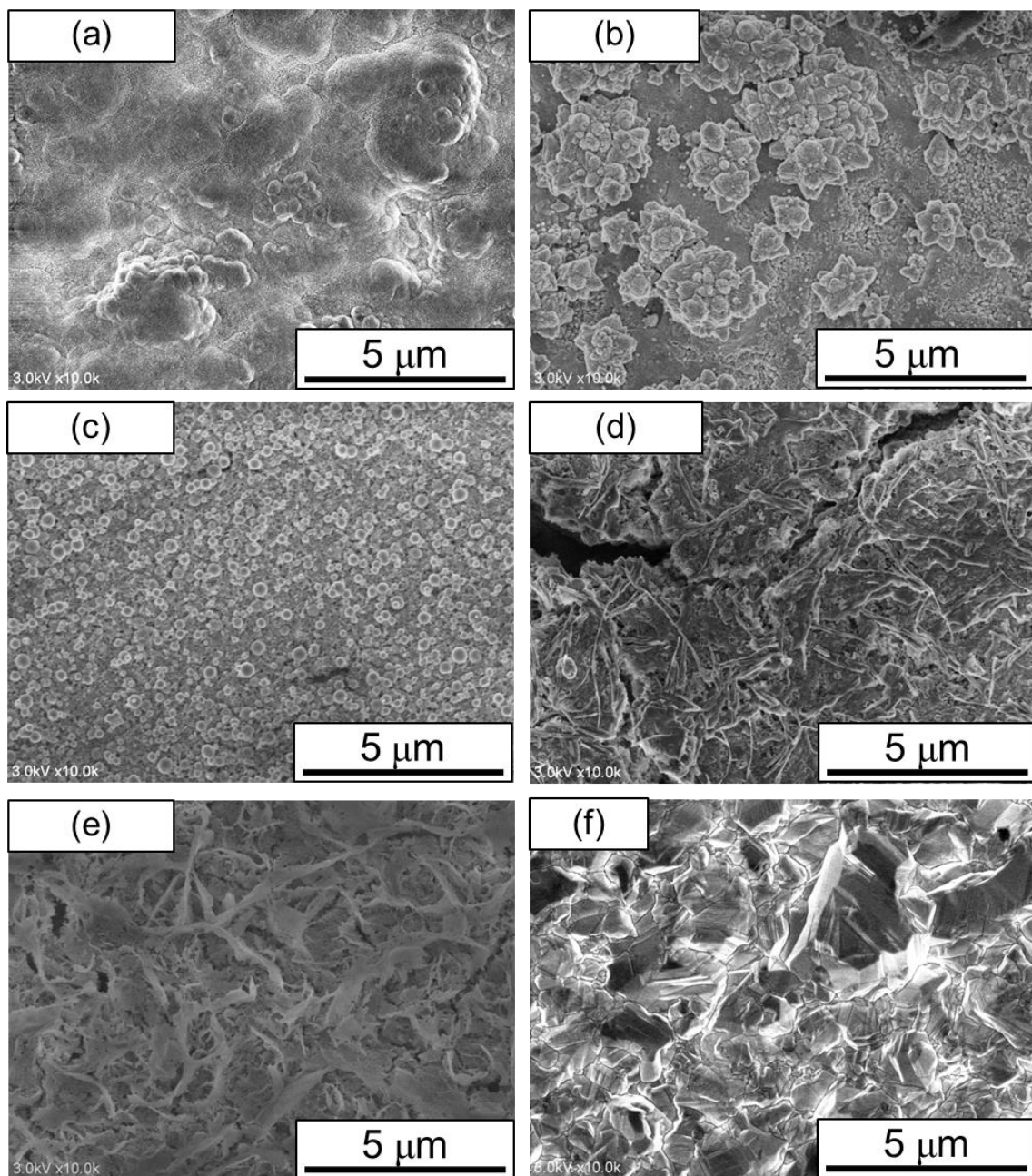


Figure 2.7 SEM images of surface of Zn-Ce-O films with Ce content of 0(a), 6(b), 20(c), 38(d), 100%(e) and bare Ag film(f).

Surface morphologies of the Ag substrate before and after-depositions of Zn-0~100% Ce-O films were shown in Figure 2.7. The Ag substrate was composed of aggregate of angular grains of 1-4  $\mu\text{m}$  in size and had very roughed surface originated from the roughness of Cu plate. The Cu plate was covered entirely with the Ag grains. The surface of the Ce-free ZnO film was composed of the aggregate of granular grains of 0.05-0.5  $\mu\text{m}$  in size. The surface of the Zn-free  $\text{CeO}_2$  film was composed of aggregate of plate-like grains of 5  $\mu\text{m}$  in length and covered over the Ag substrate, but some cracks was observed between grains. The Zn-6~20% Ce-O films were composed of the aggregate of granular grains of 10-100 nm in size, and cracks and defects was not observed on the image. The surface morphology of Zn-38% Ce-O film was different from the Zn-6%Ce-O film and was composed of aggregate of plate-like grains of 2-5  $\mu\text{m}$  in size. The Zn-38% Ce-O film showed some cracks similar to  $\text{CeO}_2$  film.

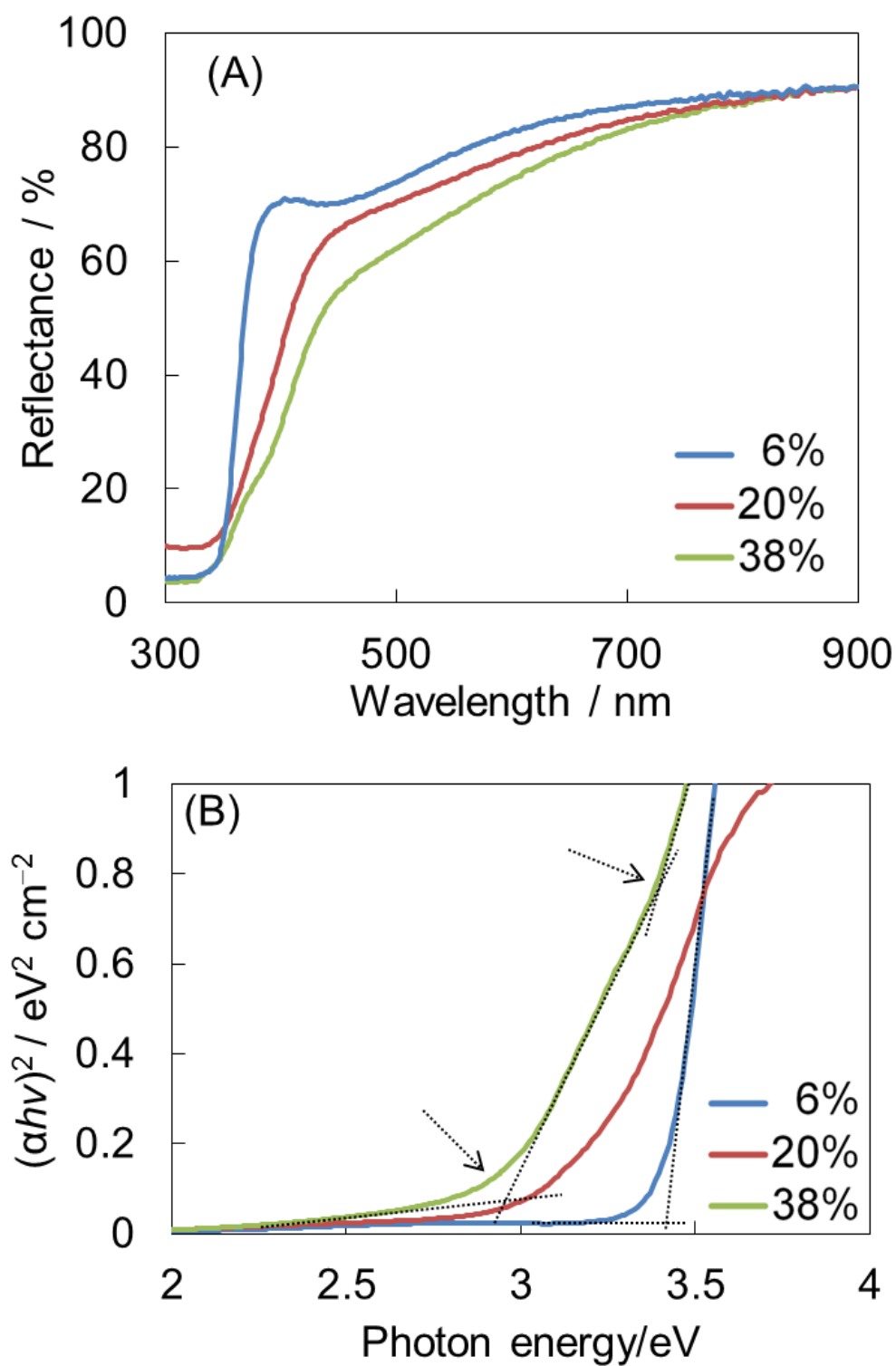


Figure 2.8 Reflectance(A) for Zn-Ce-O films with Ce content of 6, 20 and 38 mol%, and the correlation between the absorption coefficient and photon energy(B).

### 2.3.3 Optical property of Zn-Ce-O films

Figure 2.8 shows reflectance spectra for Zn-6, 20, 38% Ce-O films and the correlation between the absorption coefficient and photon energy. Zn-6~38% Ce-O films showed reflectance over 60% or more at 500-900 nm in wavelength, and the reflectance increased with increase in the wavelength. Although it was not clear whether CeO<sub>2</sub> was direct or indirect transition type semiconductor[26], relationships between the square of absorption coefficient, which was calculated from the reflectance and film thickness, and photo energy, due to the direct transition type semiconductor for ZnO. The absorption edge shifted to lower energy side with increase in the Ce ratio in Zn-Ce-O films. The bandgap energy was estimated by extrapolating linear part to the background value. A linear part was observed for the Zn-6% Ce-O film, and two linear parts were observed for Zn-20, 38% Ce-O films as represented by two arrows, where band gap energies were estimated from two linear parts. The existence of two absorption edge indicated the mixture of two different bandgap energy as already reported for Cu<sub>2</sub>O-CuO system[27]. Existence of two oxide semiconductors in Zn-20, 38%Ce-O films was consistent with the result of XRD measurement.

Figure 2.9 shows effects of the Ce content on the bandgap energy for Zn-Ce-O films. The bandgap energy of the Ce-free ZnO film was 3.42 eV, and the bandgap energy of the Zn-free CeO<sub>2</sub> was 3.25 eV. Bandgap energy of the Zn-Ce-O films decreased with increase in the Ce content. There were two tendencies represented by (1) and (2). The bandgap energy decreased from 3.4 eV for the Ce-free ZnO to 3.2 eV for the Zn-32% Ce-O film on line (1).

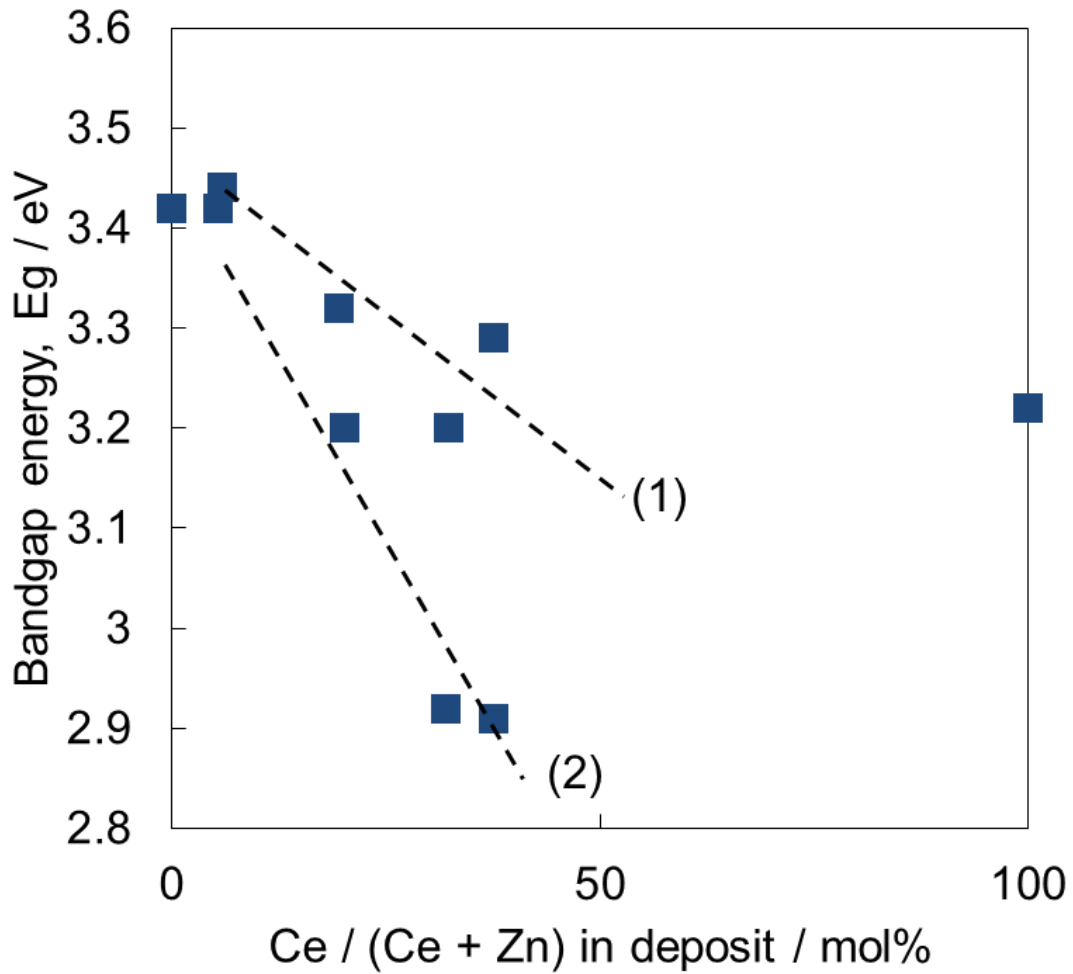


Fig. 2.9 Effects of the Ce content on bandgap energies for Zn-Ce-O films.

The bandgap energy decreased from 3.4 eV for Ce-free ZnO to 2.9 eV for Zn-32% Ce-O film. XRD measurement indicated that the Zn-Ce-O films was composed of  $\text{Ce}^{3+}$ ,  $\text{Ce}^{4+}$ :ZnO solid solution (Ce:ZnO) and  $\text{Zn}^{2+}$ : $\text{CeO}_2$  solid solution (Zn: $\text{CeO}_2$ ), but the relationship between the line (1), (2) and Ce:ZnO, Zn: $\text{CeO}_2$  solid solutions was not clear from the results obtained here. The changes in band gap energy by impurity introduction were already reported for many semiconductor materials. It was predicted

theoretically and confirmed experimentally that the bandgap energy of the  $\text{Zn}(\text{O}_{1-x},\text{S}_x)$  with wurtzite lattice as that for ZnO and ZnS decreased from 3.3 eV for ZnO to 2.8 eV for  $\text{Zn}(\text{O}_{0.5},\text{S}_{0.5})$  and then increased to 3.76 eV for ZnS[28]. The  $\text{Zn}(\text{O},\text{S})$  was ZnO solid solution by substituting O site by S element or ZnS solid solution by substituting S site by O element, and the lattice constant changed continuously depending on the composition. The lattice constants of Ce:ZnO and Zn:CeO<sub>2</sub> changed depending on the Ce content. The relationship between the bandgap energy and lattice constant was clearly observed for  $\text{Cu}(\text{In},\text{Ga})(\text{S},\text{Se})_2$  compound as already accepted. The change in the bandgap energy of the Ce:ZnO and Zn:CeO<sub>2</sub> solid solutions closely related to the lattice constant by forming solid solution.

## 2.4 Conclusions

In summary, ZnO-CeO<sub>2</sub> composite oxide (Zn-Ce-O) films were prepared on Ag substrate by electrochemical deposition in aqueous solutions containing Zn(NO<sub>3</sub>)<sub>2</sub> · 6H<sub>2</sub>O and Ce(NO<sub>3</sub>)<sub>3</sub> · 6H<sub>2</sub>O. The solubility curves for Zn<sup>2+</sup>/Zn(OH)<sub>2</sub> and Ce<sup>3+</sup>/Ce(OH)<sub>3</sub> systems were calculated using thermodynamics, and the solution formulation was thermodynamically designed by adjusting the critical pH values for both systems. The Ce concentration in solutions and deposition potential relating the pH value in the vicinity of substrate influenced the Ce content in Zn-Ce-O films. Zn-Ce-O films were identified as a wurtzite ZnO solid solution containing Ce (Ce:ZnO) at 5% Ce, and a mixture of Ce:ZnO and CeO<sub>2</sub> solid solution containing the Zn(Zn:CeO<sub>2</sub>) at 20-43% Ce. Zn-Ce-O films showed the reflectance over 60% in visible light region, and the bandgap energy changed from 3.4 eV to 2.9 eV depending on the Ce content.

## REFERENCE

- [1] M. Izaki, T. Omi, Transparent zinc oxide films prepared by electrochemical reaction, *Appl. Phys. Lett.*, **68**, 2439 (1996).
- [2] M. Izaki, M. Ishikawa, M. Inoue, Preparation of Rare-Earth Metal Oxide Films through Electrochemical Reaction, *Proc. Electrochem. Soc.*, **2000**, 1 (2000).
- [3] G. Zou, R. Liu, W. Chem, Highly textural lamellar mesostructured magnesium hydroxide via a cathodic electrodeposition process, *Mater. Lett.*, **61**, 1990 (2007).
- [4] A.A.M. Barmi, M. Aghazadeh, H.M. Shiri, F. Ghorab, Cathodic electrodeposition and characterization of nanostructured  $Y_2O_3$  from nitrate solution. Part I: Effect of current density, *Rus. J. Electrochemi.*, **49**, 583 (2013).
- [5] R. Henriquez, E. Munoz, E.A. Dalchiele, R.E. Marotti, F. Martin, D. Leinen, J.R. Ramos-Barrado, H. Gomez, Electrodeposition of  $In_2O_3$  thin films from a dimethylsulfoxide based electrolytic solution, *Physica Status Solidi A Appl. Res.*, **210**, 297 (2013).
- [6] D.C. Look, Recent advances in ZnO materials and devices, *Mater. Sci. Eng. B Solid State Mater. Adv. Technol.*, **80**, 383 (2001).
- [7] S.J. Pearton, D.P. Norton, K. Ip, Y.W. Heo, T. Steiner, Recent progress in processing and properties of ZnO, *Prog. Mater. Sci.*, **50**, 293 (2005).
- [8] H. Nawafune, Trend Remarks and Required Strategy on Plating Technologies, *J. Surf. Finish. Soc. Jpn.*, **66**, 403 (2015).

- [9] H.K. Park, J.W. Kang, S.I. Na, D.Y. Kim, H.K. Kim, Characteristics of indium-free GZO/Ag/GZO and AZO/Ag/AZO multilayer electrode grown by dual target DC sputtering at room temperature for low-cost organic photovoltaics, *Solar Ener. Mater. Solar Cells*, **93**, 1994 (2009).
- [10] P.J. Simpson, R. Tjossem, A.W. Hunt, K.G. Lynn, V. Munné, Superfast timing performance from ZnO scintillators, *Nucl. Instrum. Methods Phys. Res. A*, **505**, 82 (2003).
- [11] P.F. Carcia, R.S. McLean, M. H. Reilly, G. Nunes Jr., Transparent ZnO thin-film transistor fabricated by rf magnetron sputtering, *Appl. Phys. Lett.*, **82**, 1117 (2003).
- [12] S.J. Henley, M.N.R. Ashfold, D. Cherns, The growth of transparent conducting ZnO films by pulsed laser ablation, *Surf. Coat. Technol.*, **177**, 271 (2004).
- [13] D.M. Bagnall, Y.F. Chen, M.Y. Shen, Z. Zhu, T. Goto, T. Yao, Room temperature excitonic stimulated emission from zinc oxide epilayers grown by plasma-assisted MBE, *J. Cryst. Growth*, **184**, 605 (1998).
- [14] J.H. Lee, K.H. Ko, B.O. Park, Electrical and optical properties of ZnO transparent conducting films by the sol-gel method, *J. Cryst. Growth*, **247**, 119 (2003).
- [15] F. Paraguay, W. Estrada, D.R. Acosta, E. Andrade, M. Yoshida, Growth, structure and optical characterization of high quality ZnO thin films obtained by spray pyrolysis, *Thin Solid Films*, **350**, 192 (1999).
- [16] N. Shehata, K. Meehan, M. Hudait, N. Jain, Control of oxygen vacancies and Ce<sup>+3</sup> concentrations in doped ceria nanoparticles via the selection of lanthanide element, *J. Nanopart. Res.*, **14**, 1173 (2012).

- [17] M. pourbaix, Atlas of Electrochemical Equilibria in Aqueous Solutions, NACE, Houston, TX, 1974.
- [18] M. Izaki, R. Chizaki, T. Saito, K. Murata, J. Sasano, T. Shinagawa, Hybrid ZnO/Phthalocyanine Photovoltaic Device with Highly Resistive ZnO Intermediate Layer, ACS Appl. Mater. Interfaces, **5**, 9386 (2013).
- [19] H.I. Chen, H.Y. Chang, Synthesis of nanocrystalline cerium oxide particles by the precipitation method, Ceram. Int., **31**, 795 (2005).
- [20] D. Wagman, W. H. Evans, V. B. Parker, R. H. Schumm, I. Halow, S. M. Bailey, K. L. Churney, R. L. Nuttall ; J. Phys. Chem. Ref. Data, Vol. 11, Suppl. 2 The NBS Tables of Chemical Thermodynamic Properties, Selected Values for Inorganic and C1 and C2 Organic Substances in SI Units, NBS, Washington, DC, USA, 1982.
- [21] J.R. Haas, E.L. Shock, D.C. Sassani, Rare earth elements in hydrothermal systems: Estimates of standard partial molal thermodynamic properties of aqueous complexes of the rare earth elements at high pressures and temperatures, Geochim. Cosmochim. Acta, **59**, 4329 (1995).
- [22] J.G. Speight, Lange's Handbook of Chemistry SIXTEENTH EDITION, CD&W Inc., Laramie, Wyoming, 2005.
- [23] M. Nobial, O. Devos, O. R. Mattos, B. Tribollet, The nitrate reduction process: A way for increasing interfacial pH, J. Electroanal. Chem. Interfacial Electrochem., **600**, 87 (2006).
- [24] B.D. Cullity & S.R. Stock; Elements of X-Ray Diffraction, 3rd Ed., Prentice-Hall Inc., NJ, 2001.

- [25] N. Fujimura, T. Nishihara, S. Goto, J. Xu, T. Ito, Control of preferred orientation for ZnO<sub>x</sub> films: control of self-texture, *J. Cryst. Growth*, **130**, 269 (1993).
- [26] M. Izaki, T. Saito, M. Chiugane, M. Ishikawa, J. Katayama, M. Inoue, M. Yamashita, Low temperature deposition of cerium dioxide film by chemical reaction, *J. Mater. Chem.*, **11**, 1972 (2001).
- [27] M. Izaki, T. Shinagawa, K. Mizuno, Y. Ida, M. Inaba A. Tasaka, Electrochemically constructed p-Cu<sub>2</sub>O/n-ZnO heterojunction diode for photovoltaic device, *J. Phys. D*, **40**, 3326 (2007).
- [28] C. Persson, C. Platzer-Björkman, J. Malmström, T. Törndahl, M. Edoff, Strong Valence-Band Offset Bowing of ZnO<sub>1-x</sub>S<sub>x</sub> Enhances p-Type Nitrogen Doping of ZnO-like Alloys, *Phys. Rev. Lett.*, **97**, 146403 (2006).

## **CHAPTER 3**

### **Electrochemical deposition of tungsten oxide hydrate films with controlled bandgap energy**

#### **3.1 Introduction**

##### **3.1.2 Materials and issues of existing electrochemical depositions**

Tungsten oxide ( $\text{WO}_3$ ) having “B type” (section 1.2) potential-pH diagram is an n-type semiconductor with a bandgap energy of 3.3 eV, and its hydrates show bandgap energy values changing from 2.55 eV to 3.2 eV depending on the amount of introduced

water molecules.  $\text{WO}_3$  and hydrates have been used as photocatalysts for water splitting and decomposing organic pollutants and components in electrochromic devices[1-7]. The bandgap energy is closely related to the operative wavelength of photocatalyst, and the visible light has been employed for the photocatalytic operation by decreasing bandgap energy[8].  $\text{WO}_3$  and hydrate films have been prepared using several techniques such as gas-phase deposition processes including sputtering and chemical vapor deposition, solution processes including the sol-gel method and hydrothermal synthesis, and electrochemical deposition processes[9-16]. Solution processes have several advantages over gas-phase deposition processes, such as low cost, and high applicability to film preparation on substrates with wide and complicated surface morphology. The cathodic electrochemical deposition of  $\text{WO}_3$  hydrate films for an electrochromic application has been reported by Pauporté et al.[11]. However, there is a possibility of the incorporation of tungsten oxide phases except for the hexavalent  $\text{WO}_3$  according to the potential-pH diagram[17], and deposited  $\text{WO}_3$  was actually reduced and changed the oxidation state of W in  $\text{WO}_3$  because the cathodic electrochemical deposition was potentiostatically performed at  $-0.24$  V vs. NHE which was more negative potential than that for electrochromic reaction of  $\text{WO}_3$ . The introduced phases as mixed valence compounds could have harmful effects on the performance of photoelectronic devices. The anodic electrochemical deposition of  $\text{WO}_3$  hydrate films from metal W plate similar to the alumite treatment was reported[18].  $\text{WO}_3$  prepared by this deposition method kept the valence state of W; however, this method used high voltages, and the surface morphology of films was not easily controllable, leading to very rough and porous morphology. Moreover, both of existing processes such as the cathodic electrochemical deposition and the metal

oxidation could not obtain the crystalline films without any heat-treatment. Crystallinity is important for photovoltaic devices, and well crystalline films are needed.

### 3.1.2 Anodic electrochemical deposition using oxygen-evolution reaction

The direct electrochemical depositions of oxide semiconductor films have been proposed by our group as demonstrated for ZnO, CeO<sub>2</sub>, Ag<sub>2</sub>O and CuO[19,20], and both the Ag<sub>2</sub>O and CuO films are prepared by decreasing the pH value in the vicinity of the substrate by an oxygen gas evolution reaction described as follows



Since the redox potential of the reaction (3.1) locates at approximately 0.2–1.3 V vs. NHE depending on the pH value, it is predicted that films composed of a single WO<sub>3</sub> phase are obtained by anodic electrochemical deposition. As understood from this, anodic electrochemical deposition can be applied to almost oxides having “B type” potential-pH diagram explained in **Chapter 1**.

### 3.1.3 Objective of this study

In this chapter, I aim at developing the novel soft solution process for tungsten oxides having high chemical uniformity and dense crystalline structure to solve the problems of existing processes based on thermodynamic calculation in order to proving usability of anodic electrochemical deposition for oxide semiconductors. The Ag<sub>2</sub>O and Cu<sub>2</sub>O films are prepared by decreasing the pH value in the vicinity of the substrate with an oxygen gas evolution reaction. Since the redox potential of the reaction (3.1) locates at approximately 1.23 V vs. NHE depending on the pH value, there is a possibility to

obtain chemically uniform  $\text{WO}_3$  films by an anodic electrochemical deposition like  $\text{Ag}_2\text{O}$  and  $\text{CuO}$ . Moreover, we speculate that this process solve the problem of existing processes. Here, I report on the preparation of 2.5-eV  $\text{WO}_3 \cdot \text{H}_2\text{O}$  and 3.3-eV  $\text{WO}_3(\text{H}_2\text{O})_{0.33}$  by anodic electrochemical deposition in aqueous solutions containing  $\text{Na}_2\text{WO}_4 \cdot 2\text{H}_2\text{O}$  and  $\text{H}_2\text{SO}_4$ . Structural and optical characterizations were carried out for both  $\text{WO}_3 \cdot \text{H}_2\text{O}$  and  $\text{WO}_3 \cdot (\text{H}_2\text{O})_{0.33}$  films with X-ray diffraction, SEM observation, optical absorption measurements, and electrochemical measurements.

## 3.2 Experimental

### 3.2.1 Theory of electrochemical deposition for tungsten oxide hydrates films

Figure 3.1 shows Potential-pH diagram of W- $\text{H}_2\text{O}$  system at 298 K drawn using equation (1.8) and standard Gibbs free energies according to Table 3.1[21]; concentration of each dissolved species was set at 0.1 mol/L.

Table 3.1 Standard Gibbs free energies of formation at 298.15 K used for drawing of the potential-pH diagram of W- $\text{H}_2\text{O}$  system[21].

Chemical species	$\Delta G_f^0$ [kJ/mol]
$\text{H}_2\text{WO}_4(\text{s})$	-947.652
$\text{WO}_3(\text{s})$	-764.124
$\text{WO}_2(\text{s})$	-533.920
$\text{HWO}_4^-(\text{aq})$	-934.706
$\text{WO}_4^{2-}(\text{aq})$	-914.204
$\text{H}_2\text{O}(\text{l})$	-237.141

A potential-pH diagram maps out possible stable (equilibrium) phases of an aqueous electrochemical system, and it is also called a Pourbaix Diagram about something of metal-water system. Predominant ion boundaries are represented by lines. The relationship between equilibrium constants (K) and standard Gibbs energy of reactions ( $\Delta_r G^0$ ) (2.5), and this equation is used for chemical reactions. Nernst equation (3.2) is used for electrochemical reactions, and equation (2.5) and equation (3.2) fabricate a potential-pH diagram.

$$K = \exp\left(-\frac{\Delta_r G^0}{RT}\right) \quad (2.5)$$

$$E = E^0 - \frac{RT \ln K}{zF} \quad (3.2)$$

Nernst equation (3.2) is led from equation (1.10) and (1.14). In dilute solution, activities are approximated to ion concentrations and ion concentrations are utilized as activities for construction of potential-pH diagram for W-H<sub>2</sub>O system. Here, two lines relate to oxidation-reduction reaction of water are drawn as follows.

Hydrogen generation:



$$E = 0 - 0.0592 \text{ pH (V vs. NHE)} \quad (3.4)$$

Oxygen generation:



$$E = 1.23 - 0.0592 \text{ pH (V vs. NHE)} \quad (3.6)$$

The potential range of 1.23 V between these lines is called the potential window of water, and decomposition-reaction of water does not happen in this region.

First, the boundary of the acid-base reaction is determined as follows;



$\Delta_r G^0$  can be calculated by taking standard Gibbs energies of formation,  $\Delta_f G^0$ .

$$\begin{aligned} \Delta_r G^0 &= \Delta_f G^0_{[\text{WO}_3]} + \Delta_f G^0_{[\text{H}_2\text{O}]} - (\Delta_f G^0_{[\text{WO}_4^{2-}]} + 2\Delta_f G^0_{[\text{H}^+]}) \\ &= (-764.124) + (-237.141) - (-914.204 + 2 \times 0) \\ &= -87.061 \text{ (kJ/mol)} \end{aligned} \quad (3.8)$$

Then, substitution of  $\ln K = 2.303 \log K$ ,  $\Delta_r G^0 = -87.061 \text{ kJmol}^{-1}$ ,  $R = 8.314 \text{ JK}^{-1}\text{mol}^{-1}$  and  $T = 298.15 \text{ K}$  into (2.5) gives  $\log K$  as below.

$$\log K = - \frac{-87.061 \times 10^3}{2.303 \times 8.314 \times 298} = 15.258 \quad (3.9)$$

Meanwhile,  $K$  can be expressed by a product of equilibrium activities of the species relevant to the chemical reaction, and considering the activity of solids and solvents are 1, the following equation holds.

$$K = \frac{a_{\text{WO}_3} a_{\text{H}_2\text{O}}}{a_{\text{WO}_4^{2-}} a_{\text{H}^+}^2} \cong \frac{1}{a_{\text{WO}_4^{2-}} a_{\text{H}^+}^2} \quad (3.10)$$

Activities are nearly equal to ion concentrations in dilute solution, and  $a_{\text{WO}_4^{2-}}$  and  $a_{\text{H}^+}$  are approximated as  $[\text{WO}_4^{2-}]$  and  $[\text{H}^+]$ , respectively, and the  $\log[\text{H}^+]$  is  $-\text{pH}$ ; then, taking the logarithm of equation (3.10) gives.

$$\log K = - \log[\text{WO}_4^{2-}] + 2\text{pH} \quad (3.11)$$

$$\text{pH} = 0.5 \log K + 0.5 \log[\text{WO}_4^{2-}] \quad (3.11)'$$

When, equation (3.10) is substituted into equation(3.11)', it turns to equation (3.12).

$$\text{pH} = 7.629 + 0.5 \log[\text{WO}_4^{2-}] \quad (3.12)$$

The equation (3.12) is a function of only ion concentration, and the boundary pH is decided from the given value of ion concentration.

Next, calculation for the line of boundary of electrochemical equilibrium as reaction(3.13) is able to be conducted by considering the electrochemical equilibrium for the following reaction.



$\Delta_r G^0$  of this reaction can be calculated as below.

$$\begin{aligned} \Delta_r G^0 &= \Delta_r G^0_{[\text{WO}_2]} + 2\Delta_r G^0_{[\text{H}_2\text{O}]} - (\Delta_r G^0_{[\text{WO}_4^{2-}]} + 4\Delta_r G^0_{[\text{H}^+]} + 2\Delta_r G^0_{[\text{e}^-]}) \\ \Delta_r G^0 &= (-533.920) + 2 \times (-237.141) - [(-914.204) + 0 + 0] \\ &= -93.998 \text{ kJ mol}^{-1} \end{aligned} \quad (3.14)$$

Here, the standard electrode potential ( $E^0$ ) can be deduced from  $\Delta_r G^0$  as follows.

$$E^0 = -\frac{\Delta_r G^0}{nF} = -\frac{-93998}{2 \times 96485} = 0.4871 \text{ V vs. NHE} \quad (3.15)$$

Here, Nernst equation for this reaction is expressed as follows.

$$E = E^0 - \frac{0.0592}{2} \log K = E^0 - \frac{0.0592}{2} \log \frac{a_{\text{WO}_2} a_{\text{H}_2\text{O}}^2}{a_{\text{WO}_4^{2-}}^2 a_{\text{H}^+}^4} \quad (3.16)$$

Substituting equation (3.15) into equation(2.5),

$$E = -0.4871 - \frac{0.0592}{2} (\log a_{\text{WO}_2} + 2 \log a_{\text{H}_2\text{O}} - \log a_{\text{WO}_4^{2-}} - 4 \log a_{\text{H}^+}) \quad (3.17)$$

Then, considering the activities of solids and solvents are 1, and activities are approximated as their concentrations, the following equation (3.18) holds.

$$E = -0.4871 + 0.0296 \log[\text{WO}_4^{2-}] - 0.1184 \text{ pH V vs. NHE} \quad (3.18)$$

As shown in equation (3.18), the electrochemical equilibrium state of the reaction is indicated by a function of ion concentration, pH value, and cell potential, and once  $[\text{WO}_4^{2-}]$  is determined, the equation (3.18) makes a line on the potential-pH diagram. The calculations of equilibrium for all possible combinations of chemical species in aqueous solution for W-H<sub>2</sub>O system were carried out with the same way, and they are summarized in table 3.2. By choosing the boundaries in order to fulfill all of these relationships rationally, the potential-pH diagram is parceled out into some regions where each species has the lowest Gibbs energy, thereby being the most stable species in each region.

The theory of anodic electrochemical deposition for tungsten oxide is explained using potential-pH diagram of Figure 3.1 and the equations are shown as follows:[22]



Table 3.2 Reaction formula and the equilibrium formula for pH-diagram.

Reaction formula	$\Delta_f G^0$ (kJmol <sup>-1</sup> )	Equilibrium formula for pH-diagram
$\text{WO}_4^{2-} + \text{H}^+ \rightleftharpoons \text{HWO}_4^-$	-20.502	pH = 3.593
$\text{WO}_4^{2-} + 2\text{H}^+ \rightleftharpoons \text{H}_2\text{WO}_4$	-33.448	pH = 2.931 + 0.5 log[ $\text{WO}_4^{2-}$ ]
$\text{WO}_4^{2-} + 2\text{H}^+ \rightleftharpoons \text{WO}_3 + \text{H}_2\text{O}$	-87.061	pH = 7.629 + 0.5 log[ $\text{WO}_4^{2-}$ ]
$\text{WO}_4^{2-} + 4\text{H}^+ + 2\text{e}^- \rightleftharpoons \text{WO}_2 + 2\text{H}_2\text{O}$	-93.998	$E = -0.4871 + 0.0296 \log[\text{WO}_4^{2-}] - 0.1184\text{pH V vs. NHE}$
$\text{WO}_4^{2-} + 8\text{H}^+ + 6\text{e}^- \rightleftharpoons \text{W} + 4\text{H}_2\text{O}$	-34.36	$E = 0.0594 + 0.00987 \log[\text{WO}_4^{2-}] - 0.07893\text{pH V vs. NHE}$
$\text{HWO}_4^- + \text{H}^+ \rightleftharpoons \text{H}_2\text{WO}_4$	-12.946	pH = 2.269 + log[ $\text{HWO}_4^-$ ]
$\text{HWO}_4^- + \text{H}^+ \rightleftharpoons \text{WO}_3 + \text{H}_2\text{O}$	-66.559	pH = 11.665 + log[ $\text{HWO}_4^-$ ]
$\text{HWO}_4^- + 3\text{H}^+ + 2\text{e}^- \rightleftharpoons \text{WO}_2 + 2\text{H}_2\text{O}$	-73.496	$E = 0.3809 + 0.0296 \log[\text{HWO}_4^-] - 0.888\text{pH V vs. NHE}$
$\text{HWO}_4^- + 7\text{H}^+ + 6\text{e}^- \rightleftharpoons \text{W} + 4\text{H}_2\text{O}$	-13.858	$E = 0.02394 + 0.00987 \log[\text{HWO}_4^-] - 0.0691\text{pH V vs. NHE}$
$\text{H}_2\text{WO}_4 + 2\text{H}^+ + 2\text{e}^- \rightleftharpoons \text{WO}_2 + 2\text{H}_2\text{O}$	-6.937	$E = 0.03595 - 0.0592\text{pH V vs. NHE}$
$\text{H}_2\text{WO}_4 + 6\text{H}^+ + 6\text{e}^- \rightleftharpoons \text{W} + 4\text{H}_2\text{O}$	-0.912	$E = 0.001575 - 0.0592\text{pH V vs. NHE}$
$\text{WO}_3 + 2\text{H}^+ + 2\text{e}^- \rightleftharpoons \text{WO}_2 + \text{H}_2\text{O}$	-6.937	$E = 0.03595 - 0.0592\text{pH V vs. NHE}$
$\text{WO}_3 + 6\text{H}^+ + 6\text{e}^- \rightleftharpoons \text{W} + 3\text{H}_2\text{O}$	52.701	$E = -0.0910 - 0.0592\text{pH V vs. NHE}$
$\text{WO}_2 + 4\text{H}^+ + 4\text{e}^- \rightleftharpoons \text{W} + 2\text{H}_2\text{O}$	59.683	$E = -0.1545 - 0.0592\text{pH V vs. NHE}$

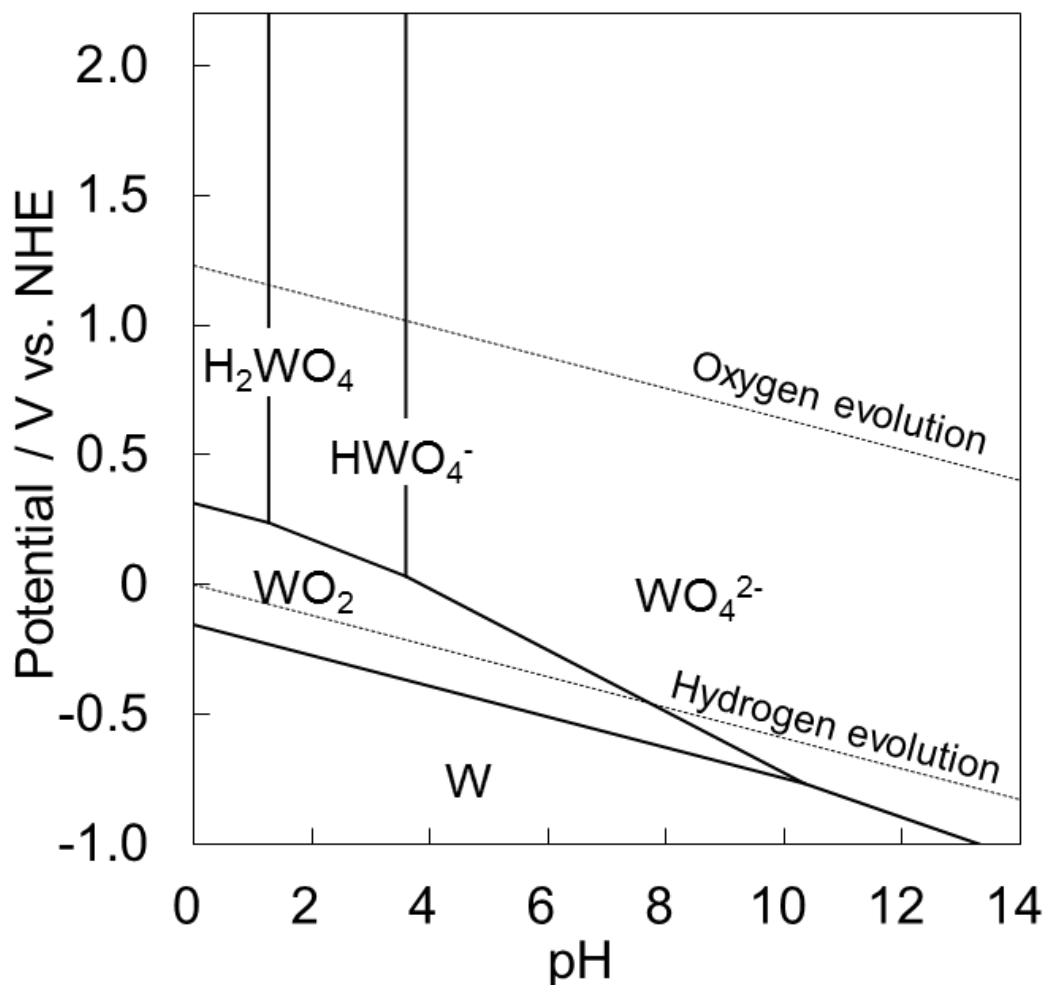


Fig. 3.1 Potential-pH diagram of W-H<sub>2</sub>O system at 348 K. Concentration of each dissolved species was set as 0.1 mol/L.

Sodium tungstate(VI) dihydrate (Na<sub>2</sub>WO<sub>4</sub>·2H<sub>2</sub>O) decomposes into Na<sup>+</sup> and WO<sub>4</sub><sup>2-</sup> in the solution (equation (3.19)), and decreasing the pH value in the vicinity of the substrate with an oxygen-generation reaction is caused by applying more positive potential than that of oxygen-generation reaction on the substrate (equation (3.1)). WO<sub>4</sub><sup>2-</sup> ions are combined with protons because of the decrease of pH, and WO<sub>3</sub>·H<sub>2</sub>O is

formed on the substrate. It is well known that  $\text{WO}_3$  forms its hydrate easily in aqueous solutions[23], and valence state of W in all  $\text{WO}_3 \cdot \text{H}_2\text{O}$  were stabilized at +6. This process promises to give tungsten oxide and its hydrates structures with high chemical uniformity.

### **3.2.2 Experimental procedure for electrochemical deposition of tungsten oxide hydrates films**

The solution for electrochemical deposition was prepared using 0.01, 0.03, 0.05, 0.09, 0.1 and 0.5 mol/L  $\text{Na}_2\text{WO}_4 \cdot 2\text{H}_2\text{O}$  and deionized water (15 M $\Omega$ cm with Milli-pore), and the solution pH was adjusted to 1.0 by sulfuric acid (KANTO CHEMICAL, 96%). Electrochemical deposition was performed using a typical three-electrode electrochemical cell equipped with a fluorine-doped tin oxide glass (10  $\Omega/\square$  FTO), a platinum foil, and an Ag/AgCl electrode (0.199 V vs. NHE) as the working, counter, and reference electrodes, respectively. Prior to the electrochemical deposition, the FTO substrate was rinsed with acetone, and then the deposition area was limited to 15 mm  $\times$  15 mm by waterproof adhesive tape (Fluoroplastic Saturated Glass Cloth Tape NITOFロン No. 973UL-S/973UL, Nitto). Then, the substrate was degreased by cathodic polarization at 10 mA  $\text{cm}^{-2}$  for 3 min in a 1.0 mol/L sodium hydroxide aqueous solution. Deposition potential was decided by linear sweep voltammetry with 0.01 and 0.5 mol/L  $\text{Na}_2\text{WO}_4 \cdot 2\text{H}_2\text{O}$  solution at 1.0 of pH, and the scan rate was 5 mV/s. Deposition parameters were set at the potential of 2.0 V vs. Ag/AgCl, the temperature of 70°C, and the deposition time of 2 hours with a computer-controlled electrochemical measurement system (HSV-110, HOKUTO DENKO).

### 3.2.3 Characterization of tungsten oxide hydrates films.

The electron spectra were recorded by an X-ray photoelectron spectroscope (XPS: PHI Quantera SXM-CI, ULVAC-PHI, Inc., monochromatized Al K $\alpha$  radiation). The pre-sputtering using Ar<sup>+</sup> ions accelerated at 1.0 kV was carried out in an area of 2.0 $\times$ 2.0  $\mu\text{m}^2$  on the surface of films for 18 seconds before the measurement. The binding energy was corrected by the C1s peak at 284.6 eV. The relative sensitivity factors of 0.733 and 3.863 for O1s and W4f orbitals were used for the calculation of molar ratios of W and O elements. The structures of the deposited films were identified by an X-ray diffraction (XRD: RINT2500, Rigaku) technique with monochromatized Cu K $\alpha$  radiation set at 40 kV and 200 mA. A field emission scanning electron microscope (FE-SEM) was used for observing the surface and the cross-sectional structures with an accelerating voltage of 3.0 kV. Optical absorption spectra were recorded by a spectrophotometer (UV-Vis-NIR: U4100, HITACHI Hightech) with the reference of bare FTO substrate. Photoelectrochemical measurements were carried out in a 1.0 mol/L Na<sub>2</sub>SO<sub>4</sub> solution with a three-electrode electrochemical cell with a platinum foil counter and an Ag/AgCl reference electrode. Applied potential was set to 1.2 V (vs. Ag/AgCl), which was decided based on the results of preliminary experiments of the linear sweep voltammetry.

Intermittent light irradiation was performed for 120 s with a high-pressure mercury lamp (USHIO Optical Modulex, SX-UI250HQ, 500 W), with switching “ON” and “OFF” carried out every 10 seconds. A bare FTO substrate was used as the filter to eliminate the ultraviolet light at photon energy over the bandgap energy of 3.3 eV.

### 3.3 Results and Discussion

#### 3.3.1. Composition and structure of tungsten oxide hydrates films

Figure 3.2 shows linear sweep voltamograms for the 0.01, and 0.5 mol/L  $\text{Na}_2\text{WO}_4 \cdot 2\text{H}_2\text{O}$  solution at pH of 1.0. A rising edges of current for oxygen-generation reaction were observed at approximately +1.9 V vs. Ag/AgCl in both the 0.01, and 0.5 mol/L solutions, and deposition potential was set at the +2.0 V vs. Ag/AgCl.

Figure 3.3 shows the chronoamperometric curves in the 0.01, 0.03, 0.05, 0.09, 0.1, and 0.5 mol/L  $\text{WO}_4^{2-}$  solutions and the dependence of the current density at 120 min on the  $\text{WO}_4^{2-}$  concentration. The films deposited on the substrate without any peeling off even after the electrochemical deposition for 120 min, irrespective of the  $\text{WO}_4^{2-}$  concentration. The current density drastically decreased at the initial stage (inset of Figure 3.3(A)) and then gradually decreased to an almost constant value for the 0.01, 0.03, 0.05, 0.09, and 0.1 mol/L  $\text{WO}_4^{2-}$  solutions.

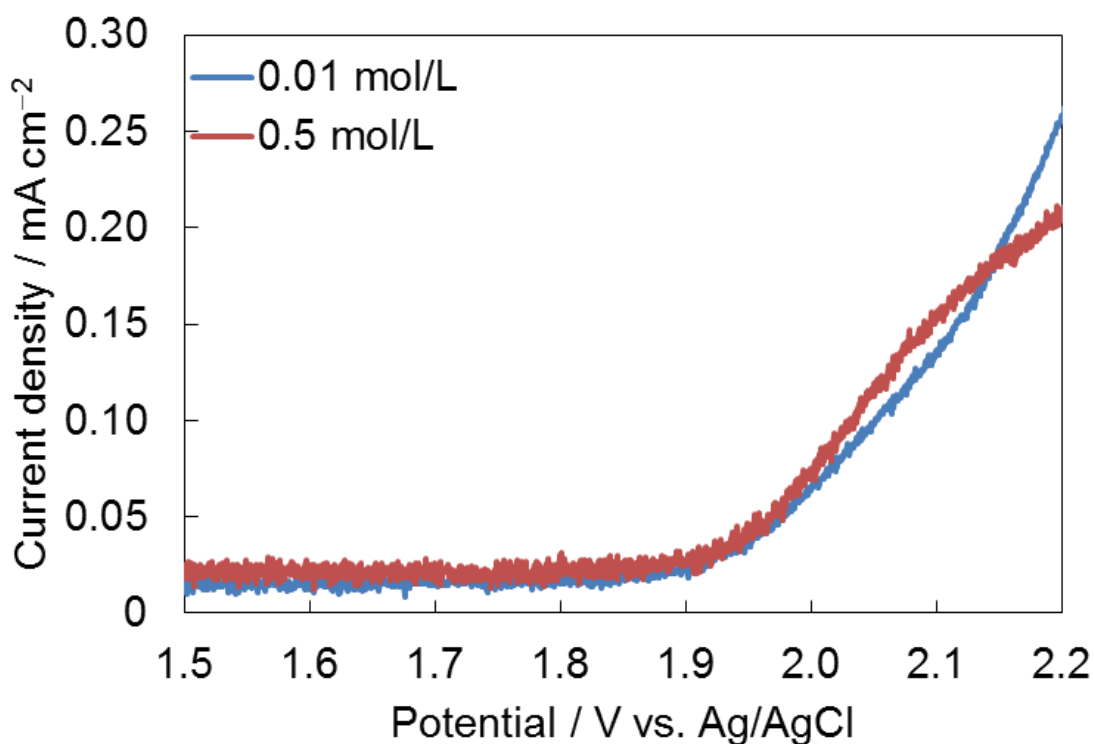


Fig. 3.2 Linear sweep voltammograms for the 0.01, and 0.5 mol/L  $\text{Na}_2\text{WO}_4 \cdot 2\text{H}_2\text{O}$  solution at pH of 1.0; scan rate was 5 mV/s.

The current density in the 0.5 mol/L  $\text{WO}_4^{2-}$  solution decreased up to about 65 min and then slightly increased with the passage of time to 120 min. The current density at the deposition time of 120 min was around  $0.025 \text{ mA cm}^{-2}$  for the 0.01, 0.03, 0.05 and 0.1 mol/L  $\text{WO}_4^{2-}$  solutions, and 0.5 mol/L  $\text{WO}_4^{2-}$  solutions showed the value of  $0.043 \text{ mA cm}^{-2}$ , suggesting that the deposited film changed depending on the  $\text{WO}_4^{2-}$  concentration. The films deposited at 0.01, 0.03, 0.05, and 0.09 mol/L  $\text{WO}_4^{2-}$  solutions had a yellowish appearance, but transparent films without any color were obtained at 0.1 and 0.5 M  $\text{WO}_4^{2-}$  concentrations.

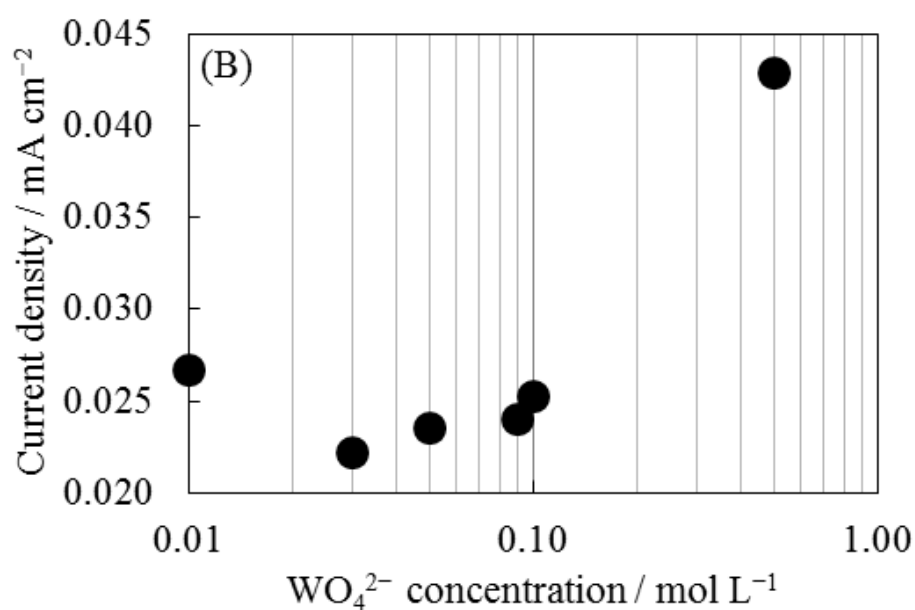
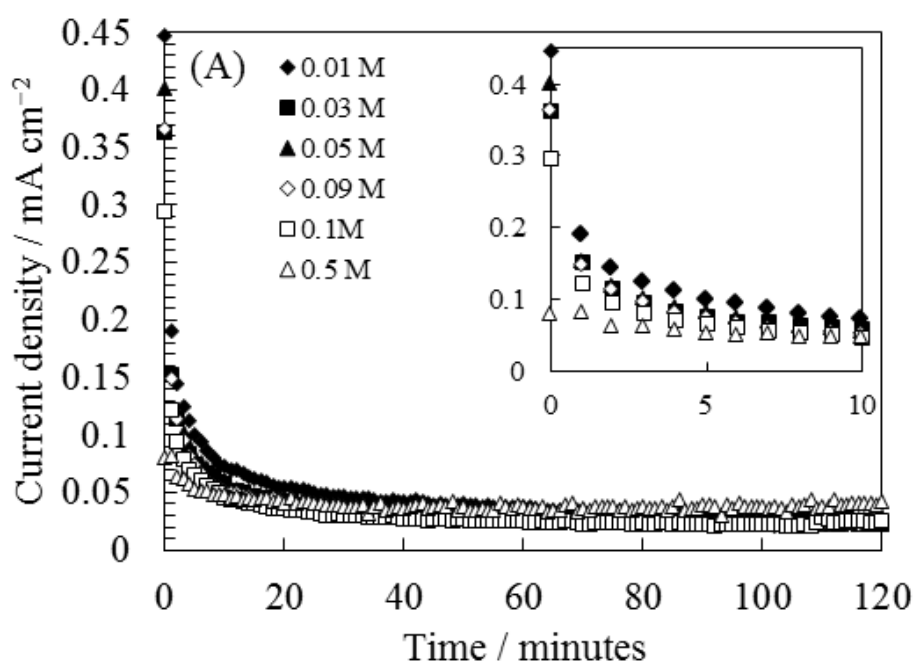


Fig. 3.3 Change in current density for electrochemical deposition with the deposition time in 0.01, 0.03, 0.05, 0.09, 0.1, and 0.5 mol/L WO<sub>4</sub><sup>2-</sup> solutions and inset of its magnified plot in initial stage of electrochemical deposition(A). The correlation between current density at 120 minutes and the WO<sub>4</sub><sup>2-</sup> concentration(B).

Figure 3.4 shows survey electron spectra and W4f and O1s electron spectra for films prepared in 0.03 and 0.1 mol/L  $\text{WO}_4^{2-}$  solutions. Both the yellowish and transparent films deposited in the 0.03 and 0.1 mol/L  $\text{WO}_4^{2-}$  solutions show almost the same in peak energy, and all the peaks on the survey spectra are able to be identified as peaks originating from the W and O elements. Peaks at 35.7, 37.7, 247.9, 260.5, 427.9, and 495.8 eV are identified with W4f<sub>7/2</sub>, W4f<sub>5/2</sub>, W4d<sub>5/2</sub>, W4d<sub>3/2</sub>, W4p<sub>3/2</sub>, and W4p<sub>1/2</sub> for W<sup>6+</sup> element, and peaks at 530.5 and 974.7 eV are assigned to O1s and O<sub>KLL</sub> electron spectra[24,25]. Any peaks originating from other elements were not detected on the spectra. This means that both the yellowish and transparent films prepared in 0.03 and 0.1 mol/L  $\text{WO}_4^{2-}$  solutions were composed of only W and O elements. The W4f<sub>7/2</sub> peaks for films prepared in 0.03 and 0.01 mol/L  $\text{WO}_4^{2-}$  solutions showed a constant binding energy of 35.7 eV and were close to 35.6 eV of W<sup>6+</sup> state in  $\text{WO}_3$  and smaller than 36.2 eV of W<sup>6+</sup> state in  $\text{H}_2\text{WO}_4$ [26]. Additionally, the molar ratios of the O to W elements (O/W ratio) calculated from integrated intensities of peaks with relative sensitivity factors are 3.5 and 3.4 from the 0.03 and 0.1 mol/L  $\text{WO}_4^{2-}$  solutions, respectively. Both the O1s spectra for films prepared in the 0.03 and 0.1 mol/L solutions showed a peak at 530.6-530.7 eV and a shoulder at 532.3 eV. The binding energy of 530.6-530.7 eV is close to that in the state of O<sup>2-</sup> in  $\text{WO}_3$ [27]. The peak at 532.3 eV was reported to be identified as O<sup>2-</sup> in  $\text{H}_2\text{O}$  incorporated in  $\text{WO}_3 \cdot (\text{H}_2\text{O})_x$ [28,29], and the value was smaller than 533.2 eV of  $\text{H}_2\text{O}$ [27]. Those peaks on the O1s spectra reflect the existence of two states of O, O<sup>2-</sup> in  $\text{H}_2\text{O}$  of  $\text{WO}_3 \cdot (\text{H}_2\text{O})_x$ , and O<sup>2-</sup> in  $\text{WO}_3$  of  $\text{WO}_3 \cdot (\text{H}_2\text{O})_x$ . The intensity ratios of the shoulder to the peak are estimated to be 0.13 and 0.1 for the films prepared in the 0.03 and 0.1 mol/L  $\text{WO}_4^{2-}$  solutions, respectively.

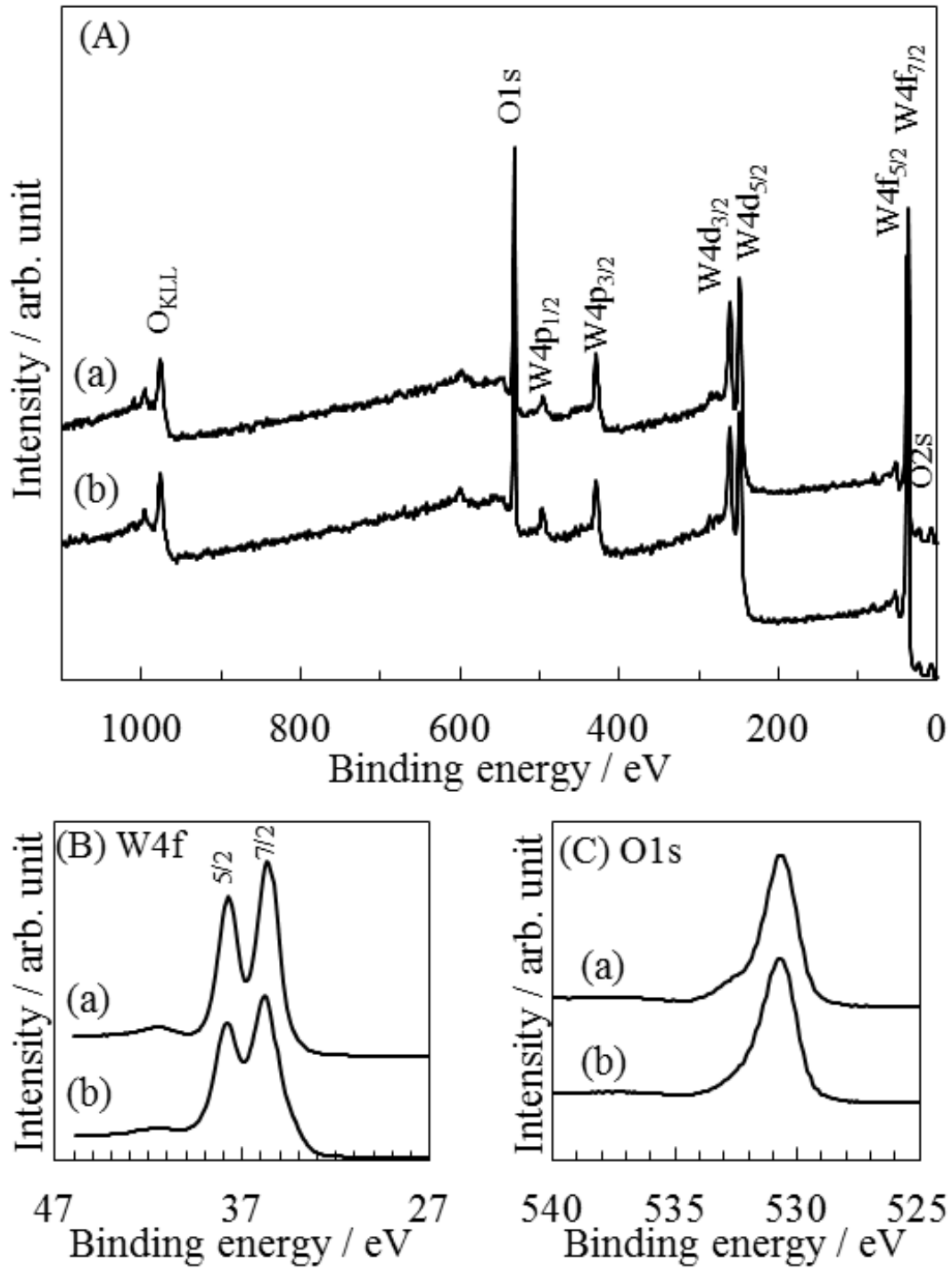


Fig. 3.4 Survey(A), O1s(B), and W4f electron spectra(C) for W-O-H films prepared in the 0.03(a), and 0.1 mol/L (b)  $\text{WO}_4^{2-}$  solutions.

According to W in films prepared in 0.03 and 0.1 mol/L  $\text{WO}_4^{2-}$  solutions having the same valence state, difference of two films in the molarities only relate to amount of hydration water molecules in films. The change in the O/W ratio and peak/shoulder intensity ratio suggests a change in the  $\text{H}_2\text{O}$  content of the films, and these films will be abbreviated as W-O-H films hereafter. The W-O-H films possessed  $\text{W}^{6+}$  state in  $\text{WO}_3$  and the  $\text{H}_2\text{O}$  content was different depending on the  $\text{WO}_4^{2-}$  concentration.

Figure 3.5 shows the XRD patterns of W-O-H films prepared in 0.01–0.5 mol/L  $\text{WO}_4^{2-}$  solutions and the correlation of lattice constant calculated from X-ray diffraction to the  $\text{WO}_4^{2-}$  concentration. The diffracted X-ray peaks for W-O-H films prepared in the 0.01–0.09 mol/L  $\text{WO}_4^{2-}$  solutions show peak angles at 16.5, 25.6, 33.4, 34.2, 35.0, and 38.9°, which are assigned to the (020), (111), (040), (200), (002), and (022) planes of  $\text{WO}_3 \cdot \text{H}_2\text{O}$  with an orthorhombic lattice, respectively[30]. The X-ray diffracted peaks for W-O-H films prepared in the 0.01–0.5 mol/L  $\text{WO}_4^{2-}$  solutions are observed at 22.8, 24.0, 26.5, 28.1, and 36.6°, and are assigned to (002), (200), (022), (220), and (222) plane of  $\text{WO}_3 \cdot (\text{H}_2\text{O})_{0.33}$  with an orthorhombic lattice, respectively [26]. The W-O-H films prepared in the 0.01 M  $\text{WO}_4^{2-}$ , 0.03 - 0.09 M  $\text{WO}_4^{2-}$ , and 0.1–0.5 mol/L  $\text{WO}_4^{2-}$  solutions are identified as single  $\text{WO}_3 \cdot \text{H}_2\text{O}$ , mixtures of  $\text{WO}_3 \cdot \text{H}_2\text{O}$  and  $\text{WO}_3 \cdot (\text{H}_2\text{O})_{0.33}$ , and single  $\text{WO}_3 \cdot (\text{H}_2\text{O})_{0.33}$ , respectively[31]. Excellent crystalline tungsten oxides prepared by electrochemical deposition without any heat-treatment have never been reported, and it is a novel and advantageous factor of this method. The lattice constants are calculated from the (002), (020), and (200) planes of  $\text{WO}_3 \cdot \text{H}_2\text{O}$  and  $\text{WO}_3 \cdot (\text{H}_2\text{O})_{0.33}$ , but a calculation could not be performed for  $\text{WO}_3 \cdot (\text{H}_2\text{O})_{0.33}$  in the W-O-H films prepared in 0.03 and 0.05 mol/L  $\text{WO}_4^{2-}$  solutions, because of the absence of (002) and (200) diffracted peaks.

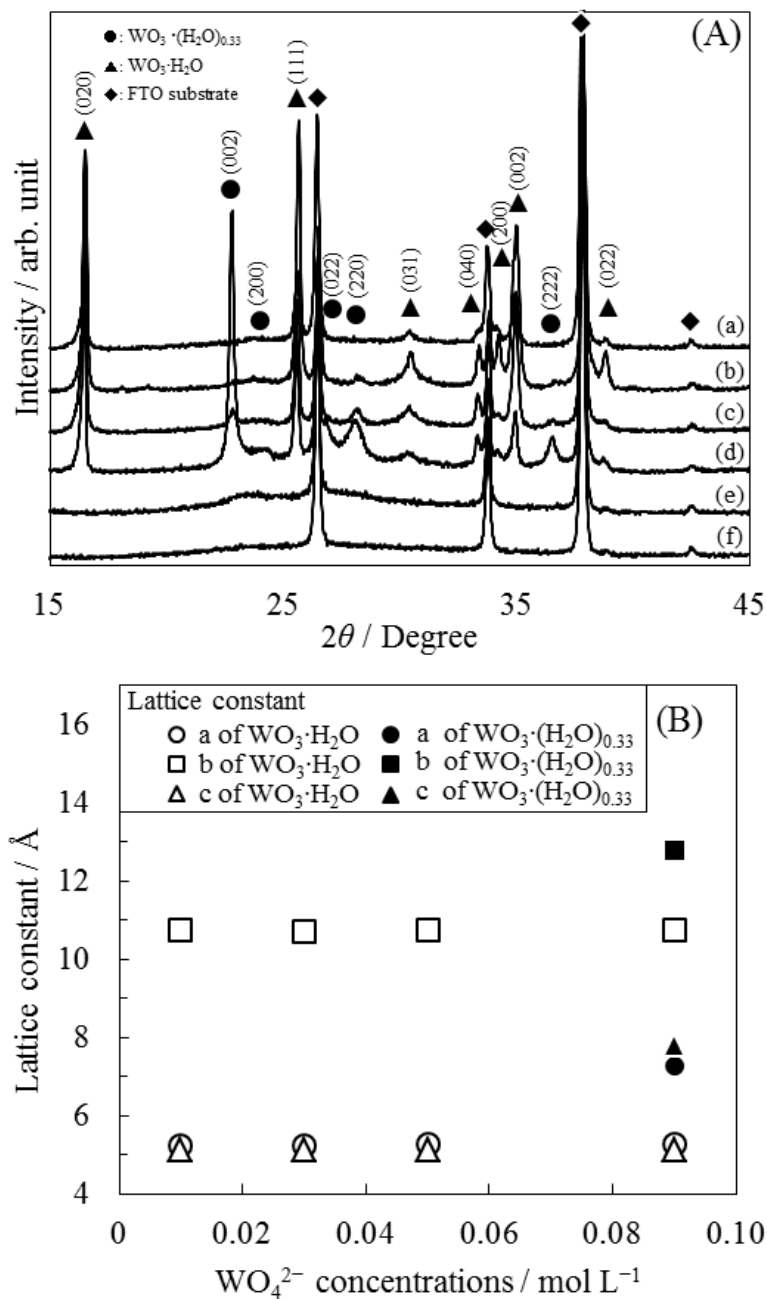


Fig. 3.5 X-ray diffraction pattern of W-O-H films prepared in the 0.01(a), 0.03(b), 0.05(c), 0.09(d), 0.1(e), and 0.5 mol/L(f)  $\text{WO}_4^{2-}$  solutions(A), and the correlation between the lattice constant calculated from X-ray diffraction and  $\text{WO}_4^{2-}$  concentration(B).

In addition, the lattice constants of  $\text{WO}_3 \cdot (\text{H}_2\text{O})_{0.33}$  could not be calculated for the 0.1 and 0.5 mol/L  $\text{WO}_4^{2-}$  solutions, because of the broadened and weak diffracted X-ray

peaks at approximately 23 and 27 degrees in  $2\theta$ . The lattice constants of a, b, and c of  $\text{WO}_3 \cdot \text{H}_2\text{O}$  are almost constant values of 5.256 Å, 10.74 Å, and 5.127 Å, irrespective of the  $\text{WO}_4^{2-}$  concentration, and the volume of the unit cell was calculated to be 289.4 Å<sup>3</sup>, which was larger by approximately 0.3% than the standard value. Meanwhile, the lattice constants of a, b, and c of  $\text{WO}_3 \cdot (\text{H}_2\text{O})_{0.33}$  were calculated to be 7.294 Å, 12.795 Å, and 7.792 Å, and the unit cell volume was calculated to be 727.2 Å<sup>3</sup>, and was larger by approximately 2.6% than the standard value. The unit cell of both the  $\text{WO}_3 \cdot \text{H}_2\text{O}$  and  $\text{WO}_3 \cdot (\text{H}_2\text{O})_{0.33}$  slightly expanded, but the effect of the  $\text{WO}_4^{2-}$  concentration in the dimension could not be seen. The intensity of the diffracted X-ray peaks assigned to  $\text{WO}_3 \cdot \text{H}_2\text{O}$  is dependent on the  $\text{WO}_4^{2-}$  concentration. Both the (020) and (002) peaks increase with increasing  $\text{WO}_4^{2-}$  concentration up to 0.05 mol/L, and then decrease. Both the intensity of the (020) and (002) peaks assigned to  $\text{WO}_3 \cdot \text{H}_2\text{O}$  increased with increasing  $\text{WO}_4^{2-}$  concentration up to 0.05 mol/L, and then decreased. The (002) plane is normal to the (020) plane in the orthorhombic lattice, and this suggests that the orientation is almost random.

Figure 3.6 shows SEM images of the surfaces of W-O-H films prepared in the 0.01–0.5 mol/L  $\text{WO}_4^{2-}$  solutions. From the SEM image of the W-O-H film prepared in the 0.01 mol/L  $\text{WO}_4^{2-}$  solution, sparse square grains of approximately 1 μm in size can be observed, and the bare FTO surface is partly exposed. The square grains are identified as  $\text{WO}_3 \cdot \text{H}_2\text{O}$  by XRD analysis. The square  $\text{WO}_3 \cdot \text{H}_2\text{O}$  grains are also observed for W-O-H films prepared in the 0.03–0.09 mol/L  $\text{WO}_4^{2-}$  solutions, and the size increases to approximately 2 μm with an increase in the  $\text{WO}_4^{2-}$  concentration to 0.09 mol/L.

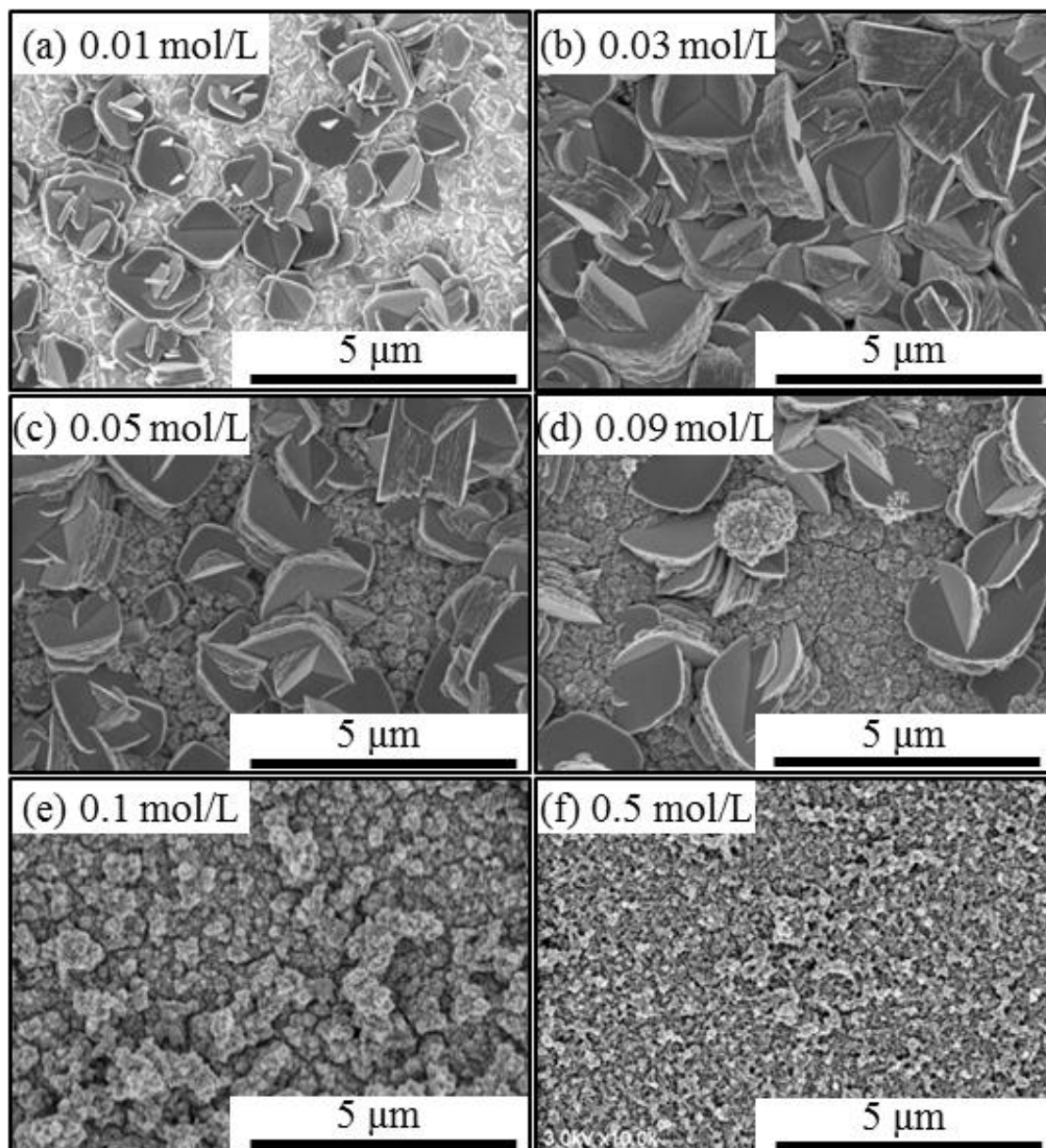


Fig. 3.6 SEM images of the surfaces of W-O-H films prepared in the 0.01(a), 0.03(b), 0.05(c), 0.09(d), 0.1(e), and 0.5 mol/L(f)  $\text{WO}_4^{2-}$  solutions.

The aggregates of granular grains with a size of approximately 100 nm can be observed between the  $\text{WO}_3 \cdot \text{H}_2\text{O}$  square grains and covered the entire FTO substrate surface. The square  $\text{WO}_3 \cdot \text{H}_2\text{O}$  grains disappeared for W-O-H films prepared in the 0.1 and 0.5

$\text{WO}_4^{2-}$  solutions, and only granular grains deposited on the FTO substrate, which were identified as  $\text{WO}_3 \cdot (\text{H}_2\text{O})_{0.33}$  with X-ray diffraction.

Figure 3.7 shows the cross-sectional SEM images of W-O-H films prepared in the 0.01–0.5 mol/L  $\text{WO}_4^{2-}$  solutions. The W-O-H film prepared in 0.01 mol/L  $\text{WO}_4^{2-}$  solution is composed of  $\text{WO}_3 \cdot \text{H}_2\text{O}$  square grains with a height of approximately 1  $\mu\text{m}$  corresponding to the size of the grains, and the height of square  $\text{WO}_3 \cdot \text{H}_2\text{O}$  grains increased to 1.8  $\mu\text{m}$  at 0.03 mol/L  $\text{WO}_4^{2-}$  concentration. From the cross-sectional SEM images, the  $\text{WO}_3 \cdot (\text{H}_2\text{O})_{0.33}$  grains cannot be clearly observed at the 0.03 mol/L  $\text{WO}_4^{2-}$  concentration due to the thin thickness, and the thicknesses of these prepared at the  $\text{WO}_4^{2-}$  concentration of 0.05 mol/L and 0.09 mol/L were estimated to be 0.25  $\mu\text{m}$  and 0.75  $\mu\text{m}$ , respectively. Large  $\text{WO}_3 \cdot \text{H}_2\text{O}$  square grains stacked on the lower granular  $\text{WO}_3 \cdot (\text{H}_2\text{O})_{0.33}$  covered the entire FTO substrate, although the deposition mechanism is not clear at present. Approximately 1.8  $\mu\text{m}$ -thick  $\text{WO}_3 \cdot (\text{H}_2\text{O})_{0.33}$  with a large surface irregularity deposited on the FTO substrate at the 0.1 mol/L  $\text{WO}_4^{2-}$  concentration. The thickness of the granular film of  $\text{WO}_3 \cdot (\text{H}_2\text{O})_{0.33}$  grains decreased to 200 nm at a 0.5 mol/L  $\text{WO}_4^{2-}$  concentration. Depending on  $\text{WO}_4^{2-}$  concentration in the solution, island-like  $\text{WO}_3 \cdot \text{H}_2\text{O}$  was obtained in the 0.01 mol/L  $\text{WO}_4^{2-}$  solutions, dense excellent crystalline  $\text{WO}_3 \cdot \text{H}_2\text{O}$  and  $\text{WO}_3 \cdot (\text{H}_2\text{O})_{0.33}$  films were obtained in the 0.03–0.09 mol/L  $\text{WO}_4^{2-}$  solutions, and porous fine crystalline  $\text{WO}_3 \cdot (\text{H}_2\text{O})_{0.33}$  films were obtained in the 0.1–0.5 mol/L  $\text{WO}_4^{2-}$  solutions.

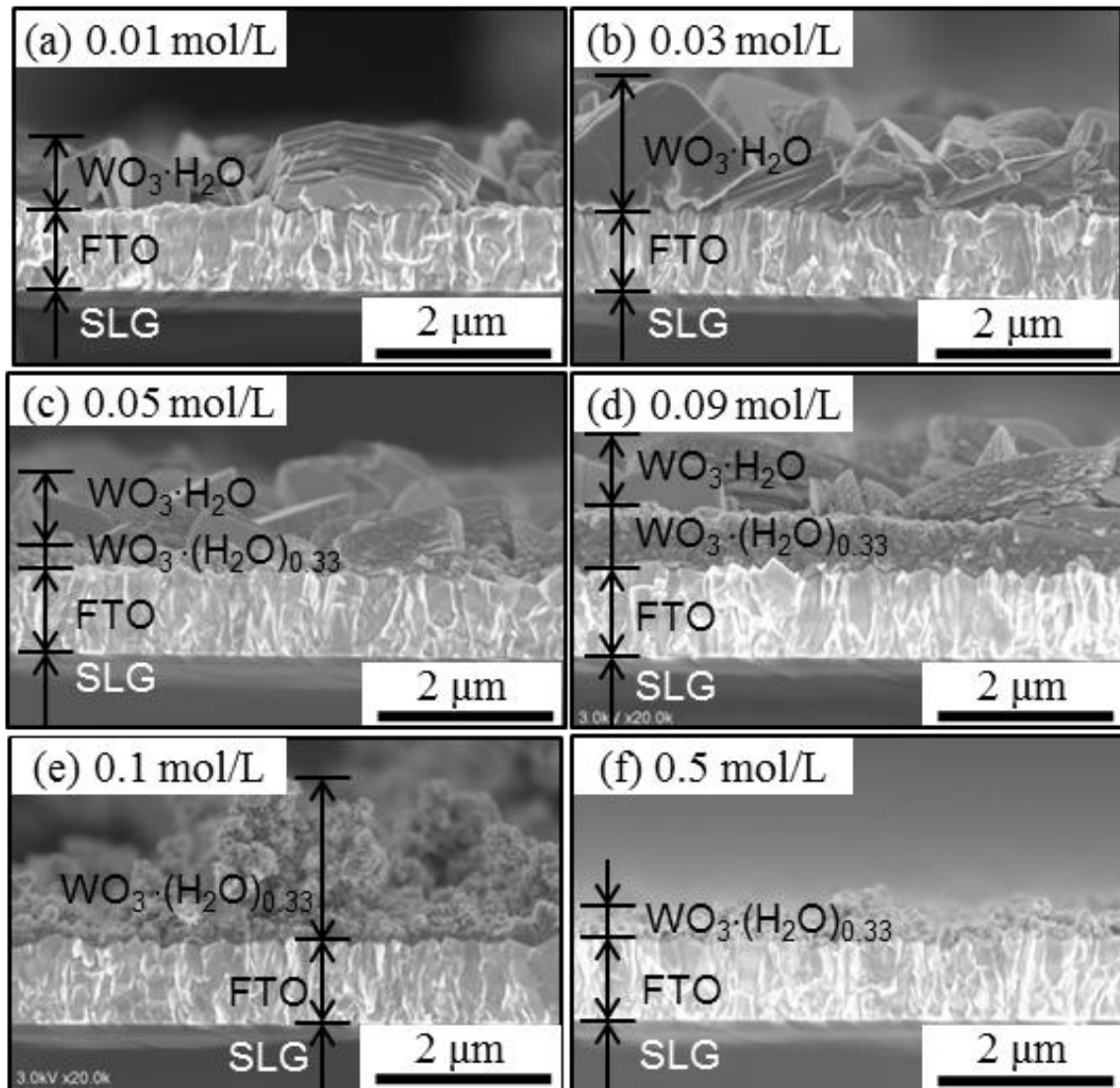


Fig. 3.7 Cross-Sectional SEM images of W-O-H films prepared in the 0.01(a), 0.03(b), 0.05(c), 0.09(d), 0.1(e), and 0.5 mol/L(f)  $\text{WO}_4^{2-}$  solutions.

### 3.3.2 Optical properties of $\text{WO}_3\cdot\text{H}_2\text{O}$ and $\text{WO}_3\cdot(\text{H}_2\text{O})_{0.33}$ films.

Figure 3.8 shows the absorption spectra for the W-O-H films prepared in the 0.01-0.5 mol/L  $\text{WO}_4^{2-}$  concentration and the correlation between bandgap energy and  $\text{WO}_4^{2-}$  concentration. The absorption spectra of the W-O-H films prepared in 0.01, 0.03, 0.05, and 0.09 mol/L  $\text{WO}_4^{2-}$  solutions showed absorption edge at around 500 nm, while additional absorption edge at around 400 nm are observed for W-O-H films prepared in 0.05, 0.09, 0.1, and 0.5 mol/L  $\text{WO}_4^{2-}$  solutions. The absorption coefficient ( $\alpha$ ) is calculated using the absorbance and thickness decided by the SEM images. The bandgap energy is estimated by extrapolating the linear part of the relationship between the  $(\alpha h\nu)^{1/2}$  and the photon energy with the assumption of an indirect bandgap transition[32]. The bandgap energies of 2.45, 2.45, 2.46, and 2.49 are obtained from the absorption edges of about 500 nm from W-O-H films prepared in the 0.01, 0.03, 0.05, and 0.09 mol/L  $\text{WO}_4^{2-}$  solutions. Furthermore, bandgap energies of 3.3, 3.27, and 3.25 eV were obtained from the absorption edge around 400 nm from W-O-H films prepared in the 0.09, 0.1, and 0.5 mol/L  $\text{WO}_4^{2-}$  solutions. The large  $\text{WO}_3\cdot\text{H}_2\text{O}$  square and  $\text{WO}_3\cdot(\text{H}_2\text{O})_{0.33}$  granular grains possessed bandgap energies of 2.45-2.49 eV and 3.25-3.3 eV, respectively, by considering the X-ray diffraction results and SEM observation.

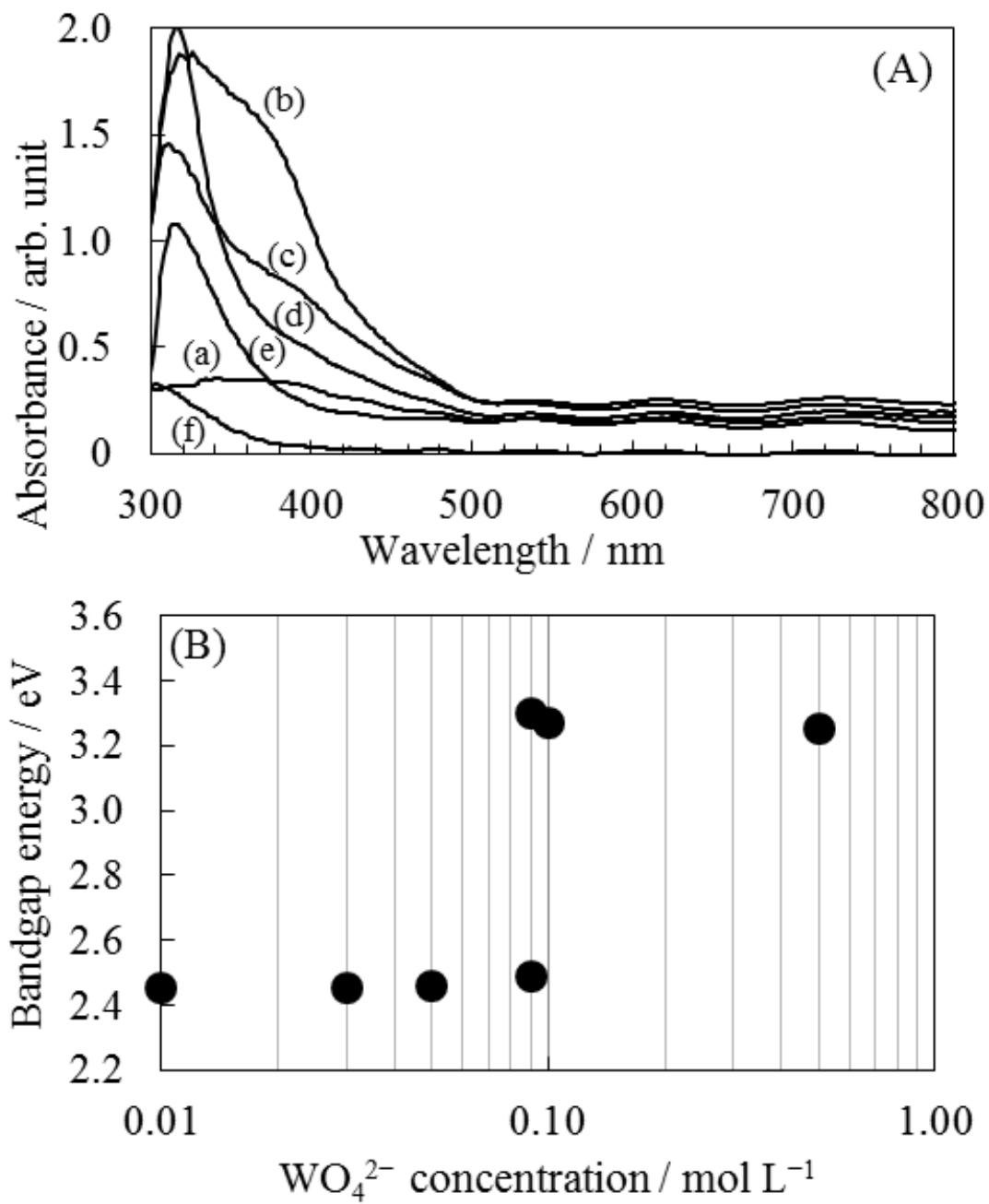


Fig. 3.8 Absorption spectra for W-O-H films prepared in the 0.01(a), 0.03(b), 0.05(c), 0.09(d), 0.1(e), and 0.5 mol/L(f)  $\text{WO}_4^{2-}$  solutions(A), and the correlation between bandgap energy and  $\text{WO}_4^{2-}$  concentration(B).

Both the  $\text{WO}_3 \cdot \text{H}_2\text{O}$  and  $\text{WO}_3 \cdot (\text{H}_2\text{O})_{0.33}$  possessed an orthorhombic lattice, and the lattice constant was different depending on the amount of water molecules introduced into the lattice. It was reported for the  $\text{Cu}(\text{In,Ga})(\text{S,Se})_2$  compounds that the bandgap energy proportionally changed from 1.04 to 2.34 eV depending on the lattice constant induced by the composition change[33]. This will be the reason for the difference of the bandgap energy for the  $\text{WO}_3 \cdot \text{H}_2\text{O}$  and  $\text{WO}_3 \cdot (\text{H}_2\text{O})_{0.33}$ .

The reaction schemes for the  $\text{WO}_3 \cdot \text{H}_2\text{O}$  and  $\text{WO}_3 \cdot (\text{H}_2\text{O})_{0.33}$  are not clear at present, but the following reaction according to the potential-pH diagram can be speculated.



The reaction was revised as follows from the formation of the tungsten oxide hydrate.



The difference of amount of the water molecules suggested that the  $\text{WO}_4^{2-}$  concentration affected the reaction equation(3.7) shown above.

### 3.3.3 Photoelectrochemical properties of $\text{WO}_3 \cdot \text{H}_2\text{O}$ and $\text{WO}_3 \cdot (\text{H}_2\text{O})_{0.33}$ films.

Photoresponse curves for W-O-H films prepared in the 0.03 and 0.1 mol/L  $\text{WO}_4^{2-}$  solutions recorded under a light irradiation with and without UV light are shown in Figure 3.9. The high-pressure Hg lamp source used in the measurement emitted UV-vis light at wavelength ranging from 300 to 600 nm.

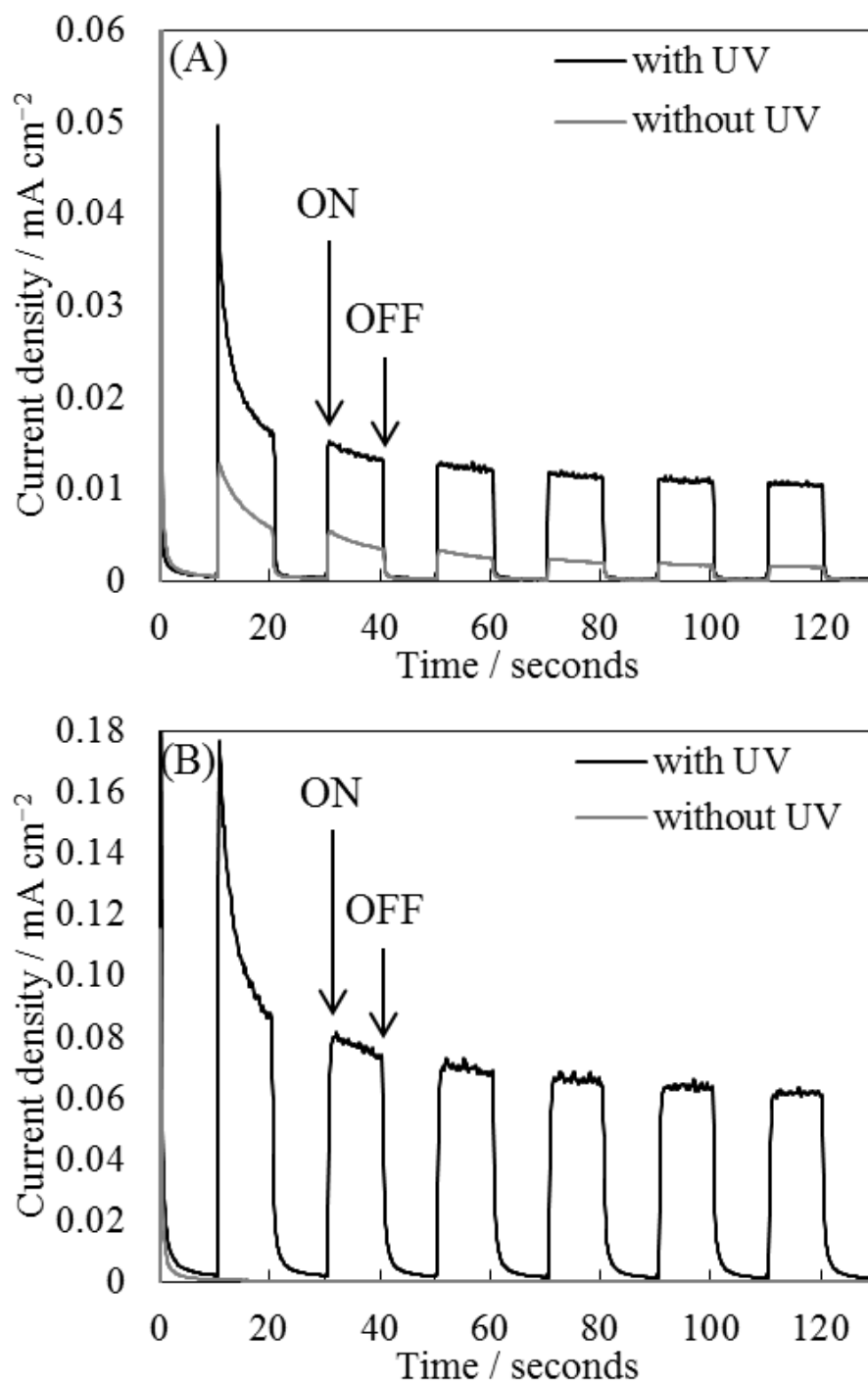


Fig. 3.9 Photoresponse curves for W-O-H films prepared in the 0.03(A) and 0.1 mol/L WO<sub>4</sub><sup>2-</sup> solutions(B) with and without UV irradiation in a 0.1 mol/L Na<sub>2</sub>SO<sub>4</sub> aqueous solution. The light irradiation started at “ON” and stopped at “OFF”.

When only visible light at 380–600 nm was irradiated, the UV light at 300–380 nm was eliminated by using an SnO<sub>2</sub> filter with a bandgap energy of 3.3 eV. Both W-O-H films prepared in the 0.03 and 0.1 mol/L WO<sub>4</sub><sup>2-</sup> solutions generated photocurrent density at only positive potential, and showed no change in current density at the negative potential side, suggesting that both W-O-H films are n-type semiconductors. The light irradiation started at “ON” and stopped at “OFF” is represented in the figure. The W-O-H films prepared in the 0.03 and 0.1 mol/L WO<sub>4</sub><sup>2-</sup> solutions are a mixture of 2.5-eV WO<sub>3</sub>·H<sub>2</sub>O and 3.3-eV WO<sub>3</sub>·(H<sub>2</sub>O)<sub>0.33</sub>, and single 3.3-eV WO<sub>3</sub>·(H<sub>2</sub>O)<sub>0.33</sub>, respectively. Photocurrent density increased immediately just after irradiating UV-vis light and then decreased to almost 10<sup>-3</sup> mA cm<sup>-2</sup> by stopping the light irradiation for both W-O-H films prepared in the 0.03 and 0.1 mol/L WO<sub>4</sub><sup>2-</sup> solutions. The maximum photocurrent density by irradiation of UV-vis light is observed at the first irradiation, and the value reaches a plateau after the fifth irradiations in each case. The maximum and plateau values are estimated to be 0.05 and 0.01 mA cm<sup>-2</sup> for the W-O-H films prepared in the 0.03 mol/L WO<sub>4</sub><sup>2-</sup> solution, while 0.18 and 0.06 mA cm<sup>-2</sup> for that in the 0.1 mol/L WO<sub>4</sub><sup>2-</sup> solution, respectively. The photocurrent generation by the irradiating light without containing UV light, i.e. visible light, is observed only for the W-O-H film prepared in the 0.03 mol/L WO<sub>4</sub><sup>2-</sup> solution. The irradiated visible light at wavelengths ranging from 380-600 nm corresponding to the photon energy of 3.26-2.06 eV excited electrons from the valence band to the conduction band only for WO<sub>3</sub>·H<sub>2</sub>O. Therefore, the W-O-H film prepared in the 0.03 M WO<sub>4</sub><sup>2-</sup> solution contained 2.5-eV WO<sub>3</sub>·H<sub>2</sub>O, and although the film was identified to be a mixture of 2.5-eV WO<sub>3</sub>·H<sub>2</sub>O and 3.3-eV WO<sub>3</sub>·(H<sub>2</sub>O)<sub>0.33</sub> from XRD results, the existence of 3.3-eV WO<sub>3</sub>·(H<sub>2</sub>O)<sub>0.33</sub> did not contribute to photocurrent generation. The W-O-H film prepared in the 0.1 WO<sub>4</sub><sup>2-</sup>

solution was identified to be the single 3.3-eV-WO<sub>3</sub>·(H<sub>2</sub>O)<sub>0.33</sub> film because of no photocurrent generation under the visible light irradiation.

### 3.4 Conclusions

Crystalline tungsten oxide hydrate films of  $\text{WO}_3 \cdot \text{H}_2\text{O}$  and  $\text{WO}_3 \cdot (\text{H}_2\text{O})_{0.33}$  were prepared on conductive glass substrates by anodic electrochemical deposition in aqueous solutions containing 0.01–0.5 mol/L  $\text{WO}_4^{2-}$  without any heat-treatment. The valence state of obtained tungsten oxide hydrate films were +6, and the films are proved to have high chemical uniformity. The large  $\text{WO}_3 \cdot \text{H}_2\text{O}$  grains with square shapes obtained in the 0.01–0.09 mol/L  $\text{WO}_4^{2-}$  solutions possessed a bandgap energy of approximately 2.5 eV, and granular- $\text{WO}_3 \cdot (\text{H}_2\text{O})_{0.33}$  films obtained in the 0.05–0.5 mol/L  $\text{WO}_4^{2-}$  solutions showed 3.3 eV in bandgap energy. Tungsten oxide hydrate films prepared in 0.01–0.9 mol/L  $\text{WO}_4^{2-}$  solutions possess excellent crystalline structures of  $\text{WO}_3 \cdot \text{H}_2\text{O}$  and  $\text{WO}_3 \cdot (\text{H}_2\text{O})_{0.33}$ , and it is a novel and advantageous factor of this method. The  $\text{WO}_3 \cdot \text{H}_2\text{O}$ - $\text{WO}_3 \cdot (\text{H}_2\text{O})_{0.33}$  mixed film prepared in the 0.03–0.09 mol/L  $\text{WO}_4^{2-}$  solutions showed a photoresponse for visible light at 380–600 nm, due to the existence of 2.5 eV-bandgap- $\text{WO}_3 \cdot \text{H}_2\text{O}$ . The  $\text{WO}_3 \cdot \text{H}_2\text{O}$  is a realistic candidate as a photomaterial such as a photocatalyst operative in visible light.

## REFERENCE

- [1 ] C.G. Granqvist, Electrochromic tungsten oxide films: Review of progress 1993–1998, *Sol. Energy Mater. Sol. Cells*, **60**, 201 (2000).
- [2] D.W. Hwang, J. Kim, T.J. Park, J.S. Lee, Mg-Doped  $\text{WO}_3$  as a Novel Photocatalyst for Visible Light-Induced Water Splitting, *Catal. Lett.*, **80**, 53 (2002).
- [3] J. Cao, B. Luo, H. Lin, B. Xu, S. Chen, Thermodecomposition synthesis of  $\text{WO}_3/\text{H}_2\text{WO}_4$  heterostructures with enhanced visible light photocatalytic properties, *Appl. Catal. B*, **111**, 288 (2012).
- [4] E. Avendaño, L. Berggren, G.A. Niklasson, C.G. Granqvist, A. Azens, Electrochromic materials and devices: Brief survey and new data on optical absorption in tungsten oxide and nickel, *Thin Solid Films*, **496**, 30 (2006).
- [5] D. Vernardou, H. Drosos, E. Spanakis, E. Koudoumas, N. Katsarakis, M.E. Pemble, Electrochemical properties of amorphous  $\text{WO}_3$  coatings grown on polycarbonate by aerosol-assisted CVD, *Electrochim., Acta*, **65**, 185 (2012).
- [6] I. Vamvasakis, I. Georgaki, D. Vernardou, G. Kenanakis, N. Katsarakis, Synthesis of  $\text{WO}_3$  catalytic powders: evaluation of photocatalytic activity under NUV/visible light irradiation and alkaline reaction pH, *J. Solgel. Sci. Technol.*, **76**, 120 (2015).
- [7] K. Psifis, D. Louloudakis, D. Vernardou, E. Spanakis, G. Papadimitropoulos, D. Davazoglou, N. Katsarakis, E. Koudoumas, Effect of  $\text{O}_2$  flow rate on the

electrochromic response of  $\text{WO}_3$  grown by LPCVD, *Physica status solidi (c)*, **12**, 1011 (2015).

[8] T. Takata, C. Pan, K. Domen, Recent progress in oxynitride photocatalysts for visible-light-driven water splitting, *Sci. Technol. Adv. Mater.*, **16**, 033506 (2015).

[9] K. Aguir, C. Lemire, D.B.B. Lollman, Electrical properties of reactively sputtered  $\text{WO}_3$  thin films as ozone gas sensor, *Sens. Actuators B Chem.*, **84**, 1 (2002).

[10] W. Wua, Q. Yu, J. Lian, J. Bao, Z. Liu, S.S. Pei, Tetragonal tungsten oxide nanobelts synthesized by chemical vapor deposition, *J. Cryst. Growth*, **312**, 3147 (2010).

[11] N. Sharma, M. Deepa, P. Varshney, S.A. Agnihotry, Influence of organic additive on the morphological, electrical and electrochromic properties of sol-gel derived  $\text{WO}_3$  coatings, *J. Solgel Sci. Technol.*, **18**, 167 (2000).

[12] J.H. Ha, P. Muralidharan, D.K. Kim, Hydrothermal synthesis and characterization of self-assembled h- $\text{WO}_3$  nanowires/nanorods using EDTA salts, *J. Alloys Compd.*, **475**, 446 (2009).

[13] T. Pauporté, Simple  $\text{WO}_3$  electrodeposition, *J. Electrochem. Soc.*, **149**, C539 (2002).

[14] K. Christou, D. Louloudakis, D. Vernardou, N. Katsarakis, E. Koudoumas, One-pot synthesis of  $\text{WO}_3$  structures at  $95^\circ\text{C}$  using HCl, *J. Solgel Sci. Technol.*, **73**, 520 (2015).

- [15] K. Christou, D. Louloudakis, D. Vernardou, C. Savvakis, N. Katsarakis, E. Koudoumas G. Kiriakidis, Effect of solution chemistry on the characteristics of hydrothermally grown  $\text{WO}_3$  for electroactive applications, *Thin Solid Films*, **594**, 333 (2015).
- [16] D. Vernardou, K. Psifis, D. Louloudakis, G. Papadimitropoulos, D. Davazoglou, N. Katsarakis, E. Koudoumas, Low Pressure CVD of Electrochromic  $\text{WO}_3$  at  $400^\circ\text{C}$ , *J. Electrochem. Soc.*, **162**, H579 (2015).
- [17] M. pourbaix, Atlas of Electrochemical Equilibria in Aqueous Solutions, NACE, Houston, TX, 1974, p.282.
- [18] J. Zhang, X.L. Wang, X.H. Xia, C.D. Gu, Z.J. Zhao, J.P. Tu, Enhanced electrochromic performance of macroporous  $\text{WO}_3$  films formed by anodic oxidation of DC-sputtered tungsten layers, *Electrochim. Acta*, **55**, 6953 (2010).
- [19] T. Shinagawa, Y. Ida, K. Mizuno, S. Watase, M. Watanabe, M. Inaba, A. Tasaka, M. Izaki, Controllable Growth Orientation of  $\text{Ag}_2\text{O}$  and  $\text{Cu}_2\text{O}$  Films by Electrocrystallization from Aqueous Solutions, *Cryst. Growth Des.*, **13**, 52 (2013).
- [20] M. Izaki, M. Nagai, K. Maeda, F.B. Mohamad, K. Motomura, J. Sasano, T. Shinagawa, S. Watase, Electrodeposition of 1.4-eV-Bandgap p-Copper (II) Oxide Film With Excellent Photoactivity, *J. Electrochem. Soc.*, **158**, D578 (2011).
- [21] B.N. Ryzhenko, Technology of Groundwater Quality Prediction: 1. Eh-pH Diagram and Detention Coefficient of Molybdenum and Tungsten in Aqueous Solutions, *Geochem. Int.*, **48**, 407 (2010).

- [22] B. Liu, J. Wang, J. Wu, H. Li, H. Wang, Z. Li, M. Zhou, T. Zuo, Proton exchange growth to mesoporous  $\text{WO}_3 \cdot 0.33\text{H}_2\text{O}$  structure with highly photochromic sensitivity, *Mater. Lett.*, **91**, 334 (2013).
- [23] C. Balazsi, J. Pfeifer, *Solid State Ion.*, Development of tungsten oxide hydrate phases during precipitation, room temperature ripening and hydrothermal treatment, **151**, 353 (2002).
- [24] J.F. Moulder, W.F. Stickle, P.E. Sobol, K.D. Bomben, J. Chastain (Eds.), R.C. King Jr. (Eds.), *Handbook of X-ray Photoelectron Spectroscopy: A Reference Book of Standard Spectra for Identification and Interpretation of XPS Data*, Physical Electronics USA Inc., Minnesota, United States of America, 1992, p172.
- [25] J.F. Moulder, W.F. Stickle, P.E. Sobol, K.D. Bomben, J. Chastain (Eds.), R.C. King Jr. (Eds.), *Handbook of X-ray Photoelectron Spectroscopy: A Reference Book of Standard Spectra for Identification and Interpretation of XPS Data*, Physical Electronics USA Inc., Minnesota, United States of America, 1992, p44.
- [26] J.F. Moulder, W.F. Stickle, P.E. Sobol, K.D. Bomben, J. Chastain (Eds.), R.C. King Jr. (Eds.), *Handbook of X-ray Photoelectron Spectroscopy: A Reference Book of Standard Spectra for Identification and Interpretation of XPS Data*, Physical Electronics USA Inc., Minnesota, United States of America, 1992, p241.
- [27] J.F. Moulder, W.F. Stickle, P.E. Sobol, K.D. Bomben, J. Chastain (Eds.), R.C. King Jr. (Eds.), *Handbook of X-ray Photoelectron Spectroscopy: A Reference Book of Standard Spectra for Identification and Interpretation of XPS Data*, Physical Electronics USA Inc., Minnesota, United States of America, 1992, p. 230.

- [28] S. Salmaoua, F. Sediri, N. Gharbi, C. Perruchot, M. Jouini, Hexagonal hydrated tungsten oxide nanomaterials: Hydrothermal synthesis and electrochemical properties, *Electrochim. Acta*, **108**, 634 (2013).
- [29] S. Deki, A.B. Béléké, Y. Kotani, M. Mizuhata, Synthesis of tungsten oxide thin film by liquid phase deposition, *Mater. Chem. Phys.* **123**, 614 (2010).
- [30] Joint committee of powder diffraction standards, Powder Diffraction File No. 01-084-0886, International Centre for Diffraction Data, Pennsylvania 2015.
- [31] Joint committee of powder diffraction standards, Powder Diffraction File No. 01-072-0199, International Centre for Diffraction Data, Pennsylvania 2015.
- [32] C.G. Granqvist, *Handbook of Inorganic Electrochromic Materials*, Elsevier, Amsterdam, The Netherlands, 1995, p. 139.
- [33] H.J. Möller (Eds.), *Semiconductors for Solar Cells*, Artech House, Inc., Boston, 1993, p. 36.

## **CHAPTER 4**

### Electrochemical deposition of tin oxide hydrate film

#### **4.1 Introduction**

##### **4.1.1 Materials and issues of existing electrochemical depositions for SnO<sub>2</sub>**

Tin oxide (SnO<sub>2</sub>) having “C type” (section 1.2) potential-pH diagram is a n-type semiconductor which has 3.6 eV of bandgap energy, and is applied to gas detective sensors, solar cells, transparent conductive films and ion injection layers for

rechargeable batteries[1-4]. Chemical state, composition, bandgap energy, morphology and structure of tin oxide films are very important for applications to photoelectric devices, and those properties depend on forming methods. SnO<sub>2</sub> films can be synthesized by numerous techniques such as sputtering [5], chemical vapor deposition[6], sol-gel dip coating[7], spray pyrolysis[8] and electrochemical deposition[9,10]. Electrochemical deposition processes have several advantages over gas-phase deposition processes, such as low cost, and high applicability to film preparation on wide and complicated substrates. Existing methods of electrochemical deposition for tin oxides utilize of the nitrate reduction reaction[9,10]; however, there is possibility of the incorporation of a tin oxide phase except for SnO<sub>2</sub> according to the potential-pH diagram[11], and the deposited tin oxide contain metal tin. This deposition of metal tin was caused by the reduction of Sn<sup>4+</sup> ions in the solution, and the introduced phases as mixed valence compounds could have harmful effects on the performance of photoelectronic devices.

#### **4.1.2 Anodic electrochemical deposition using oxidization reaction of dissolved ions**

Anodic electrochemical deposition using oxidization reaction of dissolved ions was reported by A. Switzer et al. in 1996[12], and AgO film was obtained by combination reaction of acid-base reaction and oxidation-reduction reaction. The theory of anodic electrochemical deposition for oxide is explained by the equation shown as follows:



$\text{Ag}^+$  ions dissolved in water was oxidized, and combined with  $\text{OH}^-$  ions to  $\text{AgO}$ . As understood from this, anodic electrochemical deposition can be applied to almost all oxides having “C type” potential-pH diagram explained in **Chapter 1**, and this method can deposit metal oxides with the maximum oxidation number.

### **4.1.3 Objective of this study**

In this chapter, I aim at developing the electrochemical deposition processes for tin oxides having high chemical uniformity based on thermodynamic calculation to solve the problems of existing processes and usability of anodic electrochemical deposition using oxidization-reaction of ion species for oxide semiconductor to be proved. Shown in the literature, the  $\text{AgO}$  film was prepared using combination reaction of acid-base reaction and oxidation-reduction reaction. Since the electrode potential is kept positive enough from the redox potential of  $\text{Sn}^{2+}/\text{SnO}_2$ , there is a possibility to obtain chemically uniform  $\text{SnO}_2$  films by anodic electrochemical deposition like  $\text{AgO}$ . Moreover, I speculated that this process would solve the problems of existing processes. Chemical and structural characterizations were carried out for obtained films with an X-ray photoelectron spectroscope, a grazing incidence X-ray diffraction, and a field emission scanning electron microscope observation.

## **4.2 Experimental**

### **4.2.1 Theory of electrochemical deposition for tin oxide hydrate compounds**

Before conducting the experiments of electrochemical deposition, I elaborated the potential-pH diagram of Sn-H<sub>2</sub>O system under the similar conditions to our investigation (Figure 4.1). The values of standard Gibbs energy of formation used for the thermodynamic calculations are summarized in Table 4.1[11]. In the calculations, the activities of the solvent water and pure solid materials were regarded as unity, and the activities of Sn<sup>2+</sup> ions and Sn<sup>4+</sup> ions were set to 0.001. In this study, I developed an anodic electrochemical deposition for the tin oxide from aqueous solution containing Sn<sup>2+</sup> ions based on thermodynamic calculations. When electrode potential was kept at a higher potential than that of the Sn<sup>2+</sup>/SnO<sub>2</sub> combination reaction of acid-base reaction and oxidation-reduction reaction, SnO<sub>2</sub> and Sn(OH)<sub>4</sub> are more stable on the electrode than Sn(II) species, and tin oxide were formed directly from the solution (equation (4.2),(4.3)).



Table 4.1 Standard Gibbs free energies of formation at 298.15 K used for drawing of the potential-pH diagram of Sn-H<sub>2</sub>O system[11].

Chemical species	$\Delta G_f^0$ [kJ/mol]
SnO <sub>2</sub> (s)	-515.0
Sn(OH) <sub>4</sub> (s)	-477.0
SnO(s)	-257.1
Sn <sup>4+</sup> (aq)	-2.7
Sn <sup>2+</sup> (aq)	-26.2
Sn(s)	0
H <sub>2</sub> O(l)	-237.1

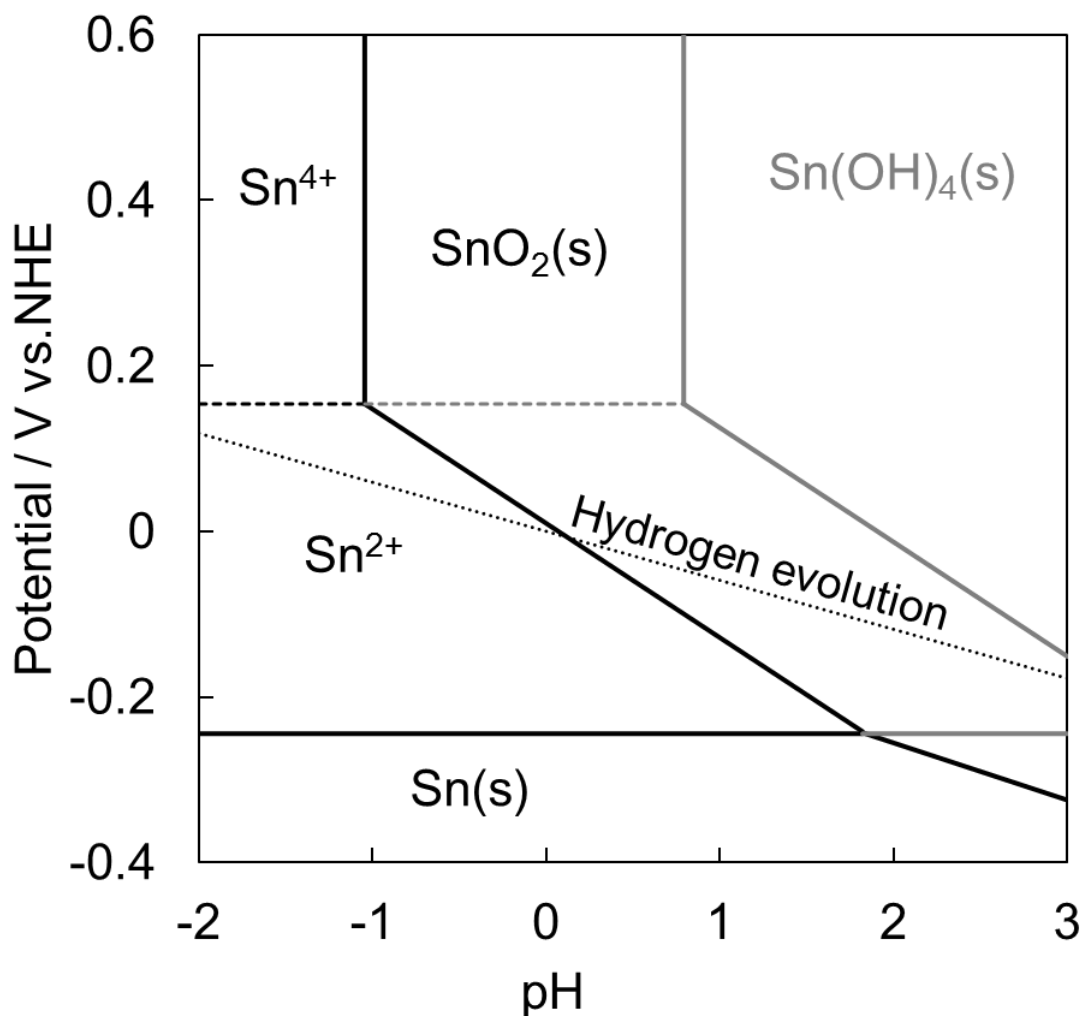


Figure 4.1 Potential-pH diagram of Sn-H<sub>2</sub>O system at 348 K. Concentration of each dissolved species was set at 1 mmol/L.

#### 4.2.2 Experimental procedure for electrochemical deposition of tin oxides hydrate compounds

Electrochemical deposition experiments were conducted based on the potential-pH diagram. The electrochemical deposition experiments were performed using a typical three-electrode electrochemical cell. The working, counter and reference electrodes

were an Au-coated Si wafer (Si/Au wafer), a platinum plate and an Ag/AgCl electrode (0.199 V vs. NHE), respectively. The substrate was rinsed with acetone by immersion. Then, it was masked with waterproof adhesive tape (Fluoroplastic Saturated Glass Cloth Tape NITOFロン No.973UL-S/973UL, Nitto) to restrict the exposed surface area of the substrate to 10 mm × 10 mm. The masked substrate was degreased by electrolytic degreasing (−10 mA/cm<sup>2</sup>, 1 min) in an aqueous sodium hydroxide solution with its concentration of 1.0 mol/L. The solvent for electrochemical deposition was prepared by adding 90 mmol/L sulfuric acid (H<sub>2</sub>SO<sub>4</sub> =96.0%, KANTO CHEMICAL) to deionized water. Then, 1 mmol/L tin(II) sulfate (SnSO<sub>4</sub> =93.0%, KANTO CHEMICAL) was added to the solvent. Deposition potential was decided by linear sweep voltammetry with 1 mmol/L SnSO<sub>4</sub> solution at 1.3 of pH, and the scan rate was 5 mV/s. Deposition parameters were set at +0.2 V (vs. Ag/AgCl), temperature of the cell was kept at 75°C using thermostatic water bath, and electrochemical deposition was conducted for 1 hour. A computer-controlled electrochemical measurement system (HSV-110, HOKUTO DENKO) was used for electrochemical deposition.

#### **4.2.3 Characterization of tin oxide hydrate compounds**

The electron spectra were recorded by an X-ray photoelectron spectroscope (XPS: PHI Quantera SXM-CI, ULVAC-PHI, Inc., monochromatized Al K $\alpha$  radiation). The pre-sputtering using Ar<sup>+</sup> ions accelerated at 1.0 kV was carried out in an area of 2.0×2.0  $\mu\text{m}^2$  on the surface of films for 18 seconds before measurement. The binding energy was corrected by the C1s peak at 284.6 eV. The relative sensitivity factor of 0.733 and 4.890 for O1s and Sn3d orbitals were used for the calculation of molar ratio of Sn and O

elements. The chemical states of the deposited species on the surface of the sample were investigated with an Attenuated Total Reflection method (ATR) of Fourier transform infrared spectroscopy (FT-IR: FT-IR-6300, JASCO). The structures of the deposited films were identified by a grazing incidence X-ray diffraction (GIXD: RINT2500, Rigaku) technique with monochromatized Cu K $\alpha$  radiation set at 40 kV and 200 mA. Glancing angle of X-ray was set at 4°, and 2 $\theta$  scan was carried out. A field emission scanning electron microscope (FE-SEM) was used for observing the surface and the cross-sectional structure with an accelerating voltage of 3.0 kV. Optical absorption spectra was recorded by a spectrophotometer (UV-Vis-NIR: U4100, HITACHI Hightech) with the reference of bare Si/Au substrate.

### **4.3 Results and discussion**

#### **4.3.1 Composition of tin oxide hydrate compounds**

Figure 4.2 shows linear sweep voltamogram for the 1 mmol/L SnSO<sub>4</sub> solution at pH of 1.3. The rising edge of current for SnO<sub>2</sub> forming was observed at approximately +0.12 V vs. Ag/AgCl, and another rising edge of current for oxidization-reaction from Sn<sup>2+</sup> to Sn<sup>4+</sup> was observed at approximately +0.27 V vs. Ag/AgCl; these results are consistent with the potential-pH diagram, and deposition potential was set at the +0.2 V vs. Ag/AgCl.

Figure 4.3 shows the chronoamperometric curves in the 1 mmol/L SnSO<sub>4</sub> solution. The films did not peel off from the substrates for 60 min electrochemical deposition.

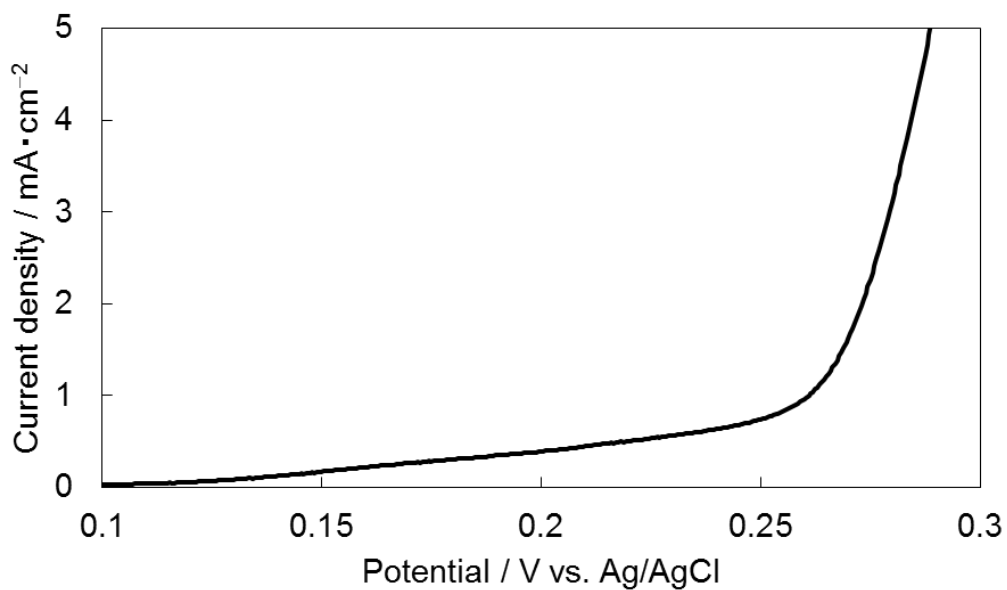


Figure 4.2 Linear sweep voltammogram of Au wafer in 1mmol/L SnSO<sub>4</sub> and H<sub>2</sub>SO<sub>4</sub> 90mM solution at 70° ; scan rate was 5 mV/s.

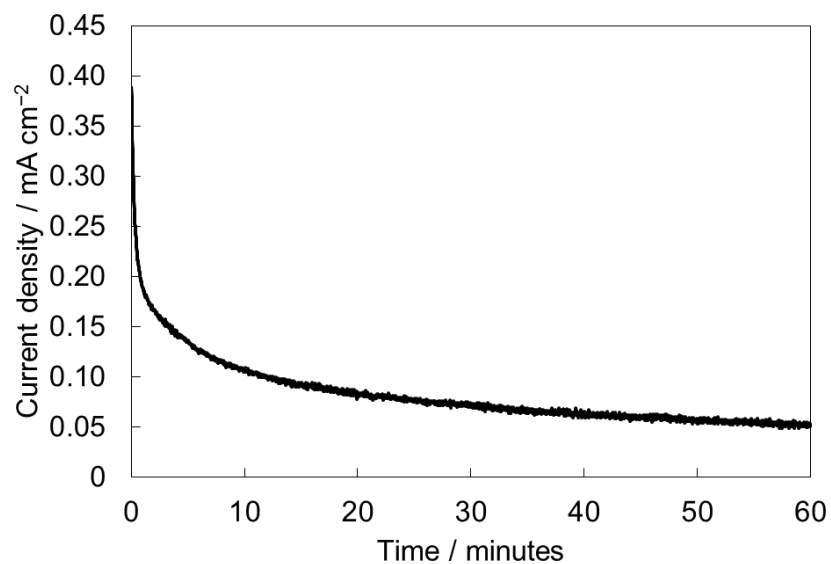


Fig. 4.3 Change in current density for electrochemical deposition with the deposition time in 1 mmol/L SnSO<sub>4</sub> solutions.

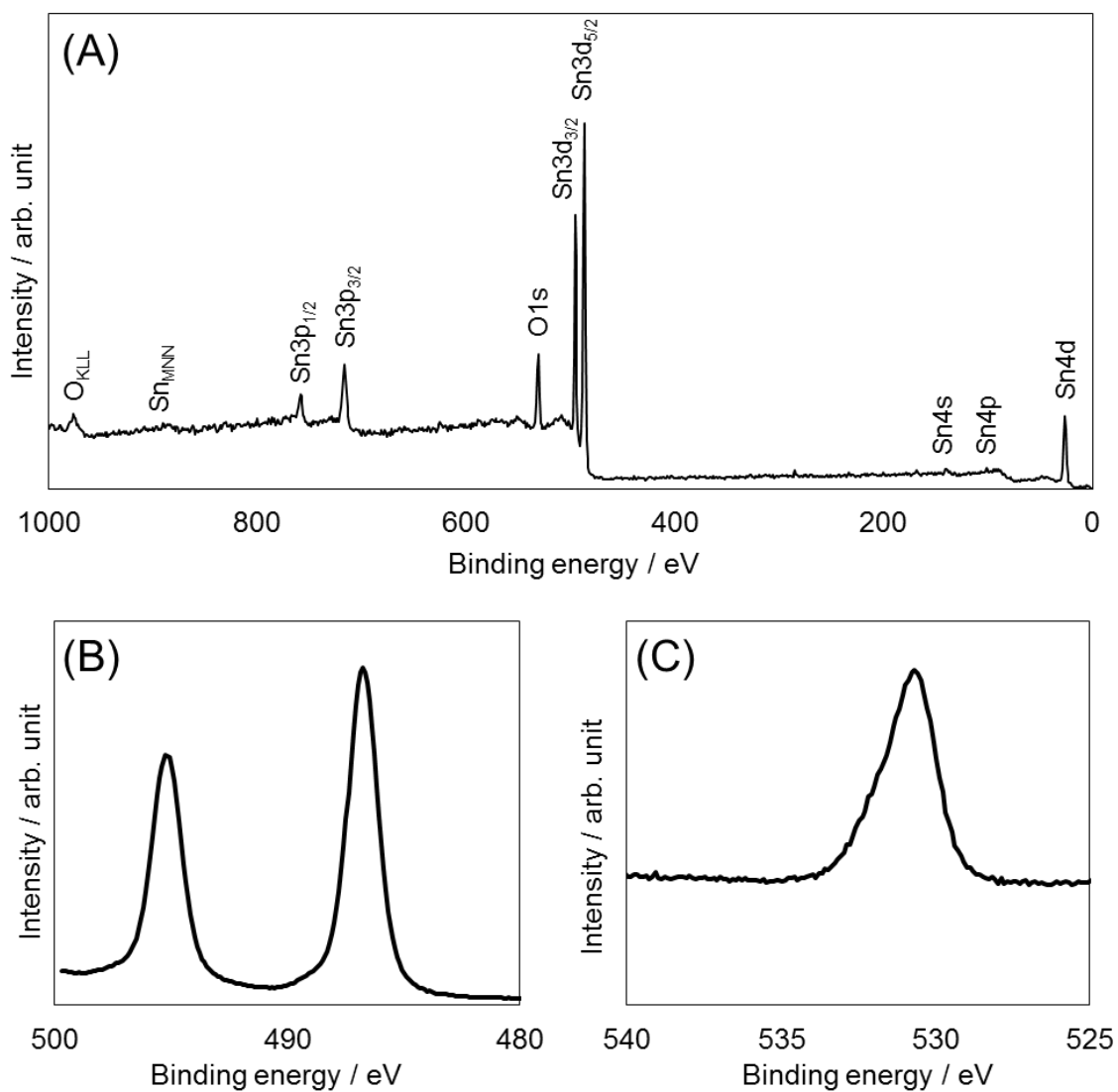


Figure 4.4 Survey(A), Sn3d(B), and O1s electron spectra(C) for tin oxide film.

The current density drastically decreased at the initial stage and then gradually decreased to an almost constant value. The current density at the deposition time of 60 min was around  $0.05 \text{ mA cm}^{-2}$ .

Colorless deposits were observed on the electrode with the naked eye. Figure 4.4 shows the results of XPS measurements for the survey electron spectrum and narrow

electron spectra of Sn3d and O1s for the obtained film. All the peaks on the survey spectrum are able to be identified as peaks originating from the Sn and O elements. Peaks at about 27, 90, 137, 487, 495, 717, 759, 886 and 1061 eV are identified with Sn4d, Sn4p, Sn4s, Sn3d<sub>5/2</sub>, Sn3d<sub>3/2</sub>, Sn3p<sub>3/2</sub>, Sn3p<sub>1/2</sub>, Sn3s, Sn<sub>MNN</sub> for Sn element, and peaks at 530.7 and 974.7 eV are assigned to O1s and O<sub>KLL</sub> electron spectra[13,14]. Any peaks originating from other elements were not detected on the spectrum, and this means that tin oxide film prepared by anodic electrochemical deposition in the SnSO<sub>4</sub> solution was composed of only Sn and O elements. Sn3d<sub>5/2</sub> peaks in XPS spectrum for tin oxide film have binding energy of 486.78 eV, and this value is closer to 486.7 eV of Sn<sup>4+</sup> in SnO<sub>2</sub> than 486.9 eV of Sn<sup>2+</sup> in SnO[15]. All observed peaks of tin had valence value of +4, and this film is proved to have high chemical uniformity. The O1s spectrum for the film prepared by anodic electrochemical deposition in the SnSO<sub>4</sub> solution showed a peak at 530.7 eV and a shoulder peak at 532.0 eV. The binding energy of 530.7 eV is close to the state of O<sup>2-</sup> in SnO<sub>2</sub>[16]. The peak at 532.0 eV was reported to be unidentified, but the value was smaller than 533.2 eV of H<sub>2</sub>O[16]. It can be assumed that this unidentified peak was originated in tin hydrate according to similar peak of metal hydrate can be observed in literature[17], but there is no particular evidence from the XPS measurement. The intensity ratio of the shoulder to the peak is estimated to be 0.33. Additionally, the molar ratios of the O to Sn elements calculated from integrated intensities of peaks with the relative sensitivity factor are 1.8.

Figure 4.5 shows the FT-IR absorption spectra of the film surface investigated with an ATR attachment.

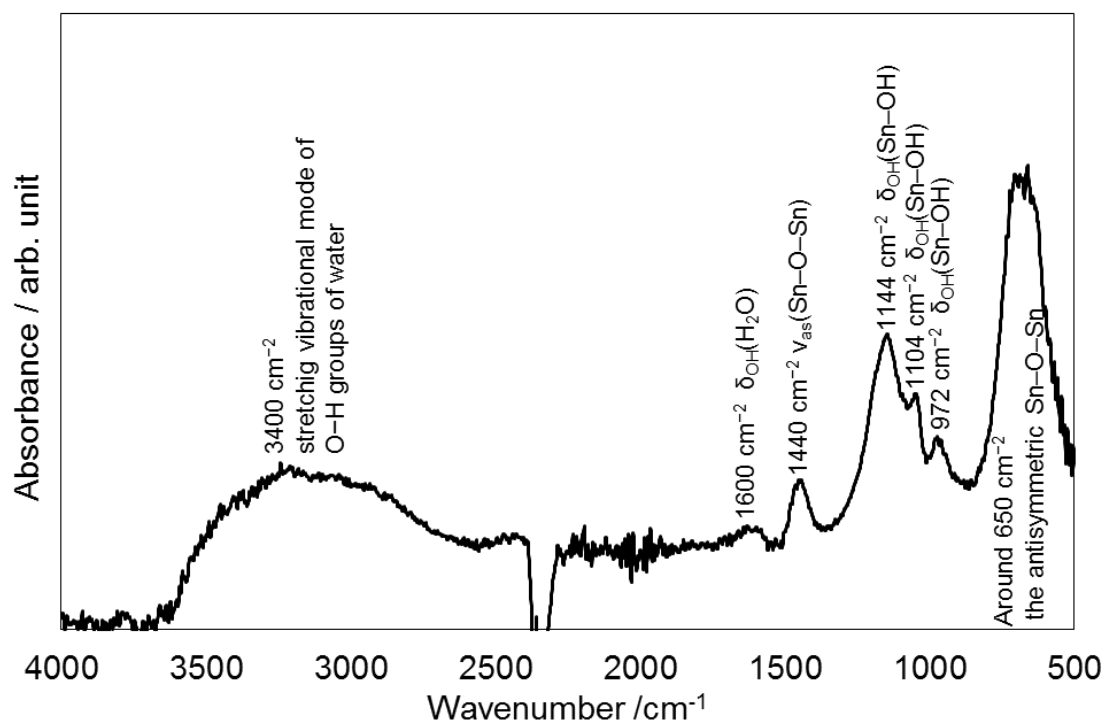


Figure 4.5 FT-IR absorption spectrum of the tin oxide film deposited on a Si/Au electrode.

The absorption peak at around  $650\text{ cm}^{-1}$  is assigned to Sn-O symmetric stretching vibration[18]; the absorbance of  $1440\text{ cm}^{-1}$  is assigned to the Sn-O-Sn antisymmetric stretching vibration[19]. This indicates the presence of  $\text{SnO}_2$  in the film. Moreover, absorption peaks at 970, 1100 and  $1140\text{ cm}^{-1}$  correspond to Sn-OH symmetric plane bending vibration[19,20], and the broad absorption around  $3400\text{ cm}^{-1}$  is assigned to O-H stretching[20]. This means that the film also includes  $\text{Sn(OH)}_4$ . In addition, the absorption peak at  $1600\text{ cm}^{-1}$  is assigned to the H-O-H symmetric plane bending vibration[20], showing the presence of a small amount of water molecules in it.

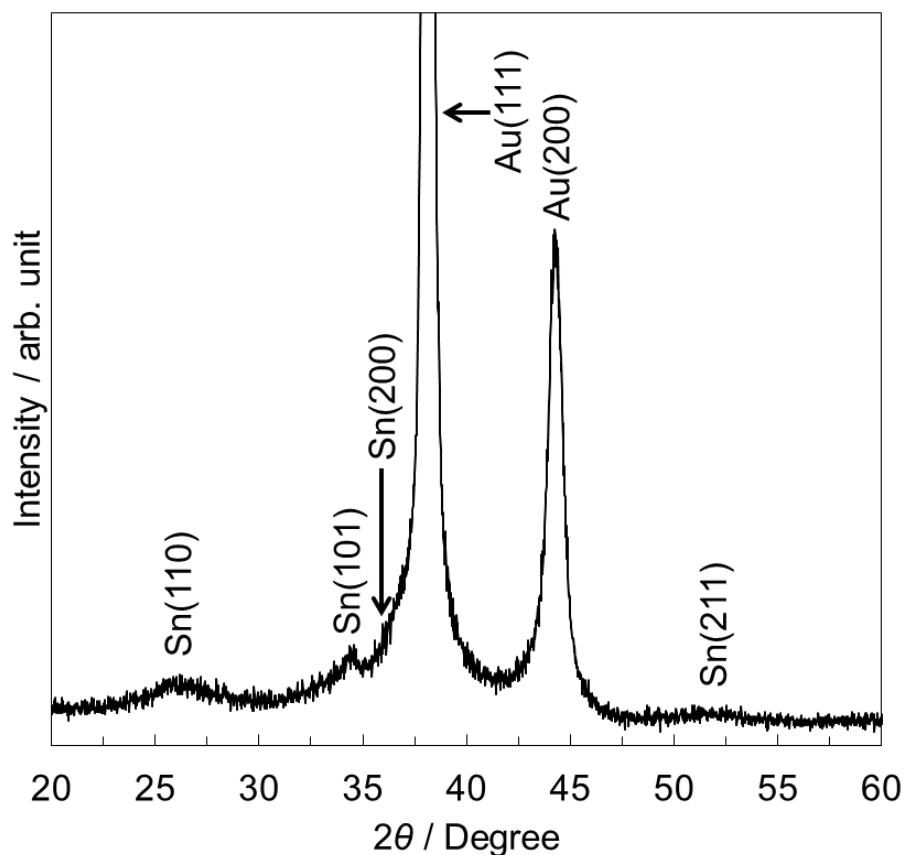


Fig. 4.6 GIXD patterns of Sn(O,OH).

Considering this result together with the XPS results, the obtained film is compounds of SnO<sub>2</sub> and Sn(OH)<sub>4</sub> (Sn(O,OH)).

#### 4.3.2 Structural characterization of tin oxide hydrate compounds

Figure 4.6 shows the XRD pattern of Sn(O,OH). The diffracted X-ray pattern for Sn(O,OH) film shows peaks at 26.1, 34.5, 36.6 and 52.7°, which are assigned to the (110), (101), (200) and (211) planes of SnO<sub>2</sub> with a tetragonal lattice, respectively[21].

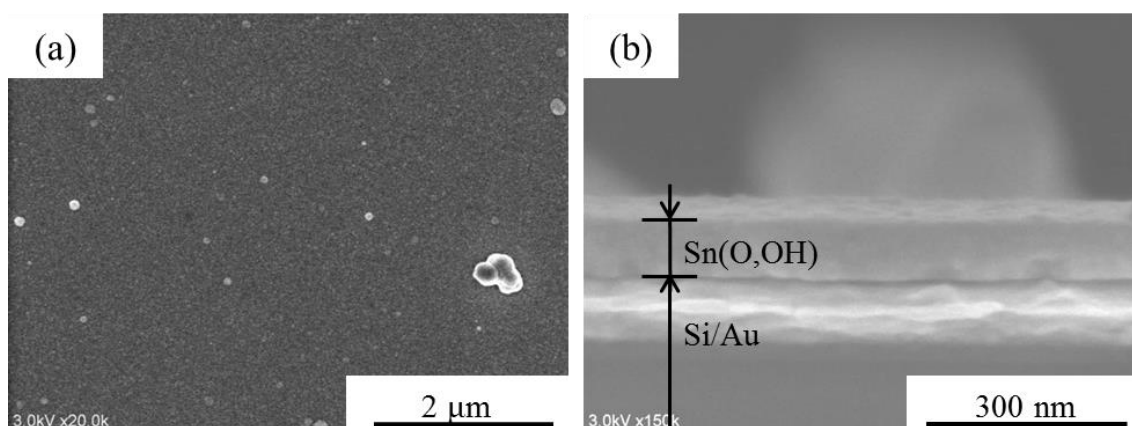


Figure 4.8 Surface(a) and cross-sectional(b) SEM images of the tin oxide film deposited on a Si/Au electrode.

The FWHM of X-ray diffraction peaks relate to grain size and inhomogeneous strain, and broad peaks of  $\text{SnO}_2$  indicate that small grain size and the presence of inhomogeneous strain. This inhomogeneous strain was originated in the presence of tin hydrate and oxygen vacancy in  $\text{Sn(O,OH)}$ . The lattice constants are calculated from the (110) and (211) planes, and the lattice constants of  $a$  and  $c$  of tetragonal  $\text{SnO}_2$  are  $4.931 \text{ \AA}$  and  $2.913 \text{ \AA}$ . These values have difference from the standard value, and the volume of the unit cell was calculated to be  $67.98 \text{ \AA}^3$ , which was smaller by approximately 5% than the standard value.

Figure 4.7(a) shows the SEM image of the surface of the tin oxide film deposited on a Si/Au electrode. The surface of the electrode is completely covered with deposits. The deposited film does not have cracks, and its surface is very smooth. Spherical particles on the surface of the films are seen in Figure 4.7(a). These particles appear to be tin oxides deposited from bulk solution since electrochemical reactions occurred not only

in the vicinity of the electrode but also in the bulk solution. Equation (4.4) shows the oxidation of  $\text{Sn}^{2+}$  ions into  $\text{Sn}(\text{OH})_4$  by dissolved oxygen in the bulk solution[22].



Since standard Gibbs energy of reaction of equation (4) is  $-4.4$  kJ/mol, the reaction is able to occur in the bulk solution, and  $\text{Sn}^{4+}$  ions spontaneously turned to  $\text{SnO}_2$  leading to deposition because  $\text{Sn}^{4+}$  ions could not stably exist under the pH condition of 1.3 in this solution. Figure 4.7(b) shows cross-sectional SEM images of the tin oxide film deposited on a Si/Au electrode. The film thickness is about 100 nm.

#### **4.4 Conclusions**

Chemically uniform Sn(O,OH), mixtures of tin oxide (SnO<sub>2</sub>) and tin hydroxide (Sn(OH)<sub>4</sub>) was formed by anodic electrochemical deposition using the combination reaction of acid-base reactions and oxidation-reduction reactions based on thermodynamic calculations. Obtained Sn(O,OH) completely covered the substrate, and have smooth surface and structure of tetragonal fine crystal.

Formation of Sn(O,OH) film composed of Sn having only a single oxidation state of +4 was achieved by electrochemical deposition based on the potential-pH diagram and electrochemical measurements.

## REFERENCE

- [1] M. Batzill, U. Diebold, The surface and materials science of tin oxide, *Prog. Surf. Sci.*, **79**, 47 (2005).
- [2] B. Thangaraju, Structural and electrical studies on highly conducting spray deposited fluorine and antimony doped SnO<sub>2</sub> thin films from SnCl<sub>2</sub> precursor, *Thin Solid Films*, **402**, 71 (2002).
- [3] J. Qian, P. Liu, Y. Xiao, Y. Jiang, Y. Cao, X. Ai, H. Yang, TiO<sub>2</sub>-Coated Multilayered SnO<sub>2</sub> Hollow Microspheres for Dye-Sensitized Solar Cells, *Adv. Mater.*, **21**, 3663 (2009).
- [4] J.Y. Huang, L. Zhong, C.M. Wang, J.P. Sullivan, W. Xu, L.Q. Zhang, S.X. Mao, N.S. Hudak, X.H. Liu, A. Subramanian, H. Fan, L. Qi, A. Kushima, J. Li, In situ observation of the electrochemical lithiation of a single SnO<sub>2</sub> nanowire electrode, *Science*, **330**, 1515 (2010).
- [5] M. Ruske, G. Bräuer, J. Pistner, U. Pfäfflin, J. Szczyrbowski, Properties of SnO<sub>2</sub> films prepared by DC and MF reactive sputtering, *Thin Solid Films*, **351**, 146 (1999).
- [6] M. Kwoka, L. Ottaviano, J. Szuber, AFM study of the surface morphology of L-CVD SnO<sub>2</sub> thin films, *Thin Solid Films*, **515**, 8328 (2007).
- [7] O.K. Varghese, L. K. Malhotra, Studies of ambient dependent electrical behavior of nanocrystalline SnO<sub>2</sub> thin films using impedance spectroscopy, *J. Appl. Phys.*, **87**, 7457 (2000).

- [8] C. Agashe, S.S. Major, Effect of heavy doping in SnO<sub>2</sub>:F films, *J. Mater. Sci.*, **31**, 2965 (1996).
- [9] S.T. Chang, I.C. Leu, M.H. Hon, Electrodeposition of nanocrystalline SnO<sub>2</sub> coatings with two-layer microstructure, *J. Cryst. Growth.*, **273**, 195 (2004).
- [10] J.J.M. Vequizo, J. Wang, M. Ichimura, Electrodeposition of SnO<sub>2</sub> Thin Films from Aqueous Tin Sulfate Solutions, *Jpn. J. Appl. Phys.*, **49**, 125502 (2010).
- [11] M. pourbaix, Atlas of Electrochemical Equilibria in Aqueous Solutions, NACE, Houston, TX, 1974, p.282.
- [12] B.E. Breyfogle, C.J. Hung, M.G. Shumsky, J.A. Switzer, Electrodeposition of Silver(II) Oxide Films, *J. Electrochem. Soc.*, **143**, 2741 (1996).
- [13] J.F. Moulder, W.F. Stickle, P.E. Sobol, K.D. Bomben, J. Chastain (Eds.), R.C. King Jr. (Eds.), Handbook of X-ray Photoelectron Spectroscopy: A Reference Book of Standard Spectra for Identification and Interpretation of XPS Data, Physical Electronics USA Inc., Minnesota, United States of America, 1992, p126.
- [14] J.F. Moulder, W.F. Stickle, P.E. Sobol, K.D. Bomben, J. Chastain (Eds.), R.C. King Jr. (Eds.), Handbook of X-ray Photoelectron Spectroscopy: A Reference Book of Standard Spectra for Identification and Interpretation of XPS Data, Physical Electronics USA Inc., Minnesota, United States of America, 1992, p44.
- [15] J.F. Moulder, W.F. Stickle, P.E. Sobol, K.D. Bomben, J. Chastain (Eds.), R.C. King Jr. (Eds.), Handbook of X-ray Photoelectron Spectroscopy: A Reference Book of Standard Spectra for Identification and Interpretation of XPS Data, Physical Electronics USA Inc., Minnesota, United States of America, 1992, p239.

- [16] J.F. Moulder, W.F. Stickle, P.E. Sobol, K.D. Bomben, J. Chastain (Eds.), R.C. King Jr. (Eds.), Handbook of X-ray Photoelectron Spectroscopy: A Reference Book of Standard Spectra for Identification and Interpretation of XPS Data, Physical Electronics USA Inc., Minnesota, United States of America, 1992, p231.
- [17] T.L. Barr, ESCA studies of naturally passivated metal foils, *J. Vac. Sci. Technol.*, **14**, 660 (1977).
- [18] T.V. Tran, S. Turrell, M. Eddafi, B. Capoen, M. Bouazaoui, P. Roussel, S. Berneschi, G. Righini, M. Ferrari, S.N.B. Bhaktha, O. Cristini, C. Kinowski, Investigations of the effects of the growth of SnO<sub>2</sub> nanoparticles on the structural properties of glass–ceramic planar waveguides using Raman and FTIR spectroscopies, *J. Mol. Struct.*, **976**, 314 (2010).
- [19] D. Amalric-Popescu, F. Bozon-Verduraz, Infrared studies on SnO<sub>2</sub> and Pd/SnO<sub>2</sub> *Catalysis Today*, **70**, 139 (2001).
- [20] S.N. Pusawale, P.R. Deshmukh, C.D. Lokhande, Chemical synthesis of nanocrystalline SnO<sub>2</sub> thin films for supercapacitor application, *Appl. Surf. Sci.*, **257**, 9498 (2011).
- [21] Joint committee of powder diffraction standards, Powder Diffraction File No. 01-077-0448, International Centre for Diffraction Data, Pennsylvania 2015.
- [22] S.L. Chou, J.Z. Wang, H.K. Liu, S.X. Dou, SnO<sub>2</sub> meso-scale tubes: One-step, room temperature electrodeposition synthesis and kinetic investigation for lithium storage, *Electrochem. commun.*, **11**, 242 (2009).

## **CHAPTER 5**

Solid state tungsten oxide hydrate/tin oxide hydrate  
electrochromic device prepared by electrochemical depositions

### **5.1 Introduction**

#### **5.1.1 Subject of this Chapter**

By the previous chapter, I have demonstrated examples of developing for electrochemical deposition processes based on potential-pH diagrams. Here, I demonstrate fabricating optical functional device prepared by previously mentioned

electrochemical depositions to solve a problem for existing devices, and suggest applicability of these electrochemical depositions based on thermodynamic calculations.

### 5.1.2 Electrochromic device

Electrochromic devices (ECDs) have been applied to cabin windows, anti-glare interior mirrors, and windshields installed into automobiles and airplanes for changing color appearances driven by electrochemical reactions[1]. The ECD was composed mainly of an electrochromic layer and an electrolyte layer for ion injection to change the color appearance. Since liquid phase electrolyte limits the industrial use due to leakage, solid state ECD has several advantages such as non-leakage and shape-flexibility over the conventional ECD with an electrolyte. The oxide hydrate such as tungsten oxide was used as the electrochromic layer for both conventional and solid state ECD[2,3], and oxide layers of rare metals like tantalum and iridium were used as the solid state ion-injection layers. Tin oxide hydrate,  $\text{Sn}(\text{O},\text{OH})$ , has been used as a component in a secondary battery as solid electrolyte and has a role to inject ions into the electrode[4]. The  $\text{Sn}(\text{O},\text{OH})$  layer is a realistic candidate as the solid electrolyte for injecting ions into the electrochromic layers installed in solid state ECDs. The tungsten and tin oxide hydrate layers have been prepared by several processes including gas- and solution-phase depositions[5-9]. The solution process has several advantages over the gas-phase deposition has already reported<sup>19-21</sup>. Direct anodic and cathodic depositions have been proposed by our group, and the ability has been approved by preparations of ZnO,  $\text{Cu}_2\text{O}$  and CuO semiconductors[10-12]. The tungsten oxide hydrate ( $\text{WO}_3(\text{H}_2\text{O})_{0.33}$ ) has been prepared by anodic deposition, and it is

expected that the preparation of the Sn(O,OH) by the anodic deposition from the electrochemical characteristic[13]. In this **Chapter 5**, I realize the fabrication of a solid state tungsten oxide hydrate/tin oxide hydrate electrochromic device by anodic deposition in aqueous solutions and demonstrate the change in the color appearance by applying voltage through it.

## **5.2 Experimental**

### **5.2.1 Fabrication of a FTO/WO<sub>3</sub>(H<sub>2</sub>O)<sub>0.33</sub>/Sn(O,OH) bilayer structure**

Prior to electrochemical deposition, the fluorine-doped tin oxide glass (10 Ω/□, FTO) substrate was rinsed with acetone, and then the electrochemical deposition area was limited to 15 mm × 15 mm by waterproof adhesive tape (Fluoroplastic Saturated Glass Cloth Tape NITOFLOX No. 973UL-S/973UL, Nitto). Then, the substrate was degreased by cathodic polarization at 10 mA cm<sup>-2</sup> for 3 min in a 1.0 mol/L sodium hydroxide aqueous solution. Tungsten oxide layers are prepared by decreasing the pH value in the vicinity of the substrate with an oxygen gas evolution reaction as mentioned in **Chapter 3**. The tungsten oxide hydrate layer was prepared on a FTO substrate by electrochemical deposition in an aqueous solution containing a 0.1 mol/L Na<sub>2</sub>WO<sub>4</sub>·2H<sub>2</sub>O at pH of 1.0, 70°C, and a potential of +2.0 V referenced to Ag/AgCl electrode for 2 hours by using a typical three-electrode electrochemical cell. The electrochemical deposition for Sn(O,OH) layer was performed using a typical three-electrode electrochemical cell as **Chapter 4**. The tin oxide hydrate layer was stacked on the tungsten oxide hydrate layer in an aqueous solution containing a 90 mmol/L H<sub>2</sub>SO<sub>4</sub> and 1 mmol/L SnSO<sub>4</sub> at 70°C and a potential of +0.2 V referenced to Ag/AgCl electrode for

2 hours. The solutions were prepared with reagent grade chemicals and deionized water purified with Milli-Pore Elix-Advantage.

### **5.2.2 Characterizations of a FTO/WO<sub>3</sub>(H<sub>2</sub>O)<sub>0.33</sub>/Sn(O,OH) bilayer structure**

The electron spectra were recorded by an X-ray photoelectron spectroscope (XPS). The Ar<sup>+</sup> sputtering was carried out at 2.0 kV for 1 minute before measurements. The binding energy was corrected by the C1s peak at 284.6 eV. The cross-sectional images were observed with a field emission scanning electron microscope (FE-SEM). Au electrode formed on Si wafer was contacted to the Sn(O,OH) layer, and a voltage of 5 V was applied between the Au electrode and FTO layer for 1 min. Optical transmission spectra were recorded by UV-visible-near infrared (UV-vis-NIR) spectroscopy.

## **5.3 Results and discussion**

### **5.3.1 Characterizations of a FTO/WO<sub>3</sub>(H<sub>2</sub>O)<sub>0.33</sub>/Sn(O,OH) bilayer structure**

Figure 5.1 shows Sn3d(a), W4f(b), and O1s(c) electron spectra for tungsten oxide hydrate/tin oxide hydrate bilayer after 2 min (solid line) and 25 min (dashed line) Ar sputtering, and the depth profiles of W, Sn and O elements(d). The intensity of the Sn3d signal was strong near the free surface and decreased with increase in the etching time, and the W4f signal showed very weak intensity near free surface and increased with increase in the etching time.

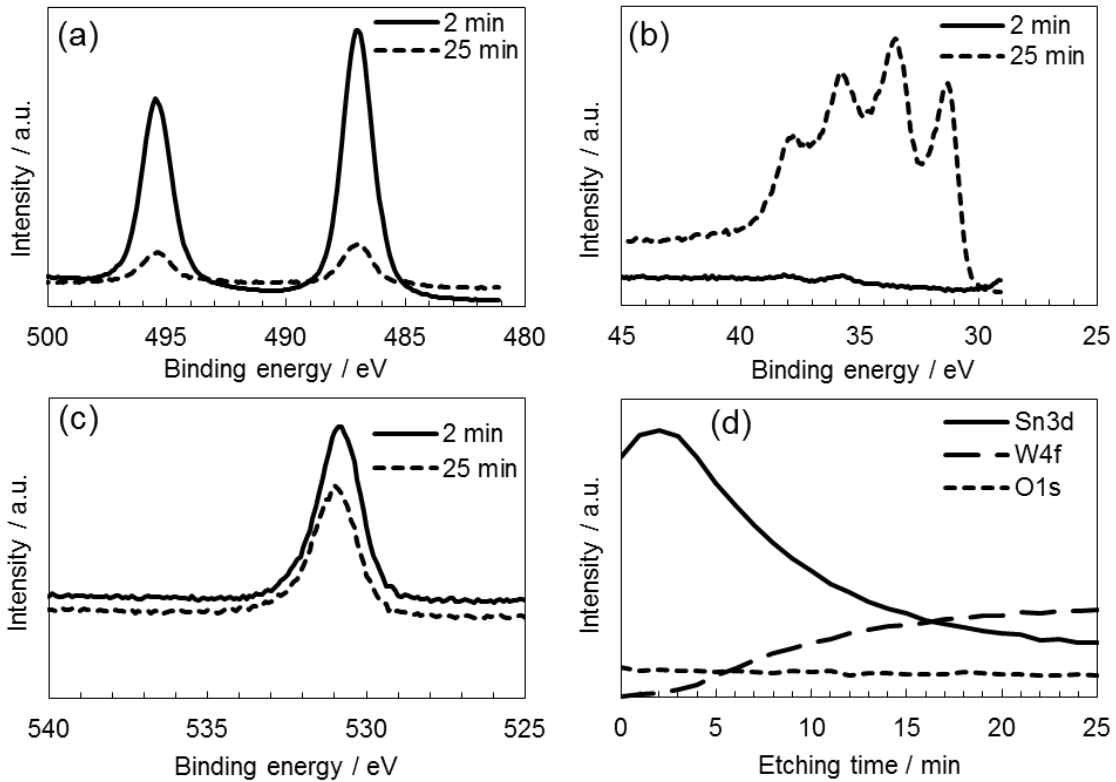


Figure 5.1 Sn3d(a), W4f(b) and O1s(c) electron spectra in  $\text{WO}_3(\text{H}_2\text{O})_{0.33}/\text{Sn}(\text{O},\text{OH})$  structure after sputtering for 2 (solid) and 25 min (dashed), and depth profiles of W, Sn and O elements(d).

The tendency of the intensity change for Sn3d and W4f signal was consistent with the bilayer structure of upper Sn(O,OH) and lower  $\text{WO}_3(\text{H}_2\text{O})_{0.33}$ . The state of Sn, W, and O elements were investigated by recording the Sn3d and O1s spectra for upper Sn(O,OH) layer at 2 min in the etching time and W4f and O1s spectra for  $\text{WO}_3(\text{H}_2\text{O})_{0.33}$  at 25 min in etching time. Although the intensity of Sn3d signal changed depending on the etching time, almost same spectra in peak energy and profile were observed irrespective of sputtering time. The Sn3d peaks at 487.0° and 495.5° were assigned to Sn3d of  $\text{Sn}^{4+}$  state in  $\text{SnO}_2$ [14]. The Sn3d signal remained even at the etching time of 25 min, but no change in profile was observed. The O1s signal showed 530.8 eV,

irrespective of the etching time, and the value was close to 530.6 eV of  $O^{2-}$  in both  $SnO_2$  and  $WO_3$ [14]. Shoulders were able to be observed at 532.3 eV for both spectra and were assigned to the  $O^{2-}$  state in hydroxides including  $WO_3(H_2O)_{0.33}$ [14]. The W4f signals appeared at 38 and 36 eV with very weak intensity at 2 min sputtering in the  $Sn(O,OH)$  layer region, and strong peaks at 37.8, 35.7, 33.5 and 31.3 eV were clearly observed at 25 min sputtering in  $WO_3(H_2O)_{0.33}$  layer region. The W4f peaks around 38 eV and 36 eV were assigned to  $W4f_{7/2}$  and  $W4f_{5/2}$  orbitals of  $W^{6+}$  species[15], and  $W4f_{7/2}$  orbital was close to 35.6 eV of  $W^{6+}$  state in  $WO_3$  and smaller than 36.2 eV of  $W^{6+}$  state in  $H_2WO_4$ [14]. The peaks at 33.5 and 31.3 eV were identified as  $W^0$  state, suggesting the occurrence of the reduction of W element by 25 min-Ar sputtering.

Figure 5.2 shows the cross-sectional SEM image of the  $WO_3(H_2O)_{0.33}/Sn(O,OH)$  structure. The 400 nm-thick- $WO_3(H_2O)_{0.33}$  layer was clearly observed on the FTO substrate and was composed of aggregates of equiaxed granular grains with the size of 50 nm. The 80-nm-thick  $Sn(O,OH)$  layer, which was composed of aggregates of granular grains of 30 nm in size, covered over entire the surface of the  $WO_3(H_2O)_{0.33}$  layer. The defects such as pores could not be located in both layers, and heterointerface was able to be clearly observed between two layers. It was confirmed that the formation of the  $WO_3(H_2O)_{0.33}/Sn(O,OH)$  bilayer structure was realized only by anodic deposition.

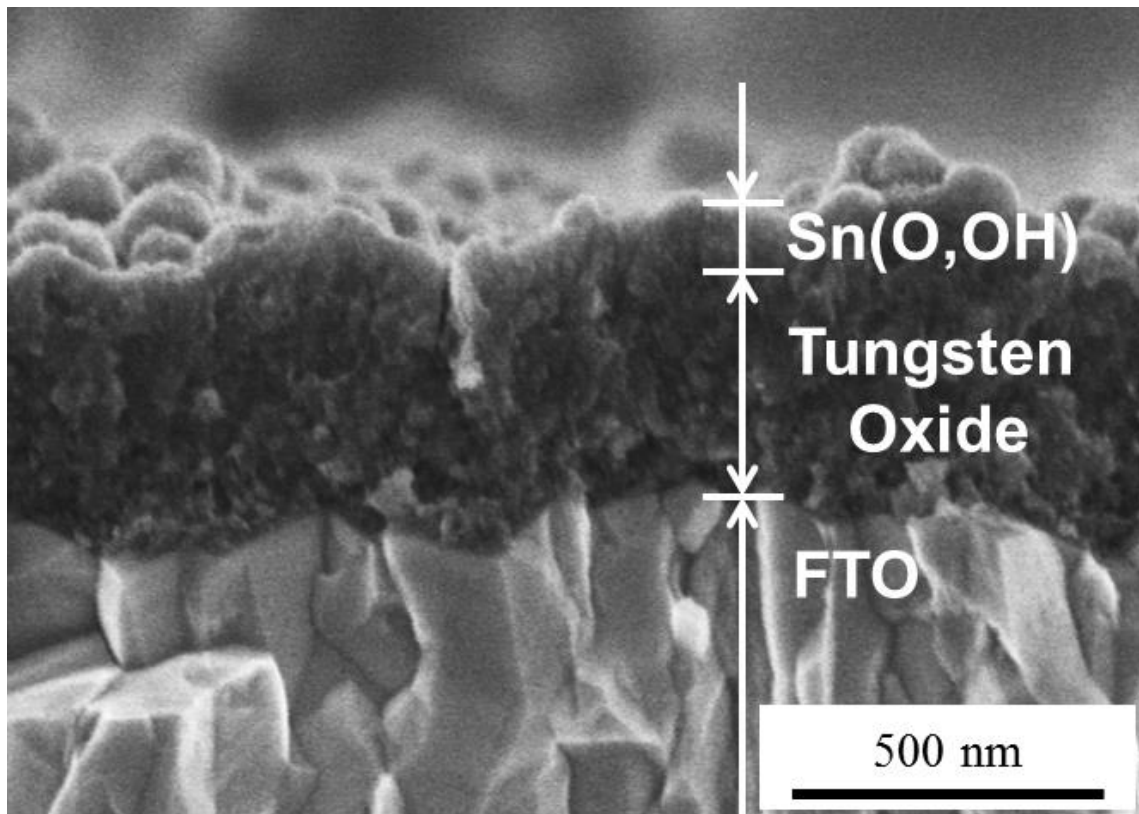


Figure 5.2 Cross-sectional SEM image of  $\text{WO}_3(\text{H}_2\text{O})_{0.33}/\text{Sn}(\text{O},\text{OH})$  bilayer structure.

### 5.3.2 Coloration reaction of a $\text{FTO}/\text{WO}_3(\text{H}_2\text{O})_{0.33}/\text{Sn}(\text{O},\text{OH})$ bilayer structure

Optical transmission spectra and the change in appearances of the  $\text{WO}_3(\text{H}_2\text{O})_{0.33}/\text{Sn}(\text{O},\text{OH})$  bilayer structure before and after applying the voltage are shown in Figure 5.3, in addition to the schematic illustration of the  $\text{WO}_3(\text{H}_2\text{O})_{0.33}/\text{Sn}(\text{O},\text{OH})$  bilayer structure(a). The optical transmission decreased rapidly at wavelength around 400 nm by the absorption edge of  $\text{WO}_3(\text{H}_2\text{O})_{0.33}$  layer, irrespective of applying the voltage.

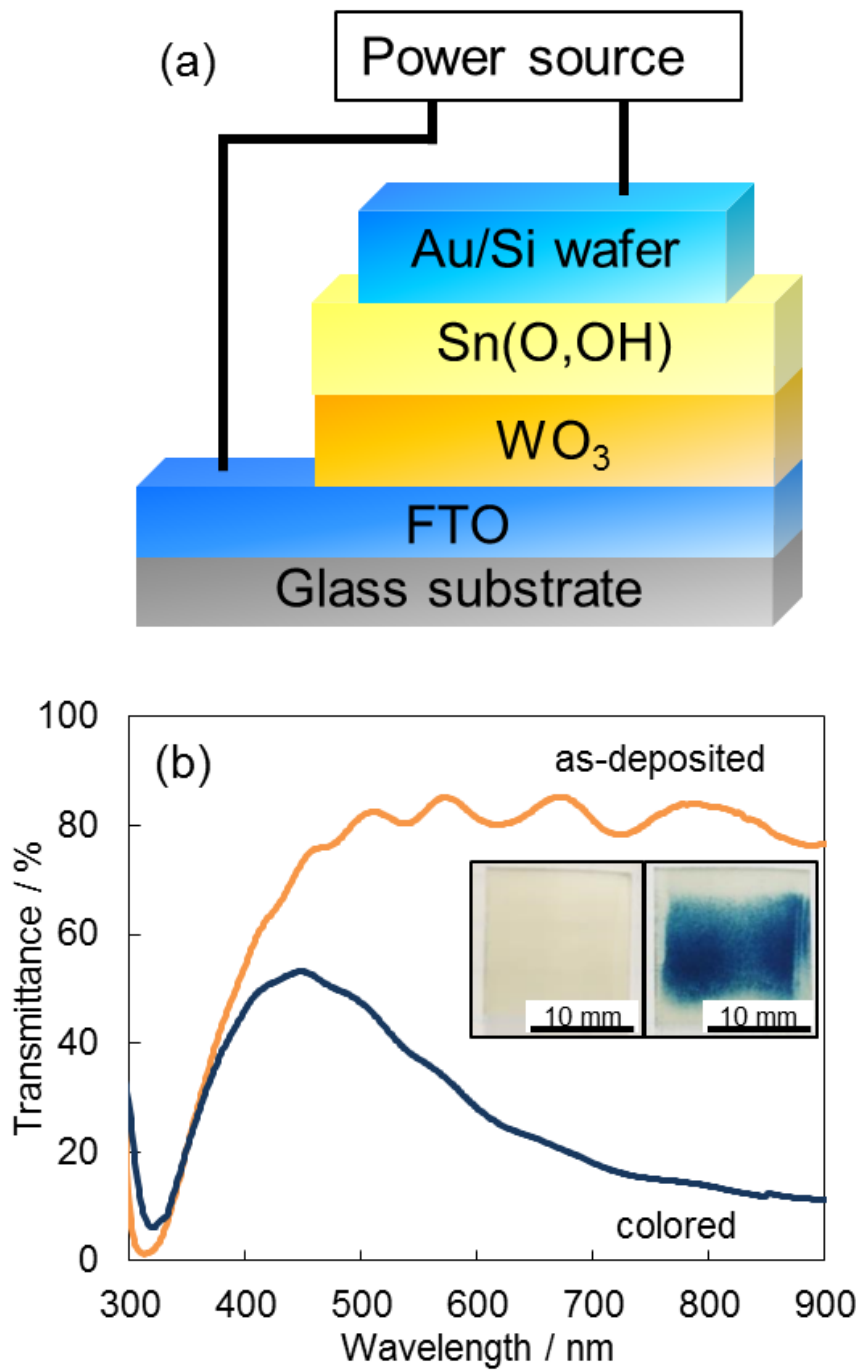


Figure 5.3 Schematic illustration of the structure of the  $WO_3(H_2O)_{0.33}/Sn(O,OH)$  bilayer structure(a), and optical transmission and the change in appearance the  $WO_3(H_2O)_{0.33}/Sn(O,OH)$  bilayer structure before and after applying voltage.

The  $\text{WO}_3(\text{H}_2\text{O})_{0.33}/\text{Sn}(\text{O},\text{OH})$  bilayer structure showed transmission of 80% in visible region of wavelength ranging from 500 to 900 nm before applying voltage, and optical transmission decreased at the wavelength longer than 450 nm by applying voltage, and it was demonstrated that the  $\text{WO}_3(\text{H}_2\text{O})_{0.33}/\text{Sn}(\text{O},\text{OH})$  bilayer structure was operated as an all-solid-state electrochromic device. Transmission of the  $\text{WO}_3(\text{H}_2\text{O})_{0.33}/\text{Sn}(\text{O},\text{OH})$  bilayer structure before and after applying the voltage was 84.94% and 21.44% at 663 nm. Since the current density and colored area were 0.5 A and  $1.5 \text{ cm}^2$ , the coloration efficiency (CE)[16] was estimated to be  $0.03 \text{ cm}^2/\text{C}$ . The CE value was lower than those already reported for solid state ECDs with tantalum and iridium[2]. The performance of ECD was affected by several factors such as electrical characteristics including the ion mobility in bulk and heterointerface[1,16]. Furthermore, investigation on the parameters, especially the bulk characteristics and heterointerface state in the  $\text{WO}_3(\text{H}_2\text{O})_{0.33}/\text{Sn}(\text{O},\text{OH})$  bilayer structure, is needed to enhance the CE value. It was demonstrated that the Sn(O,OH) layer played a role as an ion-injection layer and the  $\text{WO}_3(\text{H}_2\text{O})_{0.33}/\text{Sn}(\text{O},\text{OH})$  bilayer structure showed electrochromic characteristics from clear transparency to blue color.

## 5.4 Conclusions

The solid-state  $\text{WO}_3(\text{H}_2\text{O})_{0.33}/\text{Sn}(\text{O},\text{OH})$  bilayer electrochromic device has been fabricated only by anodic electrochemical deposition on the conductive glass substrate, and the change from clear transparency to blue color has been demonstrated by applying voltage through an Au electrode contacted on the top surface of the device.

The  $\text{WO}_3(\text{H}_2\text{O})_{0.33}/\text{Sn}(\text{O},\text{OH})$  bilayer device overcome the problem of existing device, and it utilized the advantages of electrochemical deposition, such as being low-costly, conventional and easy to applying to large scale products, to best effect. Furthermore, the  $\text{WO}_3(\text{H}_2\text{O})_{0.33}/\text{Sn}(\text{O},\text{OH})$  bilayer device is a potential candidate of an solid-state electrochromic device.

## REFERENCE

- [1] S.K. Deb, Opportunities and challenges in science and technology of  $\text{WO}_3$  for electrochromic and related applications, *Sol. Energy Mater. Sol. Cells*, **92**, 245(2008).
- [2] T. Niwa, O. Takai, Optical and electrochemical properties of all-solid-state transmittance-type electrochromic devices, *Thin Solid Films*, **518**, 1722 (2010).
- [3] T. Niwa, O. Takai, All-solid-state reflectance-type electrochromic devices using iridium tin oxide film as counter electrode, *Thin Solid Films*, **518**, 5340 (2010).
- [4] J.Y. Huang, L. Zhong, C.M. Wang, J.P. Sullivan, W. Xu, L.Q. Zhang, S.X. Mao, N.S. Hudak, X.H. Liu, A. Subramanian, H. Fan, L. Qi, A. Kushima, J. Li, In situ observation of the electrochemical lithiation of a single  $\text{SnO}_2$  nanowire electrode, *Science*, **330**, 1515 (2010).
- [5] K. Aguir, C. Lemire, D.B.B. Lollman, Electrical properties of reactively sputtered  $\text{WO}_3$  thin films as ozone gas sensor, *Sens. Actuators B Chem.*, **84**, 1 (2002).
- [6] W. Wua, Q. Yu, J. Lian, J. Bao, Z. Liu, S.S. Pei, Tetragonal tungsten oxide nanobelts synthesized by chemical vapor deposition, *J. Cryst. Growth*, **312**, 3147 (2010).
- [7] T. Pauporté, Simple  $\text{WO}_3$  electrodeposition, *J. Electrochem. Soc.*, **149**, C539 (2002).
- [8] M. Ruske, G. Bräuer, J. Pistner, U. Pfäfflin, J. Szczyrbowski, Transparent and conductive aluminum doped zinc oxide films prepared by mid-frequency reactive magnetron sputtering, *Thin Solid Films*, **351**, 146 (1999).

- [9] S.T. Chang, I.C. Leu, M.H. Hon, Electrodeposition of nanocrystalline SnO<sub>2</sub> coatings with two-layer microstructure, *J. Cryst. Growth.*, **273**, 195 (2004).
- [10] M. Izaki, T. Omi, Transparent zinc oxide films prepared by electrochemical reaction, *Appl. Phys. Lett.*, **68**, 2439 (1996).
- [11] T. Shinagawa, M. Onoda, B.M. Fariza, J. Sasano, M. Izaki, Annealing effects and photoelectric properties of single-oriented Cu<sub>2</sub>O films electrodeposited on Au(111)/Si(100) substrates, *J. Mater. Chem. A*, **1**, 9182 (2013).
- [12] M. Izaki, M. Nagai, K. Maeda, F.B. Mohamad, K. Motomura, J. Sasano, T. Shinagawa, S. Watase, Electrodeposition of 1.4-eV-Bandgap p-Copper (II) Oxide Film With Excellent Photoactivity, *J. Electrochem. Soc.*, **158**, D578 (2011).
- [13] M. pourbaix, *Atlas of Electrochemical Equilibria in Aqueous Solutions*, (NACE, Houston, TX, 1974).
- [14] J.F. Moulder, W.F. Stickle, P.E. Sobol, K.D. Bomben, J. Chastain, R.C. King Jr., *Handbook of X-ray Photoelectron Spectroscopy: A Reference Book of Standard Spectra for Identification and Interpretation of XPS Data*, (Physical Electronics USA Inc., Minnesota, United States of America, 1992).
- [15] C. Agashe, S.S. Major, Effect of heavy doping in SnO<sub>2</sub>:F films, *J. Mater. Sci.*, **31**, 2965 (1996).
- [16] C.G. Granqvist, Electrochromic tungsten oxide films: Review of progress 1993–1998, *Sol. Energy Mater. Sol. Cells*, **60**, 201 (2000).

## **CHAPTER 6**

### **Summary**

#### **6.1 Research summary**

This thesis has been focused on the importance of design of electrochemical deposition for wide bandgap oxide semiconductor based on thermodynamic calculation. I successfully resolved several representative problems of existing electrochemical deposition with novelly designed electrochemical deposition processes based on potential-pH diagrams in order to suggest the importance of design of electro chemical

deposition methods based on thermodynamic calculation. Moreover, I proved an applicability of designing electrochemical deposition processes for industrial purposes by fabricating a novel electrochromic device which overcame weaknesses of existing devices. The main results of this work are summarized below.

In **Chapter 1**, I showed the issues of electrochemical deposition as forming methods for wide bandgap oxide semiconductors and overviewed the methods for designing electrochemical deposition processes based on thermodynamic calculation in order to resolve these issues. I considered that designing electrochemical deposition processes to obtain objective oxides is important, and the objective of this thesis was decided to be “Development of electrochemical deposition process based on thermodynamic calculation”.

In **Chapter 2**, I proved forming metal oxide compounds prepared by electrochemical deposition based on thermodynamic calculation by preparing Zn-Ce-O films on an electrodeposited Ag layer in aqueous solutions containing zinc nitrate hydrate and cerium nitrate hydrate. Theory of deposition was discussed from the view point of critical pH between to oxides and dissolved species. Since  $Zn^{2+}/Zn(OH)_2$  and  $Ce^{3+}/Ce(OH)_3$  have near critical pH values and then both  $Zn^{2+}$  and  $Ce^{3+}$  can co-exist in the solution in a certain pH range, ZnO and  $CeO_2$  were deposited at the same time from the solution. The Ce content in the films changed from 0 to 43 mol% depending on the Ce concentration in solutions. Zn-Ce-O films were identified as a wurtzite ZnO solid solution containing Ce (Ce:ZnO) at 5% Ce, and a mixture of Ce:ZnO and  $CeO_2$  solid solution containing the Zn(Zn:CeO<sub>2</sub>) at 20~43% Ce.

In **Chapter 3**, I developed the novel anodic electrochemical deposition of tungsten oxide hydrate using oxygen-evolution reaction based on thermodynamic calculation, and it resolved the problems of existing electrochemical deposition, i.e. nonuniformity of oxidation states of metal ions in oxide films. Crystalline tungsten oxide hydrate films of  $\text{WO}_3 \cdot \text{H}_2\text{O}$  and  $\text{WO}_3 \cdot (\text{H}_2\text{O})_{0.33}$  were prepared on conductive glass substrates by anodic electrochemical deposition in aqueous solutions containing 0.01–0.5 mol/L  $\text{WO}_4^{2-}$  without any heat-treatments. The valence state of obtained tungsten oxide hydrate films were +6, and this film is proved to have high chemical uniformity. The large  $\text{WO}_3 \cdot \text{H}_2\text{O}$  with square shapes obtained in the 0.01–0.09 mol/L  $\text{WO}_4^{2-}$  solutions possessed a bandgap energy of approximately 2.5 eV, and granular- $\text{WO}_3 \cdot (\text{H}_2\text{O})_{0.33}$  films obtained in the 0.05–0.5 mol/L  $\text{WO}_4^{2-}$  solutions showed 3.3 eV in bandgap energy. Tungsten oxide hydrate films prepared in 0.01–0.9 mol/L  $\text{WO}_4^{2-}$  solutions possessed excellent crystalline of  $\text{WO}_3 \cdot \text{H}_2\text{O}$  and  $\text{WO}_3 \cdot (\text{H}_2\text{O})_{0.33}$ , and obtaining crystalline tungsten oxide hydrate without any heat treatment is novel and advantageous point of this method. The  $\text{WO}_3 \cdot \text{H}_2\text{O}$ - $\text{WO}_3 \cdot (\text{H}_2\text{O})_{0.33}$  mixed film prepared in the 0.03–0.09 mol/L  $\text{WO}_4^{2-}$  solutions showed a photoresponse for visible light at 380–600 nm, due to the existence of 2.5 eV-bandgap  $\text{WO}_3 \cdot \text{H}_2\text{O}$ . The  $\text{WO}_3 \cdot \text{H}_2\text{O}$  is a realistic candidate as a photomaterial such as a photocatalyst which is operative in visible light.

In **Chapter 4**, I developed the novel anodic electrochemical deposition for  $\text{Sn}(\text{O},\text{OH})$  using combination reaction of acid-base reaction and oxidation-reduction reaction based on thermodynamic calculation. This method resolved the problem of nonuniform oxidation states in existing electrochemical deposition.  $\text{Sn}(\text{O},\text{OH})$ , mixture of  $\text{SnO}_2$  and  $\text{Sn}(\text{OH})_4$ , with unified valence of +4 was prepared by electrochemical deposition

designed by thermodynamic calculations. Obtained Sn(O,OH) completely covered substrate, and had smooth surface and tetragonal fine crystal structure.

In **Chapter 5**, I demonstrated the fabrication of  $\text{WO}_3 \cdot (\text{H}_2\text{O})_{0.33} / \text{Sn}(\text{O,OH})$  bilayer structure for all-solid-state electrochromic devices by anodic electrochemical deposition above-mentioned in **Chapter 3** and **Chapter 4**, and resolved problem of existing electrochromic device fabrication such as costly and complex processes.  $\text{WO}_3 \cdot (\text{H}_2\text{O})_{0.33} / \text{Sn}(\text{O,OH})$  bilayer structure was prepared by anodic electrochemical deposition on the FTO substrate. It was revealed that the  $\text{WO}_3 \cdot (\text{H}_2\text{O})_{0.33} / \text{Sn}(\text{O,OH})$  bilayer structure was fabricated with an approximately 400 nm  $\text{WO}_3 \cdot (\text{H}_2\text{O})_{0.33}$  layer and an approximately 100 nm Sn(O,OH) layer by the XPS measurement and FE-SEM observation. Electrochromism of  $\text{WO}_3 \cdot (\text{H}_2\text{O})_{0.33} / \text{Sn}(\text{O,OH})$  bilayer structure was observed by optical transmission measurements. A voltage of 5 V was applied to the  $\text{WO}_3 \cdot (\text{H}_2\text{O})_{0.33} / \text{Sn}(\text{O,OH})$  bilayer structure for 1 min, and its color changed from colorless transparent to blue.  $\text{WO}_3 \cdot (\text{H}_2\text{O})_{0.33} / \text{Sn}(\text{O,OH})$  bilayer structure successfully worked as a novel and low-costly all-solid-state electrochromic device, and thereby I demonstrated the applicability of these electrochemical depositions based on thermodynamics.

I resolved the problem of existing electrochemical deposition for wide band gap oxide semiconductor by electrochemical deposition based on thermodynamic calculations. The results demonstrated here will strongly contribute to the improvement of the preparation of oxide semiconductor and its devices.

## 6.2 Acknowledgement

The works of chapter 3 to chapter 5 were supported by JSPS KAKENHI Grant Number 25870324.

This thesis is the outcome of my reseach from April 2014 untill March 2017 at Thin Film Laboratory, Department of Mechanical Engineering, Toyohashi University of Technology, Japan under supervision of Prof. Dr. Masanobu Izaki. The research work could not be accomplished without the great help from many people.

First and foremost, I am deeply grateful to my supervisor, Prof. Dr. Masanobu Izaki. I have learned a lot of things which are essential for a scientist, and when, this thesis was completed, I received great help from Prof. Dr. Masanobu Izaki.

Special thanks to the examiners, Prof. Dr. Masahiro Fukumoto and Assoc. Prof. Dr. Masakazu Kobayashi for provided me very valuable ideas, suggestions and comments that improved this thesis.

Next, I want to gratitude my special thanks to Assoc. Prof. Dr. Seiji Yokoyama for his kind comments and ideas especially during the discussion in laboratory's seminars. Furthermore, I would like to offer my special thanks to Assist. Prof. Dr. Junji Sasano, who has supported me throughout my research work with his patience, ideas, discussions, comments, supports and knowledge. Then also many thanks to Mr. Akihiko Kawanishi and Mr. Kouichi Muramoto of Cooperative Research Facility Center, Toyohashi University of Technology for their uncountable assistance and cooperation in some of analytical equipment.

I do appreciate to the great help of Dr. Tomoyuki Fujinami and Dr. Takanobu Asakawa of Electroplating Engineers of Japan Ltd., Kanagawa, Japan. They are coworker of research of the Zn-Ce-O films and they give me important advice about the Zn-Ce-O films.

In my daily work I have been blessed with a friendly and cheerful group of lab members. They are very helpful and always assisted me to complete my works, as well as daily life; especially to the “Sasano group” members, Mr. Adachi, Ms. Shimizu, Mr. Ebitani, Mr. Masaki, Ms. Yasarah, Mr. Matsuo, Mr. Wada, Mr. Sakai, Mr. Yamamoto, Mr. Kojima, Mr. Kobayashi and Mr. Kitano and other lab members. Moreover, I am deeply grateful to Mr. Khoo, who has grateful helped me to draw up this thesis. I would like to offer my special thanks to the lab secretaries, Mrs. Banno, Mrs. Hayashi and Mrs. Ito, for their kind supports and assistance.

I would like to express my gratitude to my parents, brother, sister and late grandparents, I could not have continued my study without the support of my family. I do not really know how to my express my thanks to them.

**Toyohashi, Aichi, Japan**

**March 2017**

**Kentaro Nishiyama**

## 6.3 Research achievements

### 6.3.1 List of publications

[1] Electrodeposition of Zn-Ce-O Films with Controlled Bandgap Energy, **Kentaro Nishiyama**, Junji Sasano, Seiji Yokoyama, Masanobu Izaki, Journal of The Surface Finishing Society of Japan, **66**, 320 (2015).

[2] Electrochemical preparation of WO<sub>3</sub> compound films with controlled bandgap energy, **Kentaro Nishiyama**, Junji Sasano, Seiji Yokoyama, Masanobu Izaki, Thin Solid Films, **625**, 29 (2017).

[3] Solid state tungsten oxide hydrate/tin oxide hydrate electrochromic device prepared by electrochemical reactions, **Kentaro Nishiyama**, Ryo Matsuo, Junji Sasano, Seiji Yokoyama, Masanobu Izak, AIP advances, **7**, 035004 (2017).

### **6.3.2 List of conferences**

[1] Effect of Temperature of Electrolyte Solution on the Anodic Deposition of Tungsten Oxide Thin Films, **Kentaro Nishiyama**, Junji Sasano, Seiji Yokoyama, Masanobu Izaki, European Materials Research Society 2014 Spring Meeting (E-MRS 2014 SPRING), Lille, France May 2014 (Poster).

[2] ELECTROCHEMICAL FORMATION OF TIN OXIDE-HYDROXIDE COMPOSITE FILMS FOR THE APPLICATION TO ELECTROCHROMIC DEVICES, **Kentaro Nishiyama**, Ryo Matsuo, Junji Sasano, Seiji Yokoyama, Masanobu Izak, The 3rd International Conference of Global Network for Innovative Technology (IGNITE 2016), Penang, Malaysia, January 2016 (Poster).

### **6.3.3 Awards received**

[1] Best Poster Award, The 3rd International Conference of Global Network for Innovative Technology (IGNITE 2016), Penang, Malaysia, January 2016 (Poster).